Hierarchical Zeolitic Catalysts for Cracking of Triglyceride-rich Biomass to Hydrocarbons

Synthesis, Characterization and Catalytic Performance

Dissertation

zur

Erlangung des akademischen Grades

doctor rerum naturalium (Dr. rer. nat.)

der Mathematisch Naturwissenschaftlichen Fakultät

der Universität Rostock

vorgelegt von

M.Sc. Xuan Hoan Vu

geboren am 12.11.1980 in Bac giang, Vietnam

Rostock: 28.04.2014

urn:nbn:de:gbv:28-diss2014-0122-4

Name: Xuan Hoan Vu

Defense date: 22nd July 2014 (Tuesday)

Defense place: Hörsaal 001, Institut für Chemie, Universität Rostock

Dissertation title: Hierarchical Zeolitic Catalysts for Cracking of Triglyceride-rich Biomass to Hydrocarbons: Synthesis, Characterization and Catalytic Performance.

Referees:

1. PD Dr. habil. Andreas Martin
   Leibniz Institute for Catalysis
   University of Rostock
   Albert Einstein Str. 29a
   18059, Rostock
   Germany

2. Apl. Prof. Dr. Michael Hunger
   Institute of Chemical Technology
   University of Stuttgart
   Pfaffenwaldring 55
   70550 Stuttgart
   Germany

Declaration

I declare that the work presented in this thesis entitled “Hierarchical Zeolitic Catalysts for Cracking of Triglyceride-rich Biomass to Hydrocarbons: Synthesis, Characterization and Catalytic Performance” is original and was carried out by myself to obtain the doctoral degree at Leibniz Institute for Catalysis e.V., Rostock, Germany, under the guidance of my supervisors PD Dr. habil. Andreas Martin (Head of Department of Heterogeneous Catalytic Processes) and Dr.-Ing. Udo Armbruster (Group leader). I further declare that this thesis has not been submitted, either wholly or in part, to any academic institutions for the award of any other degree or qualifications.

Rostock, 28.04.2014

Xuan Hoan Vu

Acknowledgements

The present thesis benefited from the contributions of many people in innumerable ways. To all of them I am gratefully acknowledged.

First and foremost, I would like to express my sincerest gratitude and appreciation to my supervisor, **PD Dr. habil. Andreas Martin**, who has supported me throughout my doctoral work with his patience, encouragement and valuable advices. His immense knowledge and philosophy of applied research have guided me in all the time of research and writing of this thesis. I am extremely grateful for the outstanding academic and personal education he has given.

I am deeply grateful to my co-supervisor, **Dr.- Ing. Udo Armbruster** for his persistent help and inspiring discussions. His wide knowledge and personal experience have a significant impact on my thesis. I am greatly indebted to him for teaching me how to handle with the experimental set-up and detailed revision despite other obligations like running new projects or industrial commitments.

My special thanks then go to Drs. U. Bentrup, N. Steinfeldt, D.-L. Hoang, M. Schneider, M.-M. Pohl, Mr. R. Eckelt, Mrs. R. Bienert and other analytical staff of LIKAT for their help in characterizing my samples. My grateful thanks are also extended to Dr. R. Kraehnert (TU Berlin) and Prof. Dr. M. Hunger (University of Stuttgart) for the SEM and MAS-NMR measurements, respectively.

I would like to thank Prof. Dr. Matthias Beller (Director of LIKAT) for allowing me to work in a high ranking institute like LIKAT. Special thanks to my colleagues in the Department of Heterogeneous Catalytic Processes: Markus for his help to translate the thesis's abstract into German; Guido for the Journal English Club; Pratap, Thuan, and Sumeet for the time we have worked together, for the discussion we have had on research, culture, social life etc.

At Vietnam Petroleum Institute, I would particularly like to thank the leaders of VPI: Dr. Phan Ngoc Trung and Mr. Nguyen Ngoc Anh for giving me an opportunity to study abroad; Dr. Nguyen Anh Duc, Mr. Phan Minh Quoc Binh and Dr. Dang Thanh Tung for the permission to use the SCT-MAT facility and the warm welcome during my research stay at VPI-PVPro. Mr. Nguyen Sura is acknowledged for his help to carry out the catalytic test experiment.

Finally, I owe my deepest gratitude to my parents for their unwavering love and support; to my brother and his family for everything they have done for me; to my beloved wife **Nguyen Thanh Huong** and our son **Nemo** for being on my side, for all their love, motivation and support, to whom I dedicate this thesis.

Abstract

The limited availability of petroleum resources combined with environmental concerns has driven the search for renewable sources of liquid fuels and chemicals. In this respect, processing of triglyceride-rich biomass derived oils in a fluid catalytic cracking (FCC) unit represents a promising option for the future to produce biofuels and chemicals. This strategy enables the utilization of the existing refining infrastructure and configuration which would require little additional capital investment. Under FCC conditions, however, the yield and quality of the desired products, i.e. gasoline-range hydrocarbons and light olefins are poor when processing unsaturated triglycerides over FCC catalysts (Ultra-stable Y zeolites - USY). It implies that conventional FCC catalysts based on large pore zeolite Y, developed for petroleum processing, are not ideal for transformation of triglyceride-rich biomass.

On the other hand, comparative studies have evidenced that medium pore zeolite ZSM-5 is the best zeolite type catalyst for converting triglycerides to gasoline-range hydrocarbons. Unfortunately, a high gas yield with reduced fraction of light olefins is generally observed, suggesting the occurrence of undesired secondary reactions due to the diffusion constraints imposed by the relatively small pore size of ZSM-5. Moreover, the experimental conditions employed in most of these laboratory-scale works are far from those of an industrial FCC unit where the same catalyst may display remarkably lower catalytic activities because of the shortened contact time. To alleviate the diffusion limitations, facilitating the access to the acid sites located inside the ZSM-5 micropores, in this work, an additional network of mesopores has been introduced by post- and direct-synthesis approaches to create superior hierarchical zeolitic catalysts for the cracking of triglycerides to gasoline-range hydrocarbons and light olefins under FCC conditions.

At the start of the thesis, the post-synthesis protocol involving the optimization of alkaline treatment and subsequent strong acid washing has been established for the preparation of mesoporous ZSM-5 (MZ) materials from commercial Al-rich ZSM-5 (Si/Al = 11). It is found that an appropriate NaOH concentration during alkaline treatment is a decisive factor for the development of intracrystalline mesoporosity while a subsequent strong acid washing is required to completely remove Al-rich debris, thereby greatly improving the textural and acidic properties. The gas phase cracking of cumene, carried out as model reaction for evaluating spacious properties of porous solids, reveals that the presence of intracrystalline mesoporosity indeed increases the reactivity of the MZ materials as the surface density of strong Brønsted sites is primarily retained while their accessibility is improved. The catalytic activity of the external surface as probed by the

gas phase cracking of 1,3,5-triisopropylbenzene (TIPB) indicates that the formation of larger pores and the enrichment of Brønsted acid sites on the external surface caused by base-acid treatment are favorable for conversion of bulky molecules like TIPB.

The direct synthesis of hierarchical zeolitic catalysts involves a two-step process in which intact ZSM-5 nanocrystals (nano-ZSM-5) are initially formed by extending the precrystallization time of the ZSM-5 precursor solution, followed by dispersing them in mesoporous SBA-15 analogs that are directly assembled from unreacted precursors by pH adjustment prior to high temperature hydrothermal treatment. The resulting nano-ZSM-5/SBA-15 analog (ZS) composite exhibits domains of nano-ZSM-5 imbedded in highly condensed, well-ordered mesoporous SBA-15 analogs containing zeolite building units. The acidic properties, particularly the surface density of strong Brønsted acid sites, of the ZS materials are significantly enhanced, being comparable to those of nano-ZSM-5. The micro-/mesostructures of the ZS are well preserved even upon steaming at 800 °C for 24 h, confirming the remarkable hydrothermal stability. The catalytic activity of the ZS was probed by the gas phase cracking of cumene and TIPB which indicates that the ZS is effective for the conversion of both molecules thanks to the increased density of Brønsted acid sites with high accessibility provided by the bimodal pore system.

The advantages of the hierarchical MZ and ZS catalysts over commercial ZSM-5 (parent ZSM-5) and industrial FCC catalyst (Midas-BSR) are ultimately evaluated in the cracking of unsaturated triglycerides, i.e. triolein and waste cooking oil (WCO) under FCC conditions. As expected, the industrial FCC catalyst displays the poorest catalytic performance, giving the least conversion and yield of light olefins, but the highest coke formation. Compared to parent ZSM-5, enhanced conversion and selectivity toward the desired products are obtained over the MZ material despite its lower acidity. The introduction of mesoporosity increases the utilization of zeolite acid sites by the enlarged external surface, thereby the increased conversion. At the same time, it partially suppresses the undesired secondary reactions by shortening the micropore diffusion path length, thereby the improved selectivity toward the desired products. The advantage of the ZS composite over the other catalysts is the exceptionally high selectivity toward light olefins, regardless of operation variables. The fast diffusion rate provided by the mesopores of SBA-15 analogs and the shorter diffusion path length inside nano-ZSM-5 coupled to medium acidity might be responsible for the ZS composite's superior catalytic performance.

Zusammenfassung

Die begrenzte Verfügbarkeit von Erdöl-Ressourcen in Verbindung mit Umweltbedenken hat die Suche nach erneuerbaren Energiequellen in Bezug auf flüssige Brennstoffe und Chemikalien vorangetrieben. In diesem Zusammenhang stellt die Verarbeitung von triglyceridreichen Ölen aus Biomasse mit Hilfe des Fluid Catalytic Cracking Prozesses (FCC) eine vielversprechende Zukunftsoption für die Produktion von Biokraftstoffen und Chemikalien dar. Diese Strategie würde die Nutzung des bereits existierenden Raffinerienetzes und dessen Infrastruktur ermöglichen und somit weniger zusätzliches Kapital und Investitionen erfordern. Jedoch sind unter FCC-Bedingungen die Ausbeute und die Qualität der gewünschten Produkte, d.h. Kohlenwasserstoffe mit Siedepunkten im Kraftstoffbereich und leichtere Kohlenwasserstoffe, nur gering, wenn ungesättigte Triglyceride an equilibrierten FCC-Katalysatoren (USY-Zeolith) umgesetzt werden. Es zeigt sich, dass konventionelle FCC-Katalysatoren, basierend auf großporigen Zeolithen (Y-Typ), welche für die Erdölverarbeitung entwickelt worden sind, nicht ideal für die Umsetzung von triglyceridreicher Biomasse sind.

Vergleichsstudien belegen, dass Zeolithe mit mittelgroßen Poren (ZSM-5) die besten Katalysatoren für die Umwandlung von Triglyceriden zu Kohlenwasserstoffen im Kraftstoffbereich sind. Im Allgemeinen wird eine hohe Gasausbeute mit reduziertem Anteil an leichten Olefinen beobachtet, was ein Hinweis auf eine unerwünschte Nebenreaktion ist, hervorgerufen durch die Diffusionsbeschränkung in den relativ kleinen Poren des ZSM-5. Allerdings sind die experimentellen Voraussetzungen im Labormaßstab weit von den Bedingungen der industriellen FCC-Anlagen entfernt, wo der gleiche Katalysator wegen der verkürzten Kontaktzeit eine auffallend geringere katalytische Aktivität aufweist. Um die Diffusionsbeschränkungen zu verringern, die die Zugänglichkeit zu den sauren Zentren im Inneren der ZSM-5 Mikroporen beeinflussen, wurde in dieser Arbeit ein zusätzliches Netzwerk von Mesoporen mit Hilfe eines Post- und eines Direktsyntheseverfahrens in mikroporöse Zeolithe eingeführt, um für das katalytische Cracken von Triglyceriden, unabhängig vom Sättigungsgrad unter FCC-Bedingungen, einen höherwertigeren hierarchischen Zeolith-Katalysator zu erhalten.

Zu Beginn der Arbeit wurde die Optimierung der alkalischen Behandlung, gekoppelt mit einer anschließenden Waschung mit starken Säuren, für die Herstellung von mesoporösen ZSM-5 (MZ) aus kommerziellen aluminiumreichen ZSM-5 (Si/Al = 11) etabliert. Es wurde festgestellt, dass die richtige NaOH-Konzentration während der alkalischen Behandlung ein entscheidender Faktor für die Entwicklung intrakristalliner Mesoporosität ist. Das nachfolgende Waschen mit Säure ist notwendig, um

aluminiumreiche Ablagerungen vollkommen zu entfernen, wodurch die Textur und die sauren Eigenschaften verbessert werden.

Als Modellreaktion zur Bestimmung der räumlichen Eigenschaften von porösen Materialien wurde das Cracken von Cumol in der Gasphase untersucht. Mit Hilfe dieser Reaktion wurde gezeigt, dass das Vorhandensein von intrakristallinen Mesoporen die Reaktivität des MZ erhöht, weil die Oberflächendichte an stark sauren Brönsted-Zentren erhalten bleibt, während gleichzeitig ihre Zugänglichkeit verbessert wird. Wie die Untersuchung der katalytischen Aktivität der äußeren Oberfläche beim Gasphasencracken von 1,3,5-Triisopropylbenzol (TIPB) zeigt, ist die Bildung von größeren Poren und die Anreicherung von brönstedsauren Zentren auf der äußeren Oberfläche abhängig von der Säure-Basen-Behandlung. Diese Faktoren begünstigen besonders die Umsetzung von sperrigen Molekülen wie beispielsweise TIPB.

Die direkte Synthese von hierarchischen Zeolith-Katalysatoren folgt einem zweistufigen Prozess. Zuerst werden die intakten ZSM-5-Nanokristalle (nano-ZSM-5) gebildet, indem die Kristallisationszeit in der ZSM-5-Precursorlösung verlängert wird. Anschließend werden die Kristalle in mesoporösen SBA-15-Analoga dispergiert, welche sich direkt aus den verbleibenden unverbrauchten Vorläuferspezies während der pH-Einstellung zusammenlagern. Dann werden die Kristalle einer Hydrothermalsynthese bei hohen Temperaturen unterzogen. Das resultierende Kompositmaterial aus nano-ZSM-5/SBA-15 Analoga (ZS) weist nano-ZSM-5-Domainen in einem kondensierten und stark geordneten mesoporösen SBA-15-Gerüst mit Zeolith-Strukturen auf. Die Azidität, insbesondere die Oberflächendichte von starken Brönsted-Säurezentren des ZS, ist im Vergleich zum nano-ZSM-5 signifikant erhöht. Die micro-/meso-Strukturen des ZS sind auch in Versuchen bei 800 °C über einen Zeitraum von 24 Stunden sehr stabil. Dies deutet auf eine bemerkenswerte hydrothermale Stabilität hin.

Die katalytische Aktivität des ZS wurde in Analogie zu den MZ-Materialien am Beispiel des Gasphasencrackens von Cumol und TIPB untersucht. Dabei wurde gezeigt, dass ZS aufgrund der erhöhten Dichte der brönstedsauren Zentren und der besseren Zugänglichkeit durch das bimodale Porensystem sehr effektiv für die Umsetzung von beiden Molekülen ist. Die Vorteile der hierarchischen MZ- und ZS-Katalysatoren im Gegensatz zu kommerziellen ZSM-5 (Precursor ZSM-5) und industriellen FCC-Katalysatoren (Midas–BSR) sind in der stärker ausgeprägten Fähigkeit zum katalytischen Cracken von ungesättigten Triglyceriden, z.B. Triolein und Waste Cooking Oil (WCO), bei FCC-Bedingungen zu sehen. Wie zu Beginn der Arbeiten vermutet wurde, zeigt der industrielle FCC-Katalysator die schwächste katalytische Leistung, was sich in der geringsten Umsetzung und Ausbeute an kurzkettigen Olefinen, aber der am stärksten

ausgeprägten Bildung von kohlenstoffhaltigen Ablagerungen („coke“) zeigt. Im Vergleich zu den kommerziellen ZSM-5-Precursoren konnte mit MZ trotz geringerer Azidität eine gesteigerte Umsetzung und Selektivität bezüglich der gewünschten Produkte erreicht werden. Die Einführung der Mesoporosität erhöht die Möglichkeiten zur Nutzung der sauren Zentren des Zeoliths durch die vergrößerte äußere Oberfläche und führt somit zu einem höheren Umsatz. Gleichzeitig unterdrückt sie teilweise die Bildung von unerwünschten Nebenreaktionen durch eine verringerte Weglänge bei der Diffusion durch die Microporen und erhöht dadurch die Selektivität bezüglich der erwünschten Produkte. Der Vorteil des ZS-Kompositmaterials gegenüber den anderen Katalysatoren ist die besonders hohe Selektivität in Bezug auf leichte Kohlenwasserstoffe unabhängig von den Versuchsbedingungen. Die schnelle Diffusionsrate der Mesoporen der SBA-15-Analoga und die verringerte Weglänge bei der Diffusion innerhalb der nano-ZSM-5-Strukturen gekoppelt mit der Acidität des Mediums sind die Schlüssel für die hervorragenden katalytischen Eigenschaften des ZS Kompositmaterials.

Table of Contents

1. **Introduction** 1
1.1 The role of biofuels in the future transportation fuel supply 2
1.2 Triglyceride-rich biomass as renewable feedstock 4
1.3 Conversion of triglycerides into biofuels and chemicals 5
1.4 Objective of the thesis 6
1.5 Outline of the thesis 7
2. **Literature Review** 9
2.1 Cracking of triglyceride-rich biomass 10
2.1.1 Thermal cracking of triglycerides 10
2.1.2 Catalytic cracking of triglycerides 11
2.1.2.1 General background 11
2.1.2.2 Chemistry of catalytic cracking of triglycerides 12
2.1.2.3 Cracking catalysts 15
2.2 Hierarchical ZSM-5 based catalysts 16
2.2.1 General background 16
2.2.2 Mesoporous ZSM-5 catalysts by post-synthesis modifications 18
2.2.3 Micro-/mesoporous composite catalysts by using ZSM-5 seeds 20
2.2.4 Catalytic performance of hierarchical ZSM-5 based catalysts 21
2.3 Summary and conclusions 22
3. **Experimental Methods and Equipment** 23
3.1 Catalyst preparation 24
3.1.1 Preparation of mesoporous ZSM-5 materials by post-synthesis modifications 24
3.1.2 Preparation of nano-ZSM-5/SBA-15 analog composites from preformed ZSM-5 precursors 25
3.1.3 Industrial FCC catalyst as reference 26
3.2 Catalyst characterization 26
3.2.1 X-ray powder diffraction (XRD) 26
3.2.2 Small/wide angle X-ray scattering (SAXS/WAXS) 27
3.2.3 Fourier transform infrared spectroscopy (FT-IR) 28
3.2.4 Scanning electron microscopy (SEM) 28
3.2.5 Transmission electron microscopy (TEM) 29
3.2.6 Solid state magic angle spinning nuclear magnetic resonance spectroscopy (MAS-NMR) 29
3.2.7 Nitrogen physisorption 29
3.2.8 Temperature-programmed desorption of ammonia (NH_3-TPD) 31
3.2.9 Fourier transform infrared spectroscopy of adsorbed pyridine (py-IR) 31
3.2.10 Atomic absorption spectroscopy (AAS) and inductively coupled plasma-

optical emission spectroscopy (ICP-OES) 32
3.3 Hydrothermal stability tests 32
3.4 Experimental setups for catalyst evaluation 32
3.4.1 Catalytic cracking of cumene and TIPB 32
3.4.2 Catalytic cracking of triolein and WCO 33
3.4.2.1 Experimental setup 33
3.4.2.2 Feedstock and product analysis 34
4. **Post-synthesis Design of Mesoporous ZSM-5 Materials from Commercial Al-rich ZSM-5** 37
4.1 Physico-chemical properties of parent ZSM-5 (ZSM-5-P), alkaline treated (MZ-xAT) and alkaline-acid treated (MZ-xAAT) materials 38
4.2 Acidity study 42
4.3 Catalytic cracking of cumene and TIPB 45
4.4 Summary and conclusions 49
5. **Direct Synthesis of Nano-ZSM-5/SBA-15 Analog Composites from ZSM-5 Precursors** 51
5.1 Evolution of precursors to zeolite crystals 52
5.2 Effect of the pH value during hydrothermal treatment (htt-pH) 53
5.2.1 Effect of the htt-pH on the structural and textural properties 53
5.2.2 Effect of the htt-pH on the acidic properties 56
5.3 Effect of the precrystallization time 57
5.3.1 Effect of the precrystallization time on the morphology, structural and textural properties 58
5.3.2 Effect of the precrystallization time on the acidic properties 64
5.4 Hydrothermal stability 68
5.5 Catalytic cracking of cumene and TIPB 70
5.6 Summary and conclusions 73
6. **Catalytic Performance of Hierarchical Catalysts in the Cracking of Triglyceride-rich Biomass** 75
6.1 Feedstock and catalysts 76
6.1.1 Feedstock 76
6.1.2 Catalysts 76
6.2 Thermal cracking 77
6.3 Catalytic cracking of triolein 78
6.3.1 Catalytic performance of mesoporous ZSM-5 materials 78
6.3.2 Catalytic performance of nano-ZSM-5/SBA-15 analogs 82
6.4 Catalytic cracking of WCO 84
6.4.1 Catalytic performance of various catalysts under mild cracking conditions 84
6.4.2 Catalytic performance of various catalysts under severe cracking conditions 87
6.5 Effect of feedstock composition 90

6.6 Proposed reaction pathway 91
6.7 Summary and conclusions 92
7. **Summary and Outlook** 95
7.1 Mesoporous ZSM-5 materials by post-synthesis modifications 96
7.2 Nano-ZSM-5/SBA-15 analog composites by high temperature synthesis 97
7.3 Performance of hierarchical ZSM-5 based catalysts in the cracking of triglyceride-rich biomass under FCC conditions 98
7.4 Outlook 99
8. **References** 101

Chapter 1

Introduction

The introduction chapter begins with a general background on the role of biomass-derived biofuels in the current and future energy supply. Then, the potential of triglyceride-rich biomass as raw material for producing renewable biofuels and chemicals is presented. Technologies for conversion of triglycerides are briefly discussed and the problems associated with catalytic cracking of unsaturated triglycerides over FCC catalysts are highlighted. Finally the objective and outline of the thesis are given.

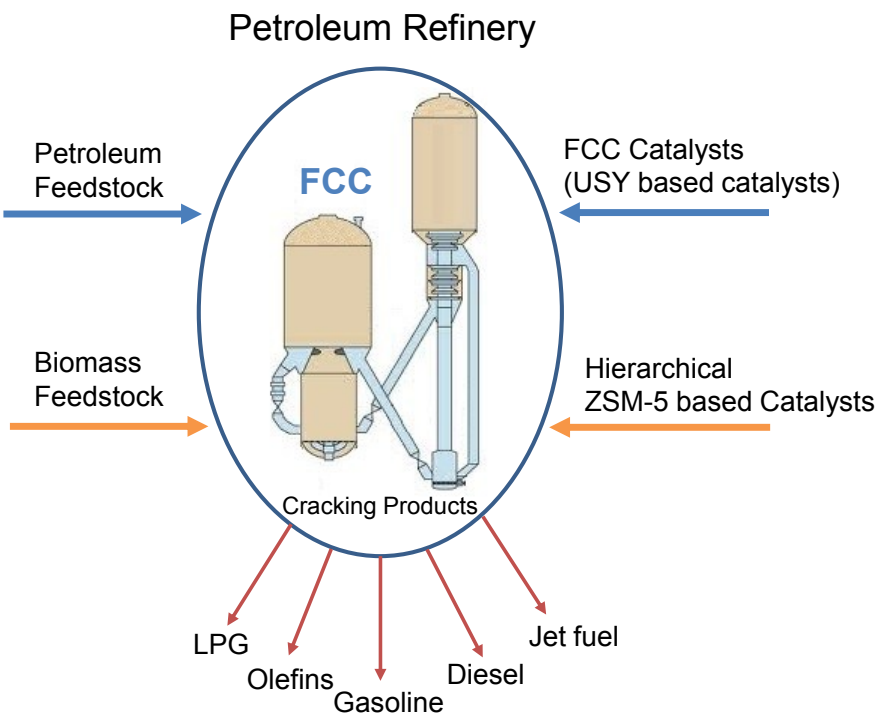

1.1 The role of biofuels in the future transportation fuel supply

One of the most significant challenges facing humanity in the 21st century is to fulfill the increasing energy demand while keeping the emission of greenhouse gases (GHGs) under control. Nowadays fossil fuels represent the main source of energy, but their uses also represent the main source of GHGs (mainly CO_2) emissions [1]. These environmental concerns along with the depletion of petroleum reserves and consequently the rising price of petroleum-based fuels have driven the search for renewable feedstock, as alternative to fossil fuels, to ensure the sustainable future energy supply and to reduce CO_2 emissions. Although many alternative options including nuclear, hydro, wind and solar energy are available for generating heat and electricity, biomass is the only sustainable source for producing liquid transportation fuels in the near future (Figure 1.1) [1,2]. The use of biomass has several advantages compared to fossil fuels such as high availability, renewability and CO_2 neutral ecobalance [1-3]. Indeed, many countries have implemented mandatory legislation in order to increase the utilization of renewable energy, particularly from biomass. For example, the U.S. Department of Energy sets an ambitious target to derive 20% of transportation fuels from biomass by 2030 while the European Directive 2009/28/EC states that at least 10% of traffic fuels will be biofuels by 2020 [4].

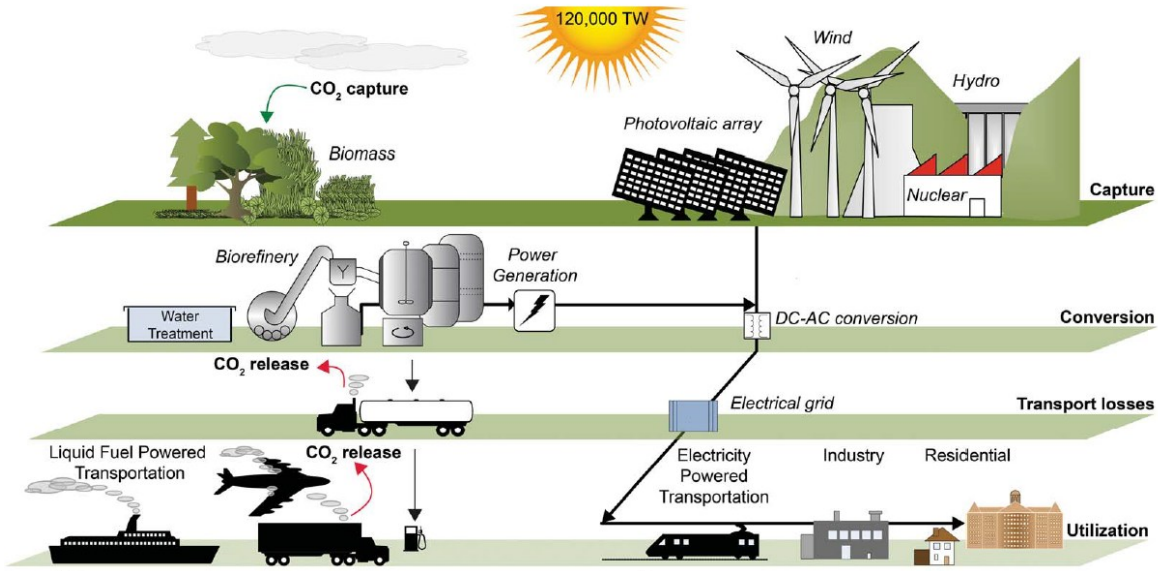

Figure 1.1 Renewable energy alternatives for transportation fuels [1].

According to the world energy outlook to 2035 by IEA [5], fossil fuels including coal, gas and oil will remain the major energy sources, but the contribution of energy from

renewables will rise drastically (Figure 1.2). The consumption of biomass derived biofuels will increase from 1.3 million barrels of oil equivalent per day (mboe/d) in 2011 to 2.1 mboe/d in 2020 and 4.1 mboe/d in 2035. By 2035, biofuels will address 8% of the global transportation fuel demand, up from approximately 3% of 2011. The market share of biofuels in the United States and the European Union will be higher, reaching 15% of the total fuel demand for transport by the projected year. Conventional biofuels including ethanol and biodiesel based on crops containing starch, sugar or vegetable oil will then still play a key role, but an increased contribution of advanced biofuels from cellulosic biomass and from various waste streams, i.e. waste cooking oil (WCO) and algae is expected in the coming years.

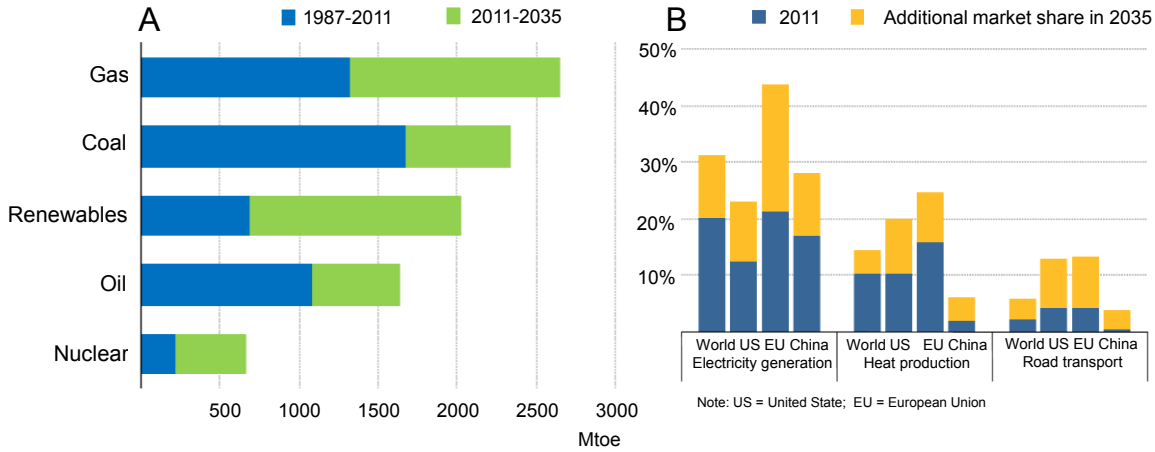

Figure 1.2 The growth (A) and renewable energy share (B) in total primary energy demand [5].

Biomass can be classified into three categories: cellulosic biomass, starch- and sugar-derived biomass and triglyceride-rich biomass [6]. As feedstock, triglyceride-rich biomass is less abundant and more expensive than cellulosic biomass. However, in Europe triglycerides derived from plant oil are the most widely used biomass for biodiesel production via transesterification due to their high energy density, low oxygen content, and efficient conversion [5,6]. Additionally, considering the existing agricultural production capacity, as well as the increasing exploitation of next-generation feedstocks such as non-edible, waste and algae oils, it is expected that a large part of future renewable fuels will remain to be triglyceride derived biofuels. In light of this, triglyceride feedstock, i.e. model compound triolein and real WCO, was selected as representative biomass for the detailed study in this thesis.

1.2 Triglyceride-rich biomass as renewable feedstock

Triglyceride-rich biomass includes animal fats and plant oils, more commonly known as vegetable oils which contain predominantly triglyceride molecules. Oils and fats can be found in the plant and animal kingdom. More than 350 oil bearing plants (seeds) have been recognized of which soybean, palm, cotton, rape and sunflower are the most important in the form of worldwide production [6,7]. The typical fatty acid composition of such oils is listed in Table 1.1 [8]. Most vegetable oils are highly unsaturated with C_{18} fatty acids as the main components, except palm oil which is dominated by saturated palmitic acid.

Table 1.1 Typical fatty acid composition of vegetable oils [8].

Fatty acid composition (wt%)	Rapeseed/ canola	Cottonseed	Palm	Soybean	Sunflower
Unsaturated fatty acids	93	73	49	85	88
oleic acid (C18:1)	61	17	39	23	16
linoleic acid (C18:2)	21	55	10	54	71
α-linolenic acid (C18:3)	11	<1	<1	8	1
Saturated fatty acids	7	27	51	15	12
palmitic acid (C16:0)	4	23	45	11	7
stearic acid (C18:0)	2	2	4	4	5
others	1	2	1	0	0

Cx:y where x is the number of carbon and y is the number of double bonds.

The use of vegetable oils as potential raw materials for producing biofuels mainly depends on their local availability (large and constant production volume). In Europe, rapeseed (canola) oil is widely employed for biodiesel production whereas soybean and palm oils are preferred in the USA and in tropical countries, respectively [6]. However, the utilization of such edible oils as biofuel feedstock has negative impacts on the arable land culture and edible food supply. In this respect, non-edible oils such as jatropha, castor or karanja oils and WCO have been emerging as potential feedstock for biofuel production in recent years.

WCO - waste cooking oil, which is otherwise wasted, is one of the most economical choices for biofuel production. It has been reported that biodiesel produced from WCO reduces the production cost by approximately 60-70% [9,10]. In addition, the utilization of WCO as biofuel feedstock does not compete with food crops and arable land. Large quantities of WCO can be obtained from waste streams of various industries such as the

food industry or animal waste rendering sources if a proper collection system is established. For instance, in EU countries, about 1 million t/a of WCO is generated whereas the estimated amount in the US is approximately 0.4 million t/a [9].

1.3 Conversion of triglycerides into biofuels and chemicals

Vegetable oil can be directly used as fuel in diesel engines, but the high viscosity and low volatility of triglycerides cause a range of engine problems including carbon deposits, oil ring sticking, coking on the injector and thickening of lubricant oils [2]. Therefore, triglycerides need upgrading before being used as a biofuel. The most common way of upgrading vegetable oil involves transesterification of triglycerides into alkyl fatty ester which is currently applied in the commercial production of the so-called first generation biodiesel [11]. However, oxidative stability, comparatively low specific energy content due to oxygen present and cold-flow properties are the major factors that limit the application of biodiesel as a high grade fuel. Furthermore, the production of biodiesel requires highly refined vegetable oil with low free fatty acid content; otherwise the production costs will rise. More than others, the low-value WCO is difficult to process in conventional biodiesel plants. In this context, processing triglycerides solely or co-processing them with conventional petroleum feedstock in standard refinery units is very promising option [4,7,8,12]. This is because petroleum refineries are already built and the use of the existing refining infrastructure and configuration for conversion of triglyceride based biomass requires little additional capital investment. More importantly, the final liquid products are similar to conventional liquid fuels obtained from crude oil in composition, thereby being more compatible with conventional engines and fuel standards. Two options are available in petroleum refineries for converting triglycerides into fuels: hydrotreating and fluid catalytic cracking (FCC) [4,7].

Hydrotreatment of vegetable oils and animal fats by petroleum refinery infrastructure to yield liquid alkanes ranging from C_{12} to C_{18}, which can be used as high quality diesel, has been already considered by some oil companies [4,12-14]. For example, Neste Oil [13] has developed a hydrotreating process (NExBTL technology) that allows the flexible use of triglyceride feedstocks for high grade diesel production in the petroleum refinery. Unfortunately, this process requires large amounts of hydrogen to saturate double bonds and to remove oxygen present in triglyceride molecules, lowering its interest from the economic point of view. Considering that the physico-chemical properties of triglyceride-rich biomass (density, viscosity, and hydrogen-to-carbon ratio etc.) are quite similar to those of vacuum gas oil, one of the most suitable refining units to process triglycerides is perhaps a FCC unit, which is currently used to convert heavy fractions of petroleum crude

oil into lighter and more valuable hydrocarbon products [4,8,15,16]. The FCC process is well-known for its flexibility to adapt to changing feedstock and product demand. The advantages of catalytic cracking over hydrotreating are that the former does not require hydrogen and operates under ambient pressure, thus reducing the production cost. Furthermore, catalytic cracking of triglycerides is the only process that allows producing gasoline and middle distillates as transportation fuels along with light olefins as platform chemicals. Consequently, this option has received an ever-increasing interest from academia as well as industry.

There is a rich body of literature on catalytic cracking of triglyceride-rich biomass, in which various aspects of the cracking of triglycerides have been extensively studied as described in recent reviews [4,6,8,17]. It was shown that under typical FCC conditions, triglycerides are totally converted over equilibrated FCC catalysts into a mixture of hydrocarbons along with CO_2, CO and water [18]. However, the yield and quality of gasoline-range hydrocarbons and light olefins become poor when processing highly unsaturated triglyceride feedstock such as rapeseed oil or oleic acid [19,20]. It implies that conventional FCC catalysts, developed from large pore zeolite Y (pore mouth diameter of 0.74 nm) for petroleum processing, are not sufficient for transformation of triglyceride-rich biomass. On the other hand, comparative studies have evidenced that medium pore zeolite ZSM-5 (pore mouth diameter of 0.52-0.56 nm) is the best zeolite type catalyst for converting triglycerides to gasoline hydrocarbons [6,17]. This is because the medium micropore width of ZSM-5 directs the cracking process toward the formation of C_5-C_{10} hydrocarbons corrsponding to the gasoline boiling range while avoiding the formation of polyaromatic species. However, a high gas yield with low concentration of light olefins is generally obtained, suggesting the occurrence of undesired secondary reactions due to the diffusion constraints imposed by the relatively small pore size of ZSM-5. Moreover, the experimental conditions employed in most of these laboratory-scale works are far from those of an industrial FCC unit and the same catalyst may display remarkably lower catalytic performances because of the shortened contact time.

1.4 Objective of the thesis

To alleviate the diffusion limitations, increasing the access to the acid sites located inside the ZSM-5 micropores, in this thesis, it was planned to introduce an additional network of mesopores to create superior hierarchical ZSM-5 based catalysts for the cracking of triglyceride-rich biomass, independent of unsaturation degree, under FCC conditions. To reach this goal, post- and direct-synthysis approaches will be explored for the preparation of hierarchical ZSM-5 based catalysts from commercial Al-rich ZSM-5 and preformed

ZSM-5 nanoseeds, respectively. Attention has to be paid on the optimization of synthesis parameters to form hierarchical catalysts with improved accessibility and physical transport features while retaining the intrinsic catalytic properties of a typical ZSM-5 zeolite (strong Brønsted acidity and shape selectivity). The obtained solids then have to be submitted to thorough characterizations by various physico-chemical techniques and probe reactions before being tested in the catalytic cracking of unsaturated triglycerides, i.e. triolein and WCO, under FCC conditions.

1.5 Outline of the thesis

The thesis is composed of seven chapters, starting with this introduction and ending with a summary and outlook. The five chapters in between are divided into literature review, catalyst preparation and characterization methods, results and discussion.

Chapter 1 begins with a **general background** on the role of biomass-derived biofuels in the current and future energy supply. Then the potential of triglyceride-rich biomass as raw materials for yielding renewable biofuels and chemicals is presented. Technologies for conversion of triglycerides are briefly discussed in which the problems associated with catalytic cracking of unsaturated triglycerides over FCC catalysts are highlighted. Finally the objective of the thesis is given.

Chapter 2 presents a **comprehensive review of the literature** concerning the current state of catalytic cracking of triglyceride-rich biomass. The focus is put on the reaction pathways, catalysts and the final product distribution. Then a thorough literature survey concerning hierarchically structured zeolitic catalysts with some basic concepts is given. Post- and direct-synthesis approaches for the preparation of hierarchical ZSM-5 based catalysts by ZSM-5 modifications and their benefits in catalyzed reactions are discussed at length.

Chapter 3 describes the detailed procedures for the preparation of hierarchical ZSM-5 catalysts by the **post-synthesis modification of commercial Al-rich ZSM-5** and by the **direct assembly of ZSM-5 nanoseeds**. The basic principle and applications of different characterization methods are illustrated. The experimental set-ups and related procedures for the evaluation of catalytic performance are explained.

Chapter 4 addresses the **post-synthesis treatment of commercial Al-rich ZSM-5 for the preparation of mesoporous ZSM-5 materials**. The optimization of alkaline treatment and subsequent strong acid washing are elaborated based on the results of studies with various characterization techniques. The benefits of generated intracrystalline mesoporosity are evidenced in the gas phase cracking of cumene and 1,3,5-triisopropyl-benzene (TIPB) as probe reactions for the accessibility of newly created mesopores.

Chapter 5 explores **high-temperature synthesis of nano-sized ZSM-5/SBA-15 analog composites from ZSM-5 nanoseeds**. This chapter starts with the optimization of pH values during hydrothermal treatment at elevated temperature for the preparation of a highly condensed, ordered mesoporous SBA-15 analog from ZSM-5 precursors by hydrothermal treatment at elevated temperature. Then the precrystallization time of initially formed ZSM-5 nanoseeds controlling the distribution of ZSM-5 phase and SBA-15 analogs phase is thoroughly discussed. The improved steaming stability and catalytic activity in the gas phase cracking of cumene and TIPB as probe reactions are ultimately presented.

Chapter 6 presents the **catalytic performance of the prepared hierarchical ZSM-5 catalysts** compared to commercial (parent) ZSM-5 and industrial FCC catalyst in the catalytic cracking of triglyceride-rich biomass, i.e. triolein and WCO under FCC conditions. The influence of operation variables, catalyst characteristics and feedstock compositions is systematically studied to establish the structure, property and catalytic performance relationships. The advantages of the hierarchical ZSM-5 catalysts over conventional ZSM-5 or FCC catalysts are evidenced. A reaction network is proposed from the obtained catalytic data.

Chapter 7 gives a concise **summary and conclusion** on the main findings and contributions of this thesis. An outlook with some recommendations for future work is also given.

Chapter 2

Literature Review

In this chapter, a comprehensive review of the literature concerning the current state of catalytic cracking of triglyceride-rich biomass is presented. The focus is put on the reaction pathways, catalysts and final product distribution. Then a thorough literature survey concerning hierarchically structured zeolitic catalysts with some basic concepts is given. Direct- and post-synthesis approaches for the preparation of hierarchical ZSM-5 based catalysts and their benefits in catalyzed reactions are discussed at length.

2.1 Cracking of triglyceride-rich biomass

Cracking of triglycerides can be carried out in the absence of a catalyst (thermal cracking) or in the presence of a catalyst (catalytic cracking). Thermal cracking of triglycerides often produces a large amount of high-molecular weight oxygenated compounds in the organic liquid fraction, reducing their potential as transportation fuels. Contrarily, catalytic cracking is faster and more selective than thermal cracking. The presence of a catalyst allows working at milder operation conditions, driving the process toward the desired products, i.e. gasoline and light olefins, while minimizing the selectivity toward by-products, i.e. dry gas, coke or heavy fractions. Accordingly, in most of available studies involving conversion of triglycerides into hydrocarbons, a catalyst is used, and the development of high performance catalysts for this process requires more efforts.

2.1.1 Thermal cracking of triglycerides

Thermal cracking or pyrolysis of triglycerides involves the chemical decomposition caused by heat in the absence of air or oxygen to form smaller molecules. A general reaction pathway of thermal cracking of a triglyceride is proposed in Figure 2.1 [21]. Fatty acid is initially formed, and then undergoes a series of radical bond cleavage reactions such as radicalic scission, cyclization (Diels-Alder reaction), H-elimination, decarboxylation and decarbonylation. The final pyrolysis products typically consist of gaseous products (C_1-C_5 hydrocarbons, dimethyl ether and hydrogen), organic liquid products (C_{6+} aliphatic hydrocarbons, aromatics and high-molecular weight oxygenated compounds like fatty acids, esters etc.) [21,22].

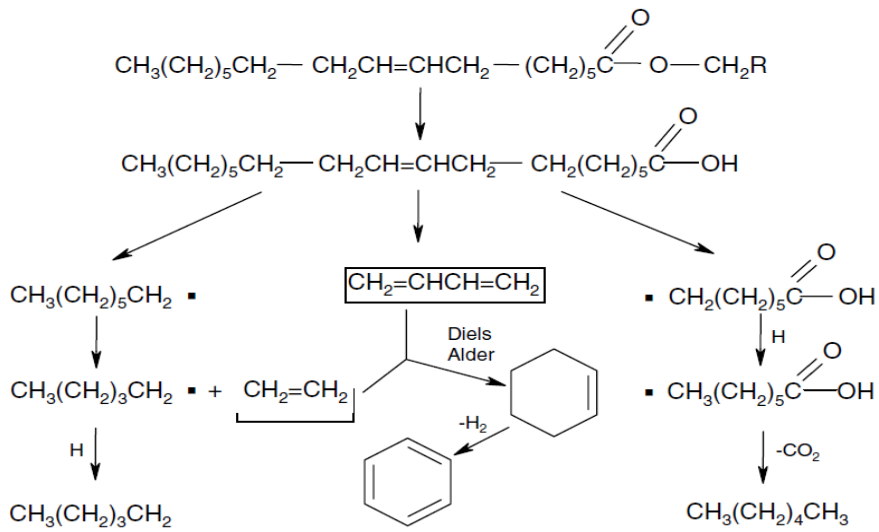

Figure 2.1 The reaction mechanism proposed for pyrolysis of triglycerides [21].

The conversion, product yields and distribution are determined by the nature of feedstock and operation conditions. Generally, the conversion and yield toward light hydrocarbons increase with the severity of reaction conditions. For example, Idem et al. [22] showed that the thermal conversion of canola oil and gas yield increased from approximately 70 and 20 wt% at 400 °C and a GHSV (gas hourly space velocity) of 15.4 h^{-1} to 100 and 75 wt% at 500 °C and a GHSV of 3.2 h^{-1}, respectively.

Pyrolysis of vegetable oils dates back 100 years and pyrolysis products were actually used as fuels during the 1st and 2nd World Wars due to fuel shortage [7,23]. Many types of triglyceride feedstock such as canola/rapeseed, palm, soybean oil or waste cooking oil were submitted to thermal degradation at 300-500 °C or higher and moderate pressure [17,21-24]. The fuel properties of pyrolysis products are normally better than those of original vegetable oils, but still inferior to those of conventional fuels in terms of viscosity and cetane numbers, which imply that further upgrading of pyrolysis products is required.

2.1.2 Catalytic cracking of triglycerides

2.1.2.1 General background

Catalytic cracking of triglyceride feedstock involves pyrolysis in the presence of a catalyst which can direct the process toward the desired products. There is a rich body of literature in which many aspects of catalytic cracking of triglycerides have been investigated [4,6,8,17]. Of various triglyceride-rich biomasses, rapeseed/canola, palm and soybean oils are highly utilized due to their mass production worldwide. Also, waste cooking oil has gained an increasing interest for this process. Most of available studies were conducted in fixed bed reactors using zeolite based catalysts at ambient pressure, a temperature range of 300-500 °C with liquid hourly space velocities (LHSV) varying from 1 to 4 h^{-1} [6,17]. However, several authors have recently performed studies on the processing of triglycerides under operation conditions as applied in commercial FCC units [18-20]. The obtained products typically include gaseous products (C_1-C_4 hydrocarbons, CO and CO_2), organic liquid products, water and coke. The organic liquid product consists predominantly of hydrocarbons corresponding to gasoline and middle distillate (kerosene and diesel) boiling ranges. There are no significant amounts of oxygenated compounds present in the organic liquid product since the initial oxygen in the feedstock is primarily converted to water, CO and CO_2.

In general, the conversion, product yields and distribution rely on the nature of triglyceride feedstock, catalyst characteristics and operation variables. Under typical FCC conditions, Dupain et al. [19] found that the cracking of saturated stearic acid over

equilibrated FCC catalysts resulted in noticeably higher yields of gasoline and light olefins compared to the cracking of unsaturated feedstock such as rapeseed oil or oleic acid. It appears that the production of the desired products can be greatly improved by a better understanding of the chemistry behind and by developing high performance catalysts and reactors [6,7].

2.1.2.2 Chemistry of catalytic cracking of triglycerides

Although catalytic cracking of triglycerides has been studied much, the detailed mechanism of this process has not been well established yet. Nevertheless, most authors have agreed that the primary step involves the initial thermal decomposition of triglycerides to yield heavy oxygenated hydrocarbons by means of free radical mechanism, which is independent of catalyst characteristics. Then, these high-molecular weight oxygenated compounds undergo secondary cracking reactions to give different products wherein the acidity of catalysts plays an important role [4,6,17]. An early global reaction mechanism proposed for the catalytic cracking of canola oil over H-ZSM-5 to hydrocarbons is shown in Figure 2.2 [17,25].

(1) Canola Oil $\longrightarrow$ Heavy Oxygenated C_xH_y ***(thermal)***

(2) Heavy Oxygenated $C_xH_y \longrightarrow$ Heavy $C_xH_y + H_20 + CO_2 + CO$ ***(thermal and catalytic)***

(3) Heavy $C_xH_y \longrightarrow$ Paraffins + Olefins (short and long chain) ***(thermal and catalytic)***

(4) Light Olefins $\rightleftharpoons$ C_2-C_{10} Olefins ***(catalytic)***

(5) C_2-C_{10} Olefins $\rightleftharpoons$ Aromatic C_xH_y + Aliphatic C_xH_y ***(catalytic)***

(6) Canola Oil $\longrightarrow$ Coke ***(thermal)***

(7) n(Aromatic C_xH_y) $\longrightarrow$ Coke ***(catalytic)***

Figure 2.2 Proposed mechanism for the catalytic cracking of canola oil over H-ZSM-5 [17,25].

Once the triglyceride has been thermally decomposed to high-molecular weight oxygenated hydrocarbons (Eq. 1), their transformation into various products starts by deoxygenation such as decarboxylation or decarbonylation (Eq. 2) and then secondary cracking reactions (Eq. 3) to produce short and long chain olefins and paraffins. The subsequent conversions of short-chain olefins (typically C_2-C_4 olefins) into C_2-C_{10} olefins, aliphatic and aromatic hydrocarbons are promoted by catalytic mechanisms such as

oligomerization, cyclization, and aromatization in the pores of ZSM-5 (Eqs. 4 and 5). The formation of coke might result from the thermal polycondensation of triglycerides (Eq. 6) and/or the catalytic polymerization of aromatic hydrocarbons (Eq. 7).

More insights into the reaction pathways of catalytic cracking of triglycerides have been recently given by Dupain et al. [19] who carried out the catalytic cracking of rapeseed oil with commercial equilibrated FCC catalyst (Ecat) under realistic FCC conditions. They reported that triglyceride molecules are mainly converted within 50 ms between 485-585 °C into fatty acids through radical cracking reactions. The formation of radicals is enhanced by the catalyst's external surface. An energetically favorable mechanism for the thermal decomposition of triglycerides into fatty acids is proposed in Figure 2.3.

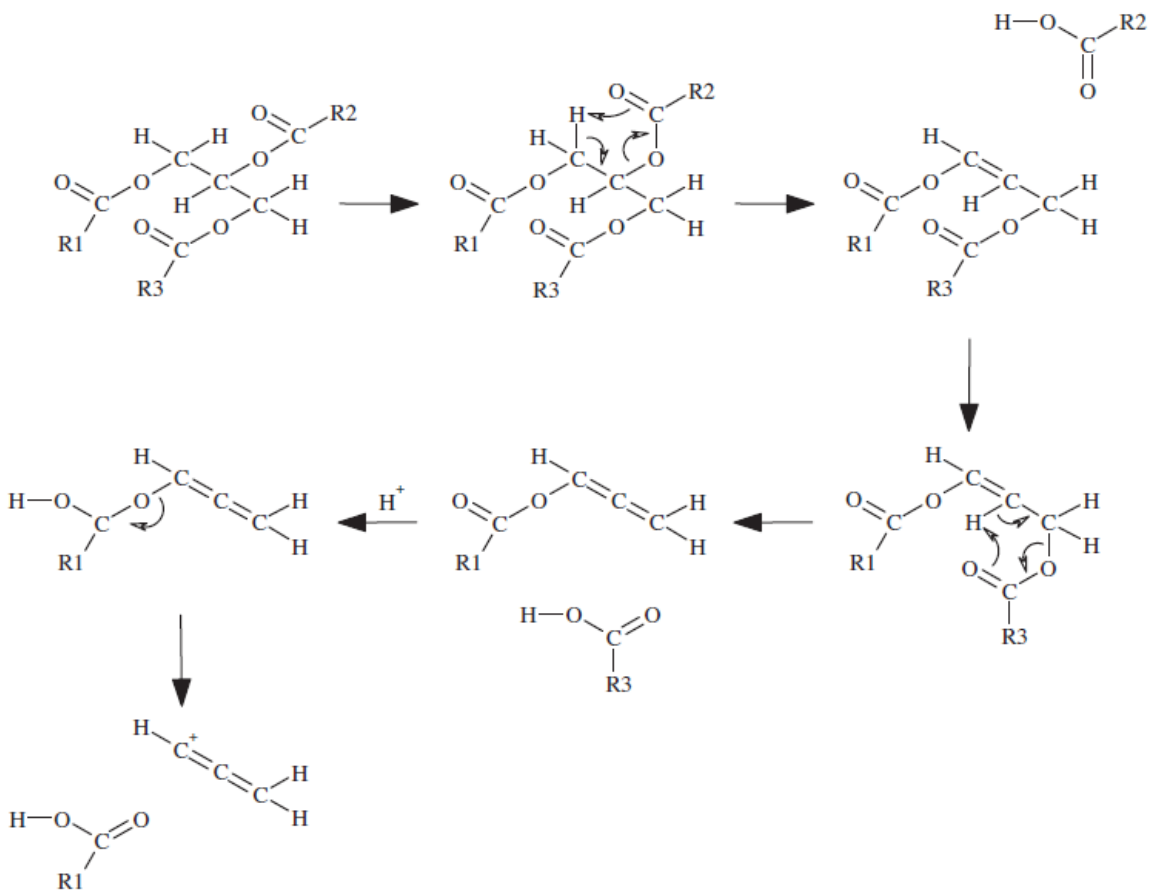

Figure 2.3 Dissociation products of rapeseed oil under FCC conditions [15,19].

A six-membered transition-state is formed in which the central hydrogen atom of the glycerol backbone approaches the ester's carbonyl group. The resulting molecule subsequently decomposes into a fatty acid and a glycerol di-fatty acid ester containing a single double bond in the glycerol backbone. The second fatty acid cleavage produces a glycerol mono-fatty acid ester with two double bonds in the glycerol backbone (allyl-

group). This mono-ester molecule can diffuse into the pores of zeolite based catalysts and spilts off by protonation of the unsaturated carbonyl group. As a result, a fatty acid and an “allyl-carbenium ion” are formed. The highly charged allyl-carbenium ion is thought to be a precursor for coke formation.

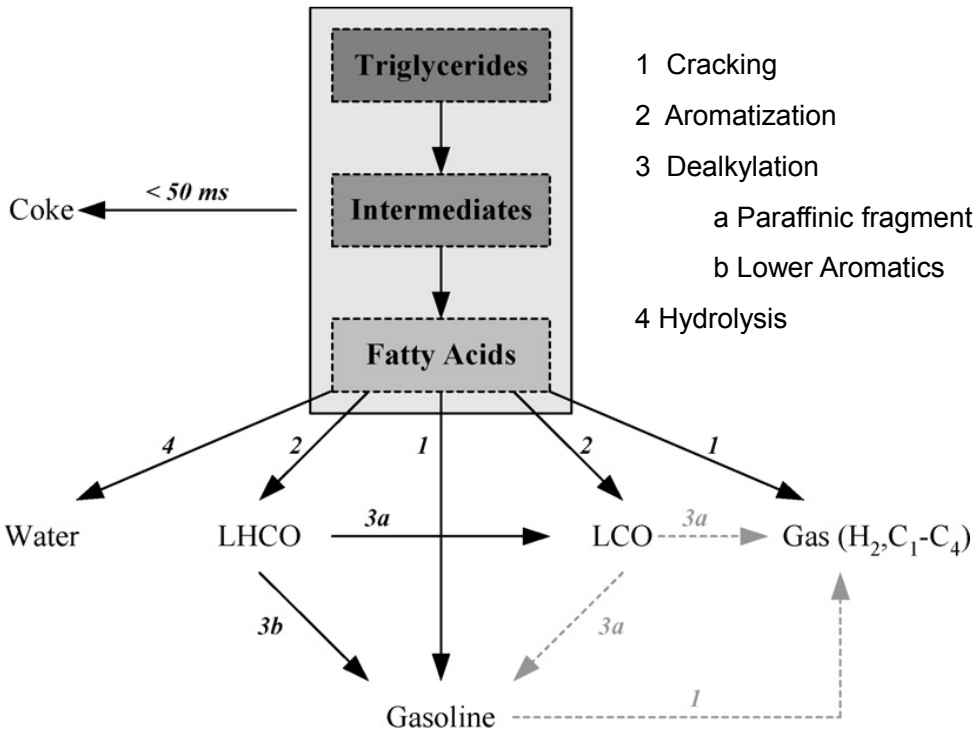

Figure 2.4 Schematic overview of the cracking of rapeseed oil under FCC conditions [19].

The formed fatty acids then enter the pores of zeolite based catalysts and are catalytically converted into various products including light heavy cycle oil (LHCO, 325-360 °C), light cycle oil (LCO, 215-325 °C), gasoline (< 215 °C) and gas as illustrated in Figure 2.4. It was reported that these fatty acids with unsaturated alkyl chains have a strong tendency to undergo a very fast aromatization process (via sequential cyclization, dehydrogenation and condensation reactions) to form (poly)aromatic bodies with alkyl branches [15,19]. This process severely competes with catalytic cracking reactions, leading to high amounts of aromatics predominantly lying in the LCO and LHCO boiling ranges. The subsequent cracking and dealkylation of these heavy aromatic species produce paraffinic fragments and lower aromatic species. The remaining lower aromatic hydrocarbons primarily end up in gasoline (mono-aromatics) or LCO (di-aromatics) boiling ranges, which have no potential to be cracked or dealkylated. This explains why the yields of gasoline and light olefins are relatively low in the cracking of unsaturated triglycerides with Ecat under FCC conditions.

2.1.2.3 Cracking catalysts

Cracking catalysts are materials whose properties are governed by acidity, pore size and shape. In catalytic cracking of triglycerides, zeolite based catalysts are preferred due to their outstanding properties such as strong acidity, high hydrothermal stability and shape selectivity. Other materials such as active alumina, alumina-silica or ordered mesoporous MCM-41 or SBA-15 type materials have been tested in this reaction though they usually give a lower gas yield and higher coke formation due to their lower acidity. Under FCC conditions, conventional FCC catalysts and ZSM-5 additives are mainly employed. A fresh FCC catalyst typically comprises an active component (USY), a matrix (alumina or alumina-silica), and a binder (kaolin). Table 2.1 lists the most relevant works dealing with catalytic cracking of triglycerides which indicate the catalysts, feedstocks and reaction conditions. Among investigated catalysts, the medium-pore zeolite ZSM-5 has proved to be the most effective zeolite type catalyst for converting of triglycerides to gasoline-range hydrocarbons.

Table 2.1 Catalysts, feedstocks and reaction conditions used in catalytic cracking of triglycerides.

Catalyst	Feedstock	Reaction conditions	Reference
SiO_2, silicalite, SiO_2-Al_2O_3, (Al-)MCM-41, (Al-)SBA-15	Palm, canola, soybean oils, WCO	Fixed bed reactor 400-550 °C WHSV =1.8-12.1 h^{-1}	[22,26-30]
H-ZSM-5 and related hybrids/composites	Rapeseed/canola, palm, corn, soybean oils, WCO	Fixed bed reactor 330-550 °C WHSV =1-12.1 h^{-1}	[22,25,27,30-37]
Other zeolites (H-Y, H-β, H-Mordenite etc.) and related hybrids/composites	Rapeseed/canola, palm, soybean oils, WCO	Fixed bed reactor 350-550 °C WHSV =1-4 h^{-1}	[33-36,38]
FCC catalysts/ZSM-5 additives	Rapeseed/canola soybean, corn oils, WCO	SCT-MAT, micro-riser, FCC pilot plants 340-585 °C Contact time: 50 ms-30s	[18-20,39-41]

WHSV: weight hourly space velocity; SCT-MAT: short contact time microactivity test.

The first application of ZSM-5 for the cracking of triglycerides (corn and castor oils) to produce gasoline and chemicals was demonstrated by Weisz et al. [42] from Mobil Oil Company in 1979, just few years after the discovery of this zeolite. Interestingly, they

found that the medium pore zeolite ZSM-5 catalyst has the capability to efficiently convert high molecular weight biomass constituents to high quality gasoline and chemicals. Since then, ZSM-5 and derived materials have been extensively investigated in catalytic cracking of triglyceride-rich biomass including canola/rapeseed [22,25,27,34,37], palm [31-33] and soybean [30] oils or waste cooking oil [35]. The aim is to enhance the production of liquid fuels, in particular gasoline and chemicals (light olefins, aromatics), while avoiding the formation of gas and coke. It is found that the selectivity toward gasoline aromatics over H-ZSM-5 is high, particularly when unsaturated triglycerides are involved in the reaction network [36]. However, H-ZSM-5 usually yields high fractions of undesired gaseous products with low concentration of light olefins [22,27]. The reduced acid site density by impregnating with potassium [25,33] hinders the secondary cracking reactions, leading to the increased fractions of liquid products and light olefins, but the decreased amount of gaseous products. Nanocrystalline and hierarchical ZSM-5 materials were also tested in a fixed bed reactor with long contact time (WHSV = 7.6 h^{-1}) which apparently produced more light olefins than conventional ZSM-5 [37]. It is assumed that these modified ZSM-5 catalysts offer shorter diffusion path lengths, improving mass transfer, and thereby preventing the primary light olefins from further transformation. On the other hand, it should be stressed that the experimental conditions used in most of these works are far from those of an industrial FCC unit where the same catalyst may display a significantly lower catalytic performance due to the scale-up and kinetic limitations (short contact time).

2.2 Hierarchical ZSM-5 based catalysts

2.2.1 General background

Zeolites are a unique class of crystalline aluminosilicates which are widely used as catalysts in the oil refining and petrochemical industry. Medium pore zeolite ZSM-5 (Zeolite Socony Mobil-5) belonging to MFI topology, patented by Mobil Oil Company in 1975, is one of the most important zeolites that has been applied in a number of industrial-scale catalyzed reactions such as cracking, isomerization, alkylation, dewaxing or methanol-to-gasoline or methanol-to-olefins (MTG, MTO) etc. [43]. The exceptional performance of ZSM-5 in catalysis primarily results from its strong Brønsted acidity, hydrothermal stability and uniform micropores of molecular dimensions. The later feature enables shape selective catalytic transformation [43,44]. A typical example among others is the application of ZSM-5 additive in the industrial FCC process. Admixture of a second catalyst containing ZSM-5 to a FCC unit significantly increases the yield of light olefins

(propene and butenes) with a gain in gasoline octane number by selective cracking of linear gasoline range olefins [44,45]. However, ZSM-5 as well as other zeolites to be considered for such applications has a major drawback. As one side effect of their micropores, zeolite catalysts often suffer from diffusion limitations for reactant molecules. The restricted access and slow molecular transport to and from active acid sites inside the micropores (known as configurational diffusion) provoke lower catalyst utilization. Obviously this limited mass-transfer negatively impacts on activity, and sometimes on selectivity and lifetime of the zeolite based catalyst [46-49].

In order to alleviate the internal diffusion limitations and to increase the utilization of the active volume in conventional zeolites, in particular ZSM-5, much effort has focused on increasing the access to zeolites' active sites by shortening the diffusion path length which leads to the so-called hierarchical zeolites. In such hierarchical zeolites, a large fraction of mesopores is introduced in combination with genuine microporosity [46,47]. More importantly, the various domains of porosity should be interconnected to fulfill a distinct function: the micropores provide a high active surface area, the access to which is enhanced by the newly introduced mesoporosity [47]. This can be attained by reducing the crystal size, consequently increasing intercrystalline mesoporosity (nanosized zeolites) and by generating intracrystalline mesoporosity by modifying the structure (mesoporous zeolitic materials). In the former case, due to the poor stability of nanosized zeolites, they are often incorporated in a porous matrix wherein nanosized-zeolite crystals are dispersed and stabilized, leading to the formation of zeolite composites (Figure 2.5).

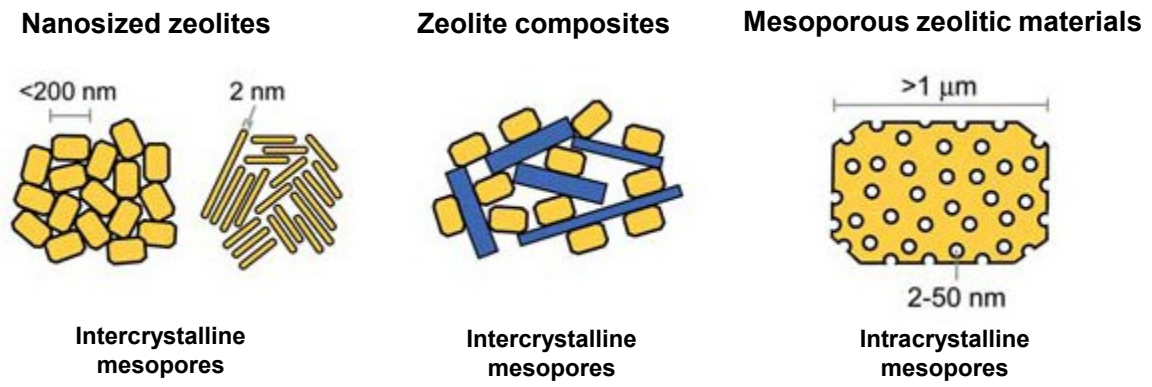

Figure 2.5 Categorization of hierarchical zeolites with improved transport characteristics [47].

Over the past decades, a wealth of synthesis approaches have been proposed and proved to be effective in introducing additional pores with other dimensions in ZSM-5 and related materials. Top-down routes normally involve the post-synthesis treatment of

previously grown zeolites by means of selective leaching of framework atoms, e.g. dealumination by steaming or acid leaching [50] and desilication by base leaching [51], thereby generating the voids inside zeolite crystals. Bottom-up routes can create intercrystalline mesopores by assembling nanosized zeolites or by dispersing them on a porous matrix such as alumina or mesoporous aluminosilicates etc. [52,53], and generate intracrystalline mesopores by using templates such as surfactant, polymer, carbon black and $CaCO_3$ [54,55]. Among them, the post-synthesis treatment of ZSM-5 by base leaching and the use of preformed ZSM-5 nanoseeds for the self-assemblly of mesostructues are perhaps the most investigated routes.

2.2.2 Mesoporous ZSM-5 catalysts by post-synthesis modifications

The introduction of intracrystalline mesoporosity into ZSM-5 crystals by post-synthesis treatment generally consists primarily of the selective extraction of silicon atoms from the zeolite framework. This can be accomplished by treating ZSM-5 with a base (typically NaOH) under controlled conditions [51]. The generated mesopores are highly interconnected and accessible from the external surface of zeolite crystals, providing an effective solution to overcome the diffusion limitation problems [47,51,56]. Over the past two decades, therefore, a huge amount of papers have been reported on the desilication of ZSM-5 and consequent benefits in catalyzed reactions.

The first base treatment of ZSM-5 was carried out by Dessau et al. [57] in 1992 in an attempt to identify Al gradients. The authors found that the selective removal of silicon framework occurred upon treatment in hot alkaline Na_2CO_3 solution, which hinted at the inhibiting role of framework Al during the base treatment. This was later confirmed by the works of Cižmek et al. [58] and Mao et al. [59], but no attention was paid to the evolution of mesoporosity. In 2000, Ogura et al. [60] first evidenced the formation of mesopores in ZSM-5 crystals by NaOH treatment. Later, the systematic studies by Groen et al. [61-64] over ZSM-5 revealed that controlled desilication primarily generates intracrystalline mesoporosity while retaining most of the microporous zeolite characteristics, i.e. intrinsic acidity and shape selectivity. They found the key role of the fraction of framework Al that determined the success of alkaline treatment (Figure 2.6). The narrow window of Si/Al ratios of 25-50 was identified to achieve the optimal introduction of mesoporosity. At higher Si/Al ratios, the excessive dissolution of silicon occurred whereas lower Si/Al ratios hampered the silicon extraction.

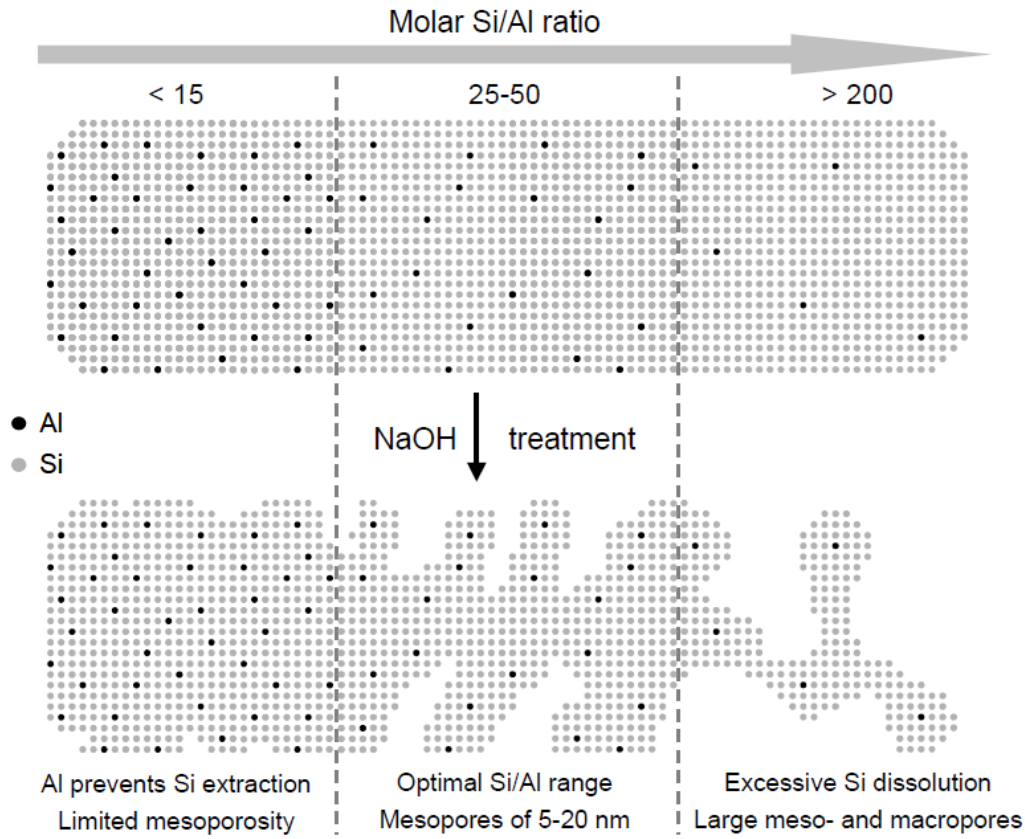

Figure 2.6 Schematic illustration of the influence of the Al content on the mechanism of pore formation during the alkaline treatment of MFI zeolites [64].

Recently, a breakthrough has been made by Verboekend et al. [56,65] who put intense efforts into exploring the full potential of post-synthesis modification routes. The authors reported that it is possible to generate intracrystalline mesoporosity by post-synthesis modifications independent of zeolite framework type or composition. The substantial formation of mesoporosity in ZSM-5 crystals having a Si/Al ratio > 50, e.g. silicalite-1, can be obtained by the addition of pore directing agents (PDAs), e.g. tetra-propyl ammonium cations or $Al(OH)_4^-$ to the base solution used for base leaching. The presence of PDAs on the external surface of zeolites allows controlling the leaching process and tailors the mesoporosity formation [66]. For Al-rich ZSM-5 (Si/Al ratio < 25), strong base treatment and subsequent mild acid washing are recommended. The role of mild acid washing is to remove amorphous aluminum debris, thereby restoring the porosity, crystallinity and acidity [67]. However, up to now, the introduction of mesoporosity in commercial Al-rich ZSM-5 zeolites, especially with a Si/Al ratio as low as 10 and their applications in catalysis are scarcely described in the literature though they are of practical relevance.

2.2.3 Micro-/mesoporous composite catalysts by using ZSM-5 seeds

As a response to the diffusion limitations encountered in zeolite catalysis, in the beginning of 1990s the discovery of ordered mesoporous materials (OMMs) brought about a promising opportunity for moving the zeolite catalysis to the mesoscale by using OMMs [68]. With regular mesopores in the range of 2-30 nm, the diffusion regime in OMMs is typically Knudsen diffusion, which has a diffusivity several orders of magnitude higher than configurational diffusion in micropores [47]. Unfortunately, these mesoporous materials lack the unique strong intrinsic acidity of zeolites and their high hydrothermal stability (caused by the non-crystalline nature of mesoporous walls), which severely limit their practical uses. Accordingly, the introduction of zeolite-like domains into the mesoporous walls by using zeolite seeds as building blocks to construct a mesostructure in a two-step process has been extensively studied [52,53].

The zeolite nanoseeds, also known as precursors or protozeolitic nanoparticles, can be prepared by shortening the hydrothermal treatment time required for the evolution of classical zeolite crystals. This idea was first realized in 2000 by the assembly of faujasitic zeolite (FAU) seeds with cetyltrimethylammonium bromide (CTAB) surfactant in basic media [69]. Soon afterwards, this approach was applied successfully for the synthesis of mesoporous aluminosilicates containing zeolite building units from ZSM-5 nanoseeds using different surfactant templates under either acidic (Pluronic-P123) [70,71] or basic (CTAB) [72,73] conditions. Although the resulting ordered mesoporous materials, referred to as MAS [70] or MSU-S [72], showed greatly enhanced hydrothermal stability and acidity compared to conventional OMMs, these properties were still inferior to those of crystalline zeolites, being not sufficient for industrial applications. The reason is that such materials do not contain the long-range atomic order, characteristic of a crystalline zeolite framework. The preserved zeolite building units in the mesoporous walls envisioned to be in the range of few unit cells because of the small size of preformed zeolite precursors required for the self-assembly of a mesostructure [74,75].

Accordingly, various attempts have focused on the exploration of larger zeolite seeds formed by extending the precrystallization time in the first step for the subsequent assembly of a mesostructure in the second step [75-79]. The obtained micro-/mesoporous composites comprise a zeolite phase intermixed with a mesophase, and the distribution of which can be roughly controlled by the precrystallization time [76]. Compared to mesoporous materials with zeolite building units, the acidic properties of micro-/mesoporous composites prepared from larger seeds are substantially improved because of the zeolite phase present. However, these syntheses were carried out at mild

temperatures (typically 100-150 °C), resulting in the imperfectly condensed mesoporous phase and thereby unsatisfactory hydrothermal stability. Furthermore, the growth of zeolite precursors to micro-sized zeolite crystals and the consequent destruction of mesostructures, in some cases, may not be controllable in a basic medium [78,79]. It has been reported that hydrothermal treatment at elevated temperature (e.g. 200 °C) effectively increases the condensation degree of mesoporous walls in the preparation of conventional OMMs [80,81]. Yet this method has not been employed for the preparation of micro-/mesoporous composites starting from preformed ZSM-5 precursors mainly due to the decomposition of polymer templates in acidic media or to the uncontrollable evolution of zeolite seeds to bulky zeolite crystals in basic media.

2.2.4 Catalytic performance of hierarchical ZSM-5 based catalysts

The superior catalytic performance of mesoporous ZSM-5 materials obtained by post-synthesis modifications compared to conventional (parent) ZSM-5 has been demonstrated in traditional and emerging catalytic applications of industrial relevance such as cracking, alkylation, isomerization, condensation etc. [47,82]. The diffusion rate of cumene in such a mesoporous ZSM-5 catalyst was proved to be three orders of magnitude faster than that in its purely microporous counterpart, which doubled the cumene conversion over the mesoporous ZSM-5 [83]. Liquid phase benzene alkylation over desilicated ZSM-5 showed higher activity and selectivity toward ethylbenzene [56,67,84]. Choi et al. [85] reported 20 times higher activity of alkaline-treated ZSM-5 compared to its parent ZSM-5 in the liquid phase degradation of HDPE (high density polyethylene). The benefits of generated intracrystalline mesoporosity on the activity, selectivity and lifetime of ZSM-5 based catalysts have been evidenced in several emerging reactions such as MTG [86] or fast pyrolysis of lignocellulosic biomass [87]. Nonetheless, such mesoporous ZSM-5 materials have not been explored for the catalytic cracking of triglycerides under FCC conditions yet.

The reported catalytic performance of micro-/mesoporous composite materials is scarce possibly due to the fact that most of relevant works have focused on the synthesis and characterization rather than the applications [52]. However, the advantages of micro-/mesoporous composite materials obtained by using ZSM-5 precursors have been evidenced in several reactions. Catalytic cracking of n-hexane revealed that bimodal porous ZSM-5/TUD-1 composites were more active than both conventional ZSM-5 solely and the mechanical mixture of individual materials [74]. Huang et al. [88] showed 14% and 9% higher n-dodecane conversions over MCM-41/ZSM-5 composites compared to Al-MCM-41 and the mechanical mixture of MCM-41 and ZSM-5 respectively. The high

accessibility of the active sites in the composite materials proved to be responsible for the enhanced conversion and selectivity in acylation of anisole and 1,2-epoxyoctane isomerization with respect to conventional ZSM-5 and Al-MCM-41 [89]. Recently, nano-sized ZSM-5 was tested in the catalytic cracking of triglycerides such as rapeseed oil [37] or waste cooking palm oil [35] using fixed bed reactors, which showed higher selectivity toward light olefins. However, there appears little information available on the conversion of triglyceride feedstocks with micro-/mesoporous composites under FCC conditions aimed at enhancing the formation of gasoline-range hydrocarbons and light olefins.

2.3 Summary and conclusions

Processing triglycerides alone or co-processing them with petroleum feedstock in standard FCC units represents a promising alternative for the production of biofuels and chemicals. However, only few studies have been performed in the conditions that closely reflect the operation conditions of an industrial FCC unit. In these studies, conventional FCC catalysts were routinely employed, which led to the poor yields of gasoline and light olefins when processing unsaturated triglycerides. It is likely that applying conventional FCC catalysts, developed based on large pore zeolite Y for petroleum refining, to triglyceride-rich biomass is not sufficient. More efforts should be devoted to the development of high-performance catalysts by taking the nature of biomass derived oils into account for the efficient transformation of triglycerides under FCC conditions.

On the other hand, medium pore zeolite ZSM-5 turns out to be the best zeolite type catalyst for converting triglycerides to gasoline-range hydrocarbons. Nevertheless, the relatively small pore size of ZSM-5 often imposes diffusion limitations, reducing the catalyst effectiveness and selectivity toward the desired products. In this regard, hierarchical ZSM-5 based catalysts may provide a solution since they couple the intrinsic zeolite characteristics with improved accessibility of active acid sites and mass transfer inside the particles. Post-synthesis treatment of ZSM-5 and direct assembly of ZSM-5 nanoseeds have been recognized as simple and effective approaches for the generation of either intracrystalline or intercrystalline mesoporosity. In the former case, the focus was mainly on ZSM-5 with the optimal Si/Al ratio of 25-50 as starting material. The post-synthesis modification of Al-rich ZSM-5 (Si/Al < 25) and their uses are hardly described in the literature. In the latter case, the exploration of high-temperature synthesis of micro-/mesoporous composites from ZSM-5 nanoseeds deserves more efforts because it provides possibilities to improve hydrothermal stability of known mesoporous materials serving as a matrix.

Chapter 3

Experimental Methods and Equipment

Chapter 3 describes the detailed procedure for the preparation of hierarchical ZSM-5 based catalysts by the post-synthesis modification of commercial Al-rich ZSM-5 and by the direct-assembly of ZSM-5 nanoseeds. The basic principle and applications of different characterization methods are explained. The description of the experimental set-ups and procedures for the evaluation of catalytic performance are given.

3.1 Catalyst preparation

3.1.1 Preparation of mesoporous ZSM-5 materials by post-synthesis modifications

The post-synthesis approach employs commercial Al-rich Na-ZSM-5 (Zeocat PZ-2/25, ZeoChem AG) as a starting (parent) material for the preparation of mesoporous ZSM-5 materials in a two-step process as illustrated in Scheme 3.1. Various samples of the parent Na-ZSM-5 are first treated in the alkaline solution with increasing NaOH concentrations (0.1-0.8 M) to generate mesopores by desilication. Then the resulting alkaline treated samples were exposed to a strong acid solution (0.5 M HCl) for the complete removal of amorphous debris in order to improve the textural and acidic properties.

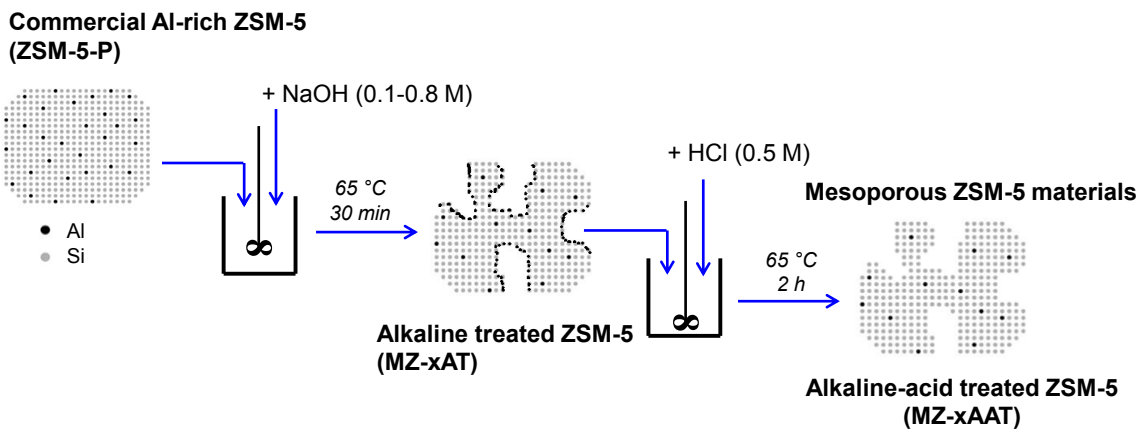

Scheme 3.1 Post-synthesis design of mesoporous ZSM-5 materials from commercial Al-rich ZSM-5 zeolites.

In a typical experiment, 3.0 g of parent Na-ZSM-5, denoted as ZSM-5-P, was submitted to 100 ml of NaOH solutions with different concentrations (0.1-0.8 M) at 65 °C under stirring for 30 min. The zeolite suspension was filtered off, washed thoroughly with distilled water, dried at 120 °C for 12 h and finally calcined at 550 °C for 3 h (hereafter referred to as separation-calcination procedure). The resulting alkaline treated sample is designated as MZ-xAT, where MZ represents the mesoporous ZSM-5 and x refers to the NaOH concentration (M, mol/l) used in the alkaline treatment (AT) step. In a subsequent acid washing step, 1.0 g of the alkaline treated samples MZ-xAT was dispersed in 0.5 M HCl at 65 °C for 2 h, followed by the same separation-calcination procedure as above-described to obtain the calcined products. The resulting sample upon alkaline and subsequent acid treatment is denoted as MZ-xAAT, where AAT means alkaline-acid treatment; MZ and x

represent the mesoporous ZSM-5 and the NaOH concentration in the first step, respectively. Prior to characterization and catalytic study, ZSM-5-P, MZ-xAT and MZ-xAAT materials were transformed into protonated form by ion-exchanging twice in 0.5 M NH_4NO_3 solution at 80 °C for 4 h, then followed by the separation-calcination procedure to obtain the final catalysts.

3.1.2 Preparation of nano-ZSM-5/SBA-15 analog composites from preformed ZSM-5 precursors

The direct synthesis of nano-ZSM-5/SBA-15 analog composites from preformed ZSM-5 precursors involves two major steps. In a first step, seed solutions are synthesized and pre-crystallized in the presence of an appropriate template for microporous zeolite formation for different time periods. A second step of hydrothermal treatment in presence of a supramolecular template converts the fraction of precursors that has not been consumed in the first step into an ordered mesoporous aluminosilicate that surrounds and disperses the initial zeolite nanocrystals. The content of microporous and mesoporous phases can be controlled by controlling the precrystallization time in the first step. The pH adjustment to higher values before high-temperature hydrothermal treatment in the second step is of paramount importance for the formation of a highly condensed ordered mesostructure with increased aluminum incorporation. The complete synthesis procedure is given in Scheme 3.2.

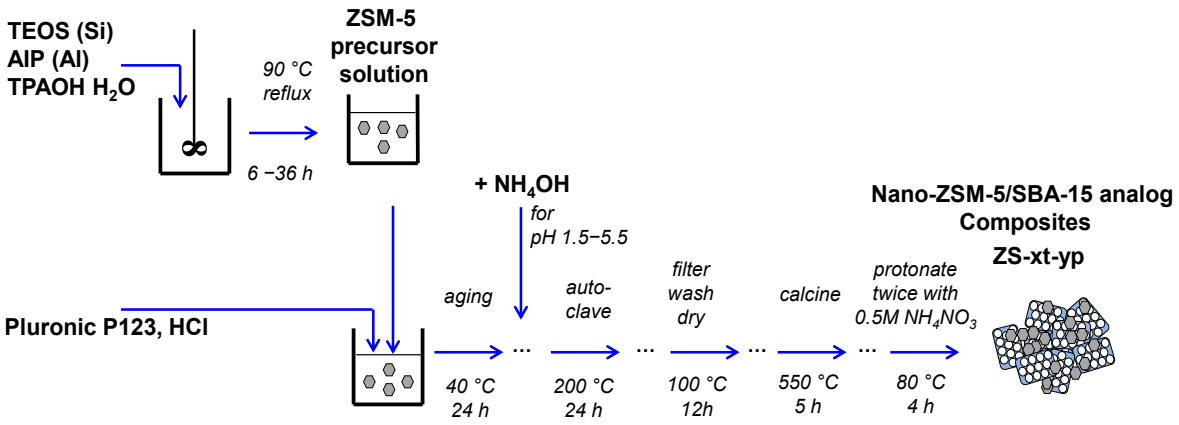

Scheme 3.2 Direct synthesis of nano-ZSM-5/SBA-15 analog composites from preformed ZSM-5 precursors.

A typical synthesis is described as follows: 6.0 g of tetraethyl orthosilicate (TEOS, 99%, Aldrich), 10.0 g of tetrapropylammonium hydroxide (TPAOH, 20% in water, Aldrich), 0.19 g

of aluminum isopropoxide (AIP, 98%, Aldrich) and 2.0 g of distilled H_2O were mixed at room temperature and stirred overnight to complete the hydrolysis, followed by pre-crystallization at 90 °C for various time periods (6 h, 12 h, 24 h and 36 h) in a reflux system to obtain the desired precursor solutions with the final molar composition of 60 SiO_2: Al_2O_3: 20 TPAOH: 1200 H_2O: 240 EtOH. Simultaneously, the surfactant solution for the second step was prepared by dissolving 2.0 g of triblock copolymer pluronic P123 (EO20PO70EO20, M.W. = 5800 g/mole, Aldrich) in 75 ml of 1.6 M HCl at room temperature and stirring for 4 h to form the clear solution. Then, the ZSM-5 precursor solution prepared as described above was added dropwise to the P123 solution, followed by aging at 40 °C for 24 h. Before transferring the mixture into a Teflon-lined autoclave to incorporate more aluminum and to further condensate silica at 200 °C for 24 h, the pH value was adjusted in steps from 1.5 to 5.5 with an aqueous NH_3 solution. The final product was filtered off, washed with distilled water, and dried at 100 °C for 12 h. The as-synthesized material was calcined in air at 550 °C for 5 h with a heating rate of 2 K/min to remove the organic template. The calcined solid was transformed into the protonated form by two consecutive ion exchanges in 0.5 M NH_4NO_3 solution at 80 °C for 4 h. The resulting hierarchical composite is denoted as ZS-xt-yp, where ZS represents the nanosized ZSM-5/SBA-15 analog composite; x is the precrystallization time (t) in the first step; y represents the hydrothermal treatment pH value (p) in the second step.

For comparison, Al-SBA-15, used as a representative for pure ordered mesoporous aluminosilicates, was prepared under the same conditions for synthesis of ZS-xt-3.5p series, but using conventional silica based precursors instead of zeolite seeds. Additionally, commercial Al-rich ZSM-5 (Zeocat PZ-2/25, ZeoChem AG) was used as a representative for pure ZSM-5 zeolites.

3.1.3 Industrial FCC catalyst as reference

To provide a benchmark, an industrial FCC catalyst (Midas-BSR) obtained from Grace Davison Refining Technologies was tested in the catalytic cracking of triglyceride feedstock under FCC conditions. The physicochemical properties of the industrial FCC catalyst are given in Table 6.2, Chapter 6.

3.2 Catalyst characterization

3.2.1 X-ray powder diffraction (XRD)

XRD is a common analytical technique for phase identification of a crystalline material. The fundamental principle of XRD is based on constructive interference of monochromatic

X-rays and a crystalline sample. These X-rays are generated by a cathode ray tube, filtered to yield monochromatic radiation. After being collimated to concentrate, these monochromatic X-rays are directed onto the sample. The interaction of the incident rays with the sample creates constructive interference (a diffracted ray) when Bragg's Law is satisfied:

$$n\lambda = 2d\sin\theta \quad (1)$$

where n (an integer) is the "order" of reflection, λ is the wavelength of electromagnetic radiation, d is the spacing between the planes in the atomic lattice, and θ is the angle between the incident ray and the scattering planes. These diffracted X-rays are then recorded using digital methods. All possible diffraction directions of the lattice caused by the random orientation of the powdered material can be attained by means of scanning the sample through a range of 2θ angles. The phase identification of the sample is achieved by comparison of line positions and intensity distributions of a set of reflections of the sample with a database from ASTM/JCPDS cards.

XRD patterns were recorded on a theta/theta diffractometer (X'Pert Pro from Panalytical, Almelo, Netherlands) with CuK_α radiation (λ = 0.15418 nm; 40 kV, 40 mA) and an X'Celerator RTMS Detector. The alignment was checked by use of a silicon standard.

3.2.2 Small/wide angle X-ray scattering (SAXS/WAXS)

SAXS/WAXS is a combined technique that enables to determine the ordered structure of materials at nanoscale and atomic scale simultaneously. Like XRD, the basic principle of this method is also based on the constructive interference of monochromatic X-rays and a sample. However, for characterization of ordered mesoporous materials by SAXS, a crystalline sample is not required.

SAXS/WAXS measurements were carried out using a Kratky-type instrument (SAXSess, Anton Paar, Austria) operated at 40 kV and 50 mA in slit collimation using a two-dimensional CCD detector and an imaging plate (Kodak X-ray film), respectively. The 2D scattering pattern was converted into a one-dimensional scattering curve as a function of the magnitude of the scattering vector $q = (4\pi/\lambda)\sin(\theta/2)$ with SAXSQuant Software (Anton Paar). A Göbel mirror was used to convert the divergent polychromatic X-ray beam into a collimated line-shaped beam of CuK_α radiation (λ = 0.154 nm). Slit collimation of the primary beam was applied in order to increase the flux and to improve the signal quality. The sample cell consisted of a metal body with two windows for the X-ray beam. The powdered samples were placed between two layers of Scotch® tape. Scattering

profiles of the mesoporous materials were obtained by subtraction of the detector current background and the scattering pattern of the Scotch® tape from the experimental scattering patterns. Correction of instrumental broadening effect (smearing) was carried out with SAXSQuant software using the slit length profile determined in a separate experiment.

3.2.3 Fourier transform infrared spectroscopy (FT-IR)

FT-IR is a useful method for the study of the zeolite framework structure. This technique is based on the assignment of IR bands to certain structural groups in various zeolite framework structures and thereby enabling the identification of very small zeolite crystals which may not have enough long range atomic order to be detected by XRD. In MFI zeolites (typically ZSM-5), the most structure-sensitive band is at around 550 cm^{-1} caused by the double five-membered rings of tetrahedra in their framework. In contrast, the IR spectra of amorphous silica or aluminosilicates exhibit a band at approximately 450 cm^{-1} and do not show any absorption band near 550 cm^{-1}. Therefore, the band approximately 550 cm^{-1} can be used as an indicative of the presence of a MFI zeolite structure.

The FT-IR spectra were recorded on an ALPHA-FTIR spectrometer (Bruker) using the ATR (Attenuated Total Reflection) sampling technique.

3.2.4 Scanning electron microscopy (SEM)

SEM is a technique that is widely used for the study of surface topography in materials science. The basic principle is that a beam of electrons is generated by a suitable source, e.g. a field emission gun, accelerated by a high voltage and passing through a system of apertures and electromagnetic lenses to yield a thin beam of electrons. Then the thin beam scans the surface of a sample by means of scan coils. The electrons interact with atoms in the sample, producing various signals at the sample surface. The signals derived from electron sample interactions on the sample's surface topography are then detected.

SEM imaging was performed using a field emission SEM JEOL 7401F operated at an acceleration voltage of 4 kV and a working distance of 4 mm. For the imaging, powder samples were attached to carbon tape. Software Image J Version 1.39u was employed to determine the pore diameter from the SEM images and to derive FFT (fast Fourier transform) images.

3.2.5 Transmission electron microscopy (TEM)

TEM is probably the most powerful microscope that utilizes highly energetic electrons transmitted through a very thin sample (< 50 nm) to image and analyze the structure of materials. TEM can provide morphologic and crystallographic information from micron sizes down to atomic scale. High resolution transmission electron microscopy (HRTEM) method is applied for lattice fringe imaging of the structure and visualization of defects and interfaces at atomic scale resolutions.

TEM measurements were performed at 200 kV with a JEM-ARM200F (JEOL), which is aberration-corrected by a CESCOR (CEOS) for the scanning transmission microscopic (STEM) applications. The sample was placed on a holey carbon supported Cu-grid (300 mesh) as received and transferred to the microscope.

3.2.6 Solid state magic angle spinning nuclear magnetic resonance spectroscopy (MAS-NMR)

Solid-state NMR spectroscopy allows the direct investigation of the framework atoms, extra-framework species and surface sites of zeolites and related materials. The basic concept is that NMR active nuclei, e.g. ^{27}Al or ^{29}Si, absorb electromagnetic radiation at a frequency characteristic of the isotope upon application of an external magnetic field. In a solid state such as zeolite samples, the presence of anisotropic interactions often causes a line-broadening effect in NMR spectra. To overcome this problem, the solid state MAS-NMR is applied. In MAS-NMR, a sample is rotated rapidly around an axis at the magic angle θ_m = 54.74° with the static field to effectively suppress chemical shift broadening.

The solid-state NMR investigations were performed with the hydrated material using a Bruker BioSpin Avance III 400WB spectrometer at the resonance frequencies of 104.3 and 79.5 MHz for ^{27}Al and ^{29}Si nuclei, respectively. The MAS-NMR spectra were recorded upon single pulse excitation of $\pi/6$ for ^{27}Al and $\pi/2$ for ^{29}Si nuclei, with repetition times of 0.5 s and 30 s, respectively, and high-power proton decoupling (HPDEC) in the case of studying ^{29}Si nuclei. The sample spinning rates were 8 kHz and 4 kHz for the investigation of ^{27}Al and ^{29}Si nuclei, respectively.

3.2.7 Nitrogen physisorption

Nitrogen physisorption at -196 °C is widely used for the determination of the surface area and pore size distribution of various porous materials. As gas molecules are introduced into the system, they adsorb and tend to form a thin layer that covers the entire adsorbent surface. Increasing the number of gas molecules above the amount necessary for

monolayer formation leads to the formation of multilayers, accompanied by capillary condensation.

To evaluate the surface area of porous materials, the Brunauer, Emmett and Teller (BET) theory is generally accepted despite its theoretical limitation, i.e. an oversimplified model of physisorption. Based on the BET method, one can estimate the number of molecules required to form a monolayer of adsorbed gas on a solid. The well-known BET equation for estimation of the specific surface area is usually expressed in the following linear form:

$$\frac{P}{V(P_0 - P)} = \frac{1}{V_m C} + \left[\frac{C-1}{V_m C}\right]\left(\frac{P}{P_0}\right) \quad (2)$$

Where P and P_0 are the equilibrium and saturated vapor pressure of adsorbate at its boiling point, V is the volume at STP (Standard Temperature and Pressure) conditions filled by molecules adsorbed at pressure P, V_m is the volume of adsorbate required for a monolayer coverage and C is the BET constant related to the heat of adsorption of adsorbate in the first and subsequent layers.

According to Equation (2), V_m and C can be easily calculated from the slope and intercept of the linear BET plot of $P/(V(P-P_0))$ versus P/P_0. Accordingly, the specific BET surface can be calculated in the following equation:

$$S = \frac{V_m N_A A_m}{22414W} \quad (3)$$

Where V_m is the monolayer volume in ml at STP conditions, N_A is the Avogadro constant, W is the weight of the sample (g), and A_m is the mean cross sectional area occupied by adsorbate molecule (e.g. 0.162 nm^2 for nitrogen).

Nitrogen physisorption measurements were carried out at -196 °C with an ASAP 2010 apparatus (Micromeritics). Before measurements, the samples were degassed at 180 °C in vacuum for 10 h. The specific BET surface area was calculated using adsorption data at a relative pressure (p/p_0) up to 0.012 while the total pore volume was estimated from the amount adsorbed at a relative pressure of about 0.976. The micropore volume and external surface area were determined by t-plot method. The pore size distributions were obtained from the desorption branch of the isotherm using the corrected form of the Kelvin equation by means of the Barrett-Joyner-Halenda method with a cylindrical pore model.

3.2.8 Temperature-programmed desorption of ammonia (NH_3-TPD)

NH_3-TPD is a simple technique for characterization of acidic properties in terms of total number and strength of acid sites in porous materials at ambient pressure. Typically the method involves saturation of the surface with ammonia, followed by linearly ramping of the temperature of the sample in a flowing inert gas stream. The amount of ammonia desorbed at characteristic temperatures is taken as the acid site concentration, and the peak desorption temperatures are used to evaluate the strength of acid sites.

NH_3-TPD measurements were carried out in a quartz tube reactor in the range of 100-550 °C. The liberated ammonia was continuously detected by a thermal conductivity detector (TCD, Gow-Mac Instruments Co.). The sample was first activated at 550 °C for 0.5 h under helium flow. After the reactor cooled to 100 °C, the sample was swept with helium gas containing 5 vol% of ammonia for 0.5 h for adsorption. Then the feed gas was switched to helium to remove physisorbed ammonia until the TCD baseline was flat. After that, the temperature was increased to 550 °C with a heating rate of 10 K/min, and desorbed ammonia was quantitatively analyzed by the external standard method based on comparison of the desorption peak area with the standard curve.

3.2.9 Fourier transform infrared spectroscopy of adsorbed pyridine (py-IR)

Since NH_3-TPD does not give information on the nature of surface acid sites of solid catalysts, py-IR is nowadays extensively used for discrimination between various types of surface centers, i.e. Brønsted and Lewis acid sites. Adsorption of pyridine is particularly useful because the assignments of vibrational modes associated with pyridinium ions formed at Brønsted sites and with coordination complexes at Lewis sites are well established. Quantitative analysis of site densities can be obtained by normalizing the integral intensity of individual peaks in the spectrum to the BET surface area.

The FT-IR measurements for the acidity investigations were performed on a Tensor 27 spectrometer (Bruker) using self-supporting wafers and pyridine as probe molecule. A homemade, heatable reaction cell with CaF_2 windows connected to a gas-dosing and evacuation system was used. The sample powders were pressed into self-supporting discs with a diameter of 20 mm and a weight of 50 mg. Before pyridine adsorption, the samples were pretreated by heating in flowing He up to 400 °C and holding this temperature for 10 min. Then the samples were cooled in the respective gas stream to room temperature. Pyridine was adsorbed onto the sample by bubbling the He flow through a pyridine-containing saturator until saturation of the acid sites, followed by evacuation of the reaction cell to remove physisorbed pyridine. The pyridine desorption

was monitored during heating the sample under He stream with 5 K/min up to 400 °C. Spectra were recorded at different temperatures with 2 cm^{-1} resolution and 100 scans.

3.2.10 Atomic absorption spectroscopy (AAS) and inductively coupled plasma-optical emission spectroscopy (ICP-OES)

These techniques make use of absorption and emission spectroscopy to assess the concentration of a particular element in a sample. In AAS, electronic transitions between the energy levels of atoms into excited state are generated by the absorption of photons in the visible frequency range. The variation in the light beam's intensity is detected and correlated with the concentration relative to the absorbance of a calibration standard. However, the drawback of AAS is its low sensitivity; therefore, it is often used for analysis of samples containing relatively high elemental concentrations.

To obtain higher sensitivity, ICP-OES is employed. Atoms or ions present in the sample are excited electronically in argon plasma working at temperatures up to 8000 °C and emit electromagnetic radiation at wavelengths characteristic of a particular element. This light is collected by the spectrometer and resolved into a spectrum. After amplification and calibration against standards, quantitative analysis can be achieved.

The Al and Si contents were determined by ICP-OES (715-ES, Varian) and AAS (Analyst 300, Perkin Elmer), respectively. For this purpose, the samples were digested with a mixture of HCl-HNO_3-HF in a microwave-assisted sample preparation system (Multi wave, Anton Paar/Perkin-Elmer) at 200 °C and 60 bar.

3.3 Hydrothermal stability tests

The solid sample was sieved and 0.2 g with a particle size between 300-700 µm was loaded into a quartz tube reactor. The sample was heated to 800 °C in a helium flow with a ramping rate of 20 K/min. As soon as the target temperature was reached, the helium flow containing 30% steam was introduced into the tube reactor. The steam treatment time was 24 h at a flow rate of 30 ml/min. After the steam treatment, the sample was cooled and characterized by XRD, SAXS and nitrogen physisorption to re-evaluate the structural and textural properties.

3.4 Experimental setups for catalyst evaluation

3.4.1 Catalytic cracking of cumene and TIPB

The gas phase cracking of cumene and 1,3,5-triisopropyl benzene (TIPB) was carried out

in a fixed-bed down-flow stainless steel reactor (10 mm internal diameter) equipped with mass flow controllers for reactant metering. Typically, a fixed amount (0.2-0.6 g) of the sieved catalyst (particle size 300-700 µm) diluted with 2.0 g of quartz beads of the same size was placed in the reactor. Prior to the reaction, the sample was activated in N_2 flow at 300 °C for 2 h to remove physically adsorbed water. The liquid reactant (cumene or TIPB) was fed at a rate of 0.6 g/h by a liquid mass flow controller (LiquiFlow, Bronkhorst) coupled to a controlled evaporator mixer (CEM, Bronkhorst). By this way, the reactant was mixed with N_2 (90 ml/min) as a carrier gas and then evaporated before entering the reactor. The catalytic cracking was conducted at 250-300 °C under ambient pressure. Feed and product streams were analyzed with an online gas chromatograph (HP 5890, equipped with a 6-port sampling valve, a fused silica capillary column (HP5, 50 m × 0.32 mm × 0.52 µm) and a flame ionization detector (FID)). The temperature of the column was held at 50 °C for 2 min, then increased to 280 °C at a rate of 15 K/min and held for 4 min.

3.4.2 Catalytic cracking of triolein and WCO

3.4.2.1 Experimental setup

Catalytic cracking of triolein and WCO was performed on a fully automated Single Receiver Short-Contact-Time Microactivity Test (SR-SCT-MAT) unit from Grace Davison GmbH + Co. KG. The use of the SR-SCT-MAT unit allows avoiding most of the shortcomings encountered with the traditional fixed-bed microactivity test equipment, such as large contact time (20-70 s) or low temperatures in the preheating section (which might hamper an appropriate feed vaporization), and therefore simulating more accurately an industrial FCC unit.

The experimental setup is presented in Scheme 3.3 and consists of a feeding module (1), a metallic fixed bed tubular reactor (2) heated by a three-zone furnace (3) and a product collecting system (4). The feeding module is equipped with a heated syringe (80 °C) and a special motor pump for injecting feedstock into the reactor. The tubular bed reactor (13 mm internal diameter) is filled with a fixed bed where the catalyst is diluted with inert glass beads to maintain a constant-volume reaction independent of the catalyst to oil mass ratio used. A specialized single receiver is used to collect the vapor and liquid products of cracking reactions. More details in the experimental set-up of SCT-MAT is given in the Figure B1 (Appendix).

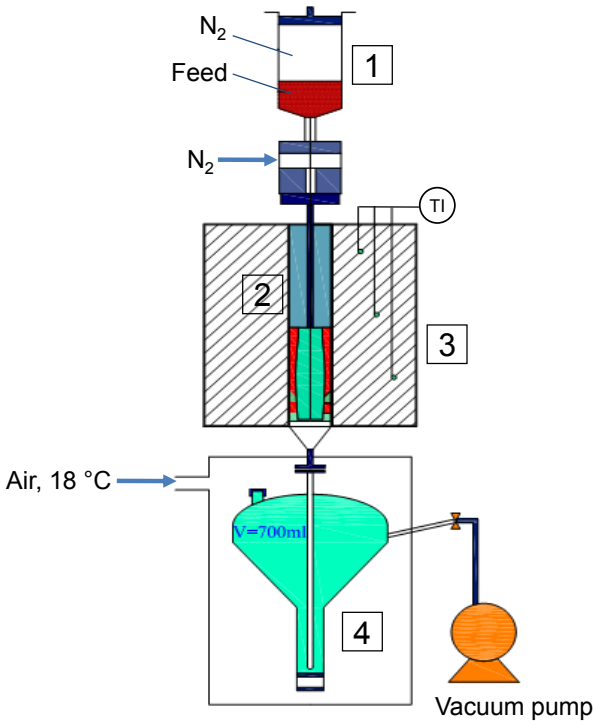

Scheme 3.3 Experimental setup of the SR-SCT-MAT unit

The catalytic cracking experiments of triolein and WCO were carried out at ambient pressure, 400-550 °C, catalyst-to-oil (CTO) mass ratios of 0.2-1.2 (g/g) and a reaction time of 12 s. In a typical run, 1.75 g of feedstock (either triolein or WCO) were fed into the reactor which contained a desired amount of catalyst diluted with glass beads by the way mentioned above. The CTO mass ratio was varied by keeping the weight of feedstock constant (1.75 g) and changing the catalyst weight. The total injection time was 12 s. After the reaction, stripping of catalyst was carried out by using a nitrogen purge. The gaseous and liquid products were collected in the single receiver cooled at +18 °C via cooling system. The mass balance was between 95-100% of the injected feed in all runs.

3.4.2.2 Feedstock and product analysis

The fatty acid composition of the feedstocks (triolein and WCO) was analyzed on GC-MS (QP2010S, Shimadzu). For this purpose, a derivatization was carried out with trimethylsulfonium hydroxide solution (0.25 M in methanol, Fluka) to transform the triglycerides into methyl ester derivatives completely. The C, H, N elemental analysis of triolein and WCO was performed on a TruSpec CHNS Micro analyzer (Leco).

The cracking products comprised main hydrocarbons along with oxygenated compounds (mainly water, CO and CO_2) and coke. Due to the complexity of the cracking

products obtained in a FCC unit, the main hydrocarbons are usually grouped in terms of lumps of boiling ranges. The gaseous hydrocarbon fraction is divided into dry gas (hydrogen, methane, ethane, and ethylene) and liquefied petroleum gas (LPG; propane, propylene, butenes, and butanes). The liquid hydrocarbons are lumped in terms of boiling ranges: C_{5+} gasoline (< 211 °C), light cycle oil (LCO; 221-360 °C) and heavy cycle oil (HCO; >360 °C).

The gaseous products were analyzed according to ASTM D1945-3 method using a Refinery Gas Analyzer (HP Agilent 7890 A, configured with three channels, including one FID and two TCD (thermal conductivity detector)). Light hydrocarbons (C_1-C_5) were analyzed on the FID channel. One TCD with nitrogen carrier was employed to determine hydrogen because of the small difference in the conductivity of hydrogen and helium carrier. The other TCD with helium as carrier gas was used to detect CO, CO_2, N_2 and O_2. More details in the columns and GC conditions for the gas analysis is given in Table B1 (Appendix). For quantitative analysis, the response factor was determined by using a RGA (Refinery Gas Analysis) calibration gas standard (National Oxygen Pte, Singapore).

The liquid organic products were classified according to boiling ranges: C_{5+} gasoline, LCO and HCO as mentioned above by means of simulated distillation (ASTM D2887) on a Simulated Distillation gas chromatograph (Agilent 7890 A, equipped with a capillary column (DB-2887, 10 m x 0.53 mm x 0.3 µm) and a FID). For calibration, a reference gas oil sample (RGO-2887, Agilent) was used. For several liquid samples, PIONA (Paraffin, i-Paraffin, Olefin, Naphthene, and Aromatic) analyses were performed to determine the composition of gasoline using a HP Agilent 7890 A equipped with Hydrocarbon Expert software from Separation System Inc. This method yields the hydrocarbon distribution in the form of n-paraffins, i-paraffins, naphthenes, olefins, and aromatics in the gasoline boiling range (roughly up to C_{15}). Water was measured by a Karl Fischer titration (MKS-520, Kem) and coke was determined by an elemental analyzer (CS600, Leco).

All calculation methods and software were provided by Grace Davison GmbH + Co. KG. The yield toward different products (Y_i, wt%) is defined as gram of product i (W_i) per gram of feed (W_f) (Eq. 4). The standard MAT conversion is defined by the total converted fraction of the feed (Eq. 5). The selectivity toward light olefins with respect to other gaseous hydrocarbons (light olefinicity) is defined as the fraction of light olefins (C_2-C_4) per the total C_2-C_4 hydrocarbons (Eq. 6).

$$Y_i(\text{wt\%}) = \frac{W_i}{W_f} \times 100 \quad (4)$$

$$X\ (\text{wt\%}) = 100\% - (Y_{HCO} + Y_{LCO}) \quad (5)$$

$$\text{Light olefinicity (\%)} = \frac{Y_{C_2-C_4\ \text{olefins}}}{Y_{total\ C_2-C_4}} \times 100 \quad (6)$$

Chapter 4

Post-synthesis Design of Mesoporous ZSM-5 Materials from Commercial Al-rich ZSM-5

Chapter 4 addresses the post-synthesis treatment of commercial Al-rich ZSM-5 for the preparation of mesoporous ZSM-5 materials. The optimization of alkaline treatment and subsequent strong acid washing are elaborated based on the results of studies with various characterization techniques. The benefits of generated intracrystalline mesoporosity are evidenced in the gas phase cracking of cumene and TIPB as probe reactions.

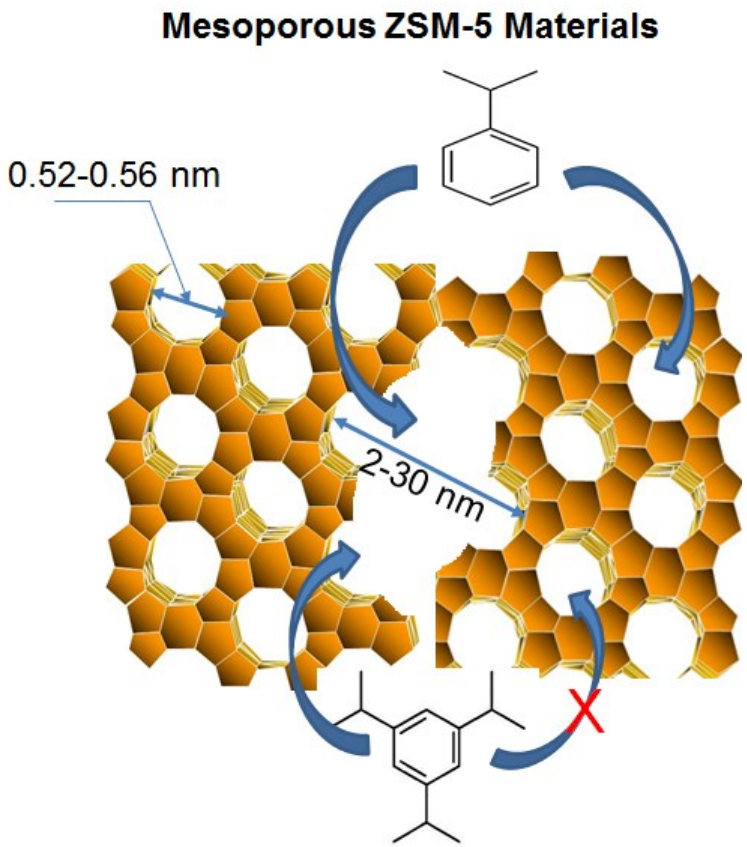

4.1 Physico-chemical properties of parent ZSM-5 (ZSM-5-P), alkaline treated (MZ-xAT) and alkaline-acid treated (MZ-xAAT) materials

The XRD pattern of ZSM-5-P (Figure 4.1) shows the MFI structure as the only crystalline phase. This is further supported by its type I nitrogen isotherm according to IUPAC nomenclature (Figure 4.2) with a high N_2 uptake at low relative pressures (< 0.01). The micropore volume (V_{micro}) and external surface (S_{meso}) were estimated by t-plot method to be about 0.113 cm^3/g and 110 m^2/g, respectively (Table 4.1). The relatively large S_{meso} can be attributed to sub-microscale zeolite crystals of ZSM-5-P, typically characteristic of commercial Al-rich ZSM-5 products, as confirmed by SEM and TEM analyses. The SEM images (Figures 4.3A, B) reveal that ZSM-5-P consists of small crystals (ca. 250 nm) and their aggregates (ca. 800 nm), forming intercrystalline voids. Analogously, the TEM observation provides more insights in the morphology of parent ZSM-5 (Figures 4.4A, B). No intracrystalline mesoporosity is visible from the TEM image at high magnification (Figure 4.4 B).

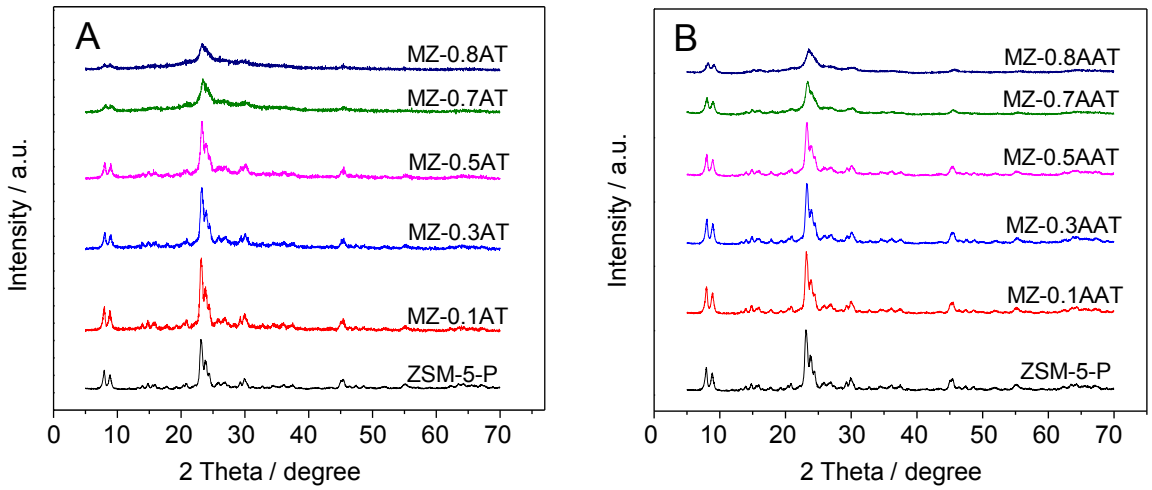

Figure 4.1 XRD patterns of parent (ZSM-5-P) and treated samples: (A) alkaline treated MZ-xAT and (B) alkaline-acid treated MZ-xAAT.

Upon alkaline treatment, the physico-chemical properties of ZSM-5-P have been changed with base concentrations. The XRD patterns (Figure 4.1A) show that the ZSM-5 structure is well maintained at rather low NaOH concentrations (MZ-0.1AT, MZ-0.3AT and MZ-0.5AT). In contrast, MZ-0.7AT and MZ-0.8AT, treated with highly concentrated NaOH solutions (0.7-0.8 M), exhibit much less pronounced characteristic diffraction reflections, indicating the considerable deterioration of their crystalline structure. Similarly, the

recovery yield and the bulk Si/Al ratio also decrease gradually with increasing NaOH concentrations (Table 4.1). It seems reasonable because the preferential silicon extraction from the zeolite framework is facilitated at higher alkaline concentrations [67,90].

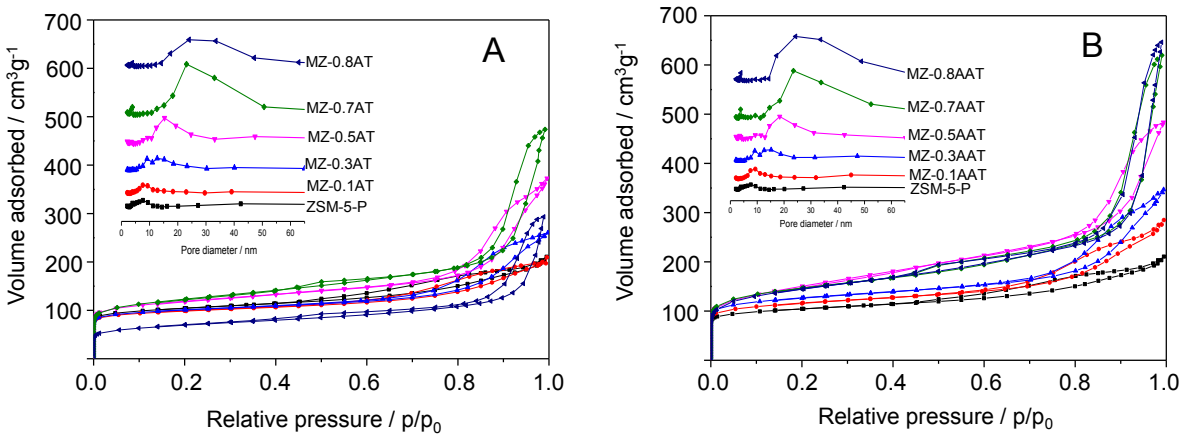

Figure 4.2 N_2 isotherms and the corresponding BJH mesopore size distribution curves (inset) of parent (ZSM-5-P) and treated samples: (A) alkaline treated MZ-xAT and (B) alkaline-acid treated MZ-xAAT.

The changes in the textural properties with employed NaOH concentrations can be evidenced from the data of N_2 adsorption/desorption (Figure 4.2A and Table 4.1). In line with the previous work [67] the treatment of Al-rich ZSM-5 in mild base media (MZ-0.1AT and MZ-0.3AT) has minor effects as shown from their isotherms being similar to that of ZSM-5-P. As treated in higher NaOH concentrations, the resulting materials (MZ-0.5AT, MZ-0.7AT and MZ-0.8AT) display isotherms combining type I and IV behavior, with an enhanced uptake of N_2 at higher relative pressures accompanied by a steeper hysteresis loop, being indicative of the creation of new mesopores. The mesoporosity development can be also seen from the pore size distribution curves derived from the desorption branch of the isotherms (Figure 4.2A, insets). The formation of mesopores becomes substantial as being exposed to 0.5 M NaOH and broadens at higher alkaline concentrations, giving rise to an increased total pore volume (V_t). As a result, the external surface area (S_{meso}) of MZ-0.5AT and MZ-0.7AT increases remarkably at the expense of the microporous volume (V_{micro}). However, the severe base treatment (0.8 M NaOH) of the parent sample lowers the surface areas (S_{meso} and S_{BET}) and pore volumes (V_{micro} and V_t) of MZ-0.8AT due to the extensive dissolution of the zeolite crystals. Thus, the optimal NaOH concentration for substantial mesoporosity formation without losing significant intrinsic microporosity should be 0.5 M under the investigated conditions.

It has been reported that a mild acid washing step is necessary to remove aluminum-rich debris, thereby restoring the desired framework properties [56]. To understand such effect, the MZ-xAT samples in this work were exposed to a fairly concentrated HCl solution (0.5 M) in order to completely remove Al-rich debris. It appears likely that more aluminum-rich residues are formed during the base treatment of Al-rich ZSM-5 with a very low Si/Al ratio of ca. 10. The results are presented in Figures 4.1B, 4.2B and Table 4.1.

Table 4.1 Treatment parameters and physico-chemical properties of ZSM-5-P, MZ-xAT and MZ-xAAT materials.

Sample	NaOH (M)	HCl (M)	Yield[a] (%)	Si/Al[b]	S^c_{meso} (m^2/g)	S_{BET} (m^2/g)	V^c_{micro} (cm^3/g)	V_t (cm^3/g)	Total acidity[d] (mmol NH_3/g)
ZSM-5-P	-	-	100	11	110	373	0.113	0.22	1.24
MZ-0.1AT	0.1	-	90	10	103	363	0.107	0.29	1.31
MZ-0.1AAT	0.1	0.5	81	13	116	412	0.130	0.39	0.98
MZ-0.3AT	0.3	-	79	9	89	367	0.117	0.38	1.39
MZ-0.3AAT	0.3	0.5	67	16	124	445	0.144	0.49	0.85
MZ-0.5AT	0.5	-	74	7	131	411	0.110	0.52	1.26
MZ-0.5AAT	0.5	0.5	62	20	297	456	0.130	0.71	0.71
MZ-0.7AT	0.7	-	56	5	160	342	0.096	0.61	1.13
MZ-0.7AAT	0.7	0.5	45	32	252	462	0.121	0.79	0.50
MZ-0.8AT	0.8	-	48	4	104	224	0.063	0.41	1.22
MZ-0.8AAT	0.8	0.5	33	38	253	436	0.116	0.82	0.42

[a] recovery yield (defined as grams of solid received after treatment per gram of parent sample; [b] analyzed by AAS and ICP; [c] t-plot method; [d] NH_3-TPD.

Generally, the subsequent strong acid treatment increases the bulk Si/Al ratio, the accessible surface area, pore size and volume, but reduces the recovery yield (Table 4.1). These effects become more prominent for MZ-xAT samples treated in stronger base media in the first step, where larger fractions of aluminum-rich debris are generated. In fact, the bulk Si/Al ratio of MZ-0.1AT and MZ-0.3AT varies slightly while that of the other samples shows a dramatic enhancement upon the acid treatment, e.g. the bulk Si/Al ratio = 38 of MZ-0.8AAT vs. 4 of the corresponding MZ-0.8AT sample. Furthermore, the zeolite crystallinity appears not to be affected by the acid treatment as judged from the XRD patterns (Figures 4.1A, B). These results suggest that the deposited aluminum-rich debris has been selectively extracted rather than the framework aluminum even under such a severe acid treatment.

The clearance of aluminum-rich debris induces a significant change in the textural properties of MZ-xAAT. Upon the acid treatment, the nitrogen uptake increases

remarkably, in particular for MZ-0.5AAT, MZ-0.7AAT and MZ-0.8AAT upon acid treatment (Figure 4.2B). This is reflected in the substantial enlargement in their surface areas (S_{meso} and S_{BET}) and pore volumes (V_{micro} and V_t) (Table 4.1). For instance, S_{meso} and V_{micro} increase from 131 m^2/g and 0.11 cm^3/g of MZ-0.5AT to 297 m^2/g and 0.13 cm^3/g of MZ-0.5AAT respectively. Verboekend et al. [67] reported that one can obtain a large S_{meso} of 275 m^2/g by the strong base treatment (1.2 M NaOH) and subsequent mild acid washing (0.1 M HCl) of Al-rich ZSM-5 with a Si/Al ratio of 10. However, the V_{micro} and recovery yield drop severely to 0.05 cm^3/g and 18%, respectively. It is likely that the strong base treatment causes massive dissolution of zeolite crystals, resulting in a much lower recovery yield. On the other hand, the mild acid washing might not completely remove aluminum-rich debris, resulting in a minor improvement in V_{micro}. In this work, by the optimization of alkaline treatment and subsequent strong acid washing, the large external surface (S_{meso} = 297 m^2/g) has been successfully generated while retaining the intrinsic microporous feature (V_{micro} = 0.13 cm^3/g) with a relatively high recovery yield (62%). This further emphasizes that the optimization of treatment variables is of crucial importance in the post-synthesis modification route.

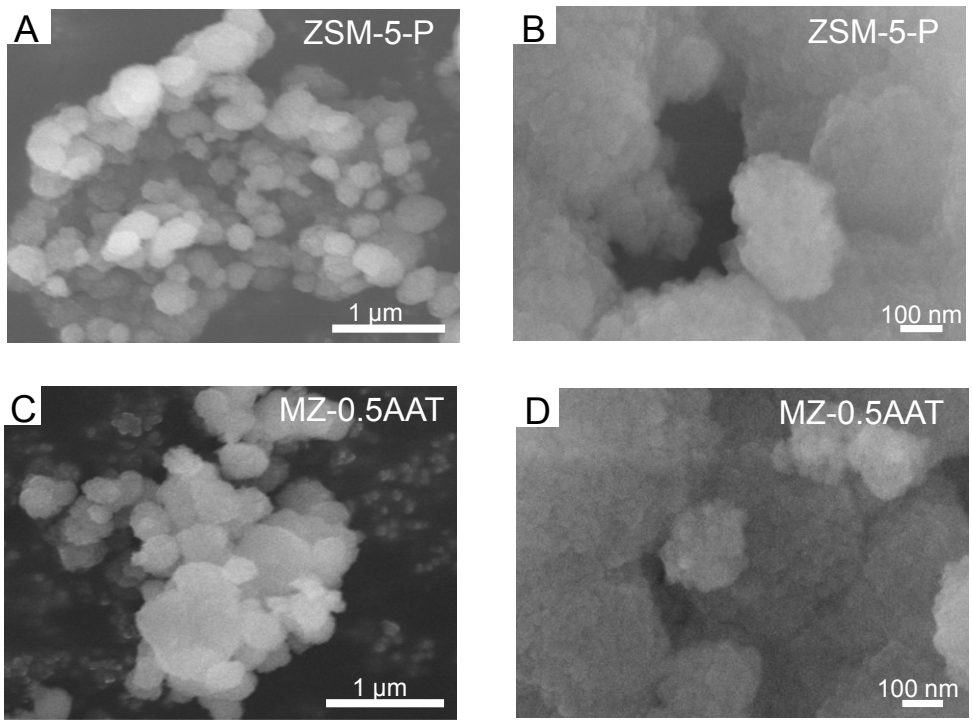

Figure 4.3 SEM images of ZSM-5-P and MZ-0.5AAT: (A, C) low magnification and (B, D) high magnification.

To study the changes in morphology, SEM and TEM analyses were performed on the representative sample MZ-0.5AAT. Apparently the morphology of ZSM-5-P remains unchanged upon the alkaline-acid treatment as can be judged from the SEM images of ZSM-5-P (Figure 4.3 A, B) compared to those of MZ-0.5AAT (Figure 4.3 C, D). However, some changes in the particle morphology are visualized in the TEM images of MZ-0.5AAT (Figure 4.4 C, D). At low magnification, the edge part of particles looks to be deformed (Figure 4.4 C) while the TEM image at high magnification (Figure 4.4 D) reveals clearly the formation of intracrystalline mesopores (note the white arrows).

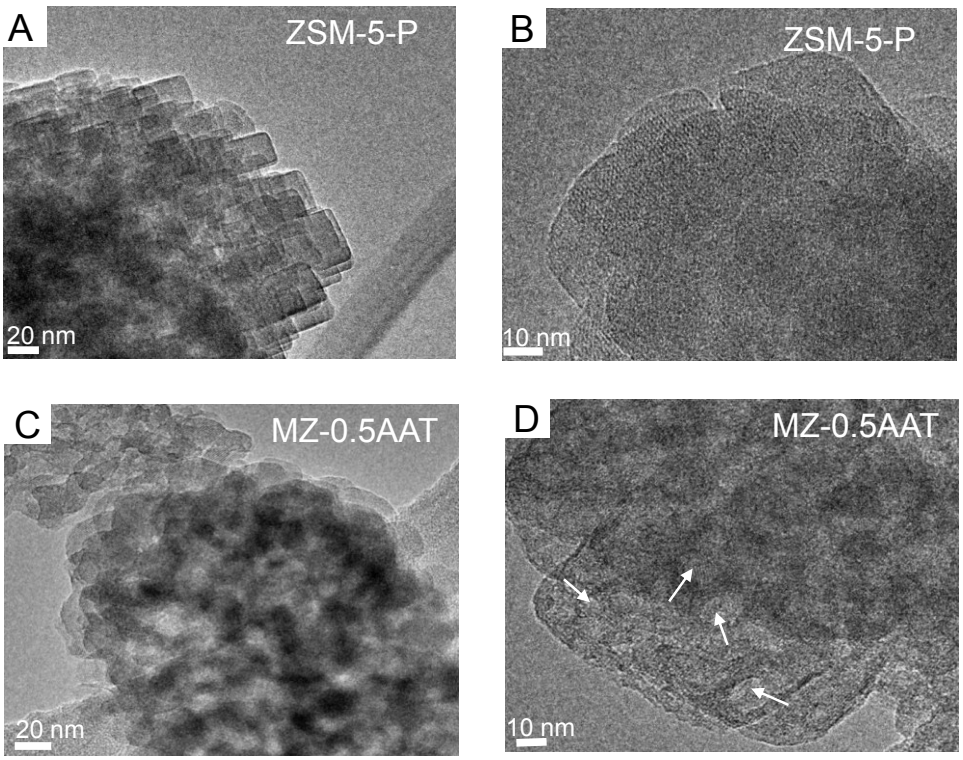

Figure 4.4 TEM images of ZSM-5-P and MZ-0.5AAT: (A, C) low magnification and (B, D) high magnification.

4.2 Acidity study

The changes in the acidic properties upon base and subsequent acid treatment of Al-rich ZSM-5 were studied by NH_3-TPD. This technique provides information on the number and strength of acid sites. The data are shown in Figure 4.5 and Table 4.1.

The NH_3-TPD profile of the starting material ZSM-5-P exhibits two distinct desorption peaks. The low temperature peak (LTP, ca. 200 °C) corresponds to NH_3 adsorbed on weak acid sites, whereas the high temperature peak (HTP, ca. 450 °C) arises from NH_3

liberated from strong acid sites. A mild alkaline treatment (0.1 M NaOH) increases the HTP intensity compared to that of ZSM-5-P, suggesting a larger fraction of strong acid sites in MZ-0.1AT. It can be explained by the fact that the commercial ZSM-5-P often contains some amorphous parts that can easily be washed out during the mild base treatment (0.1 M NaOH) while the zeolite framework is hardly affected, leading to a better crystallinity in the resulting product [91].

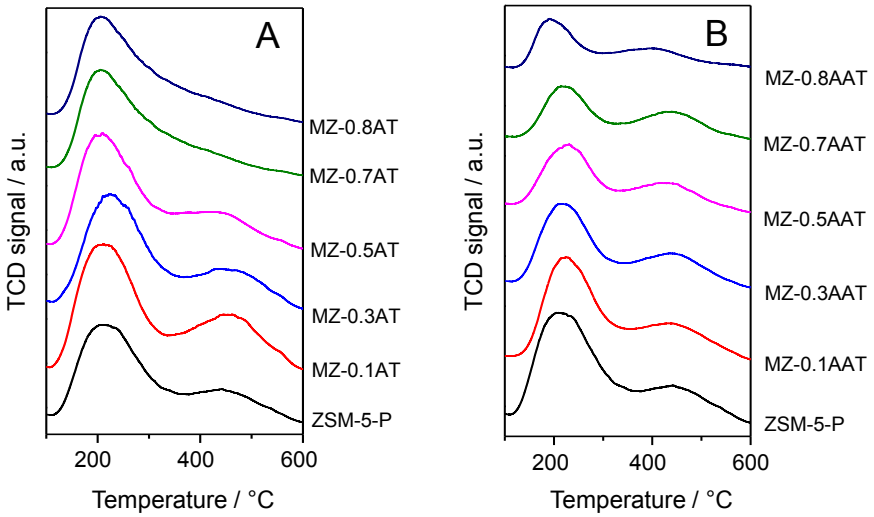

Figure 4.5 NH_3-TPD profiles of parent (ZSM-5-P) and treated samples: (A) alkaline treated MZ-xAT and (B) alkaline-acid treated MZ-xAAT.

Increasing the severity of alkaline treatment, however, the intensity of the HTP shows a gradual decline, suggesting the loss of strong acid sites. It has been reported that dealumination of framework Al (FAl) to extra-framework Al (EFAl) occurs significantly at higher base concentrations (> 0.3M) [92,93], thereby reducing the concentration of strong framework acid sites. Indeed, the NH_3-TPD profiles of MZ-0.7AT and MZ-0.8AT exhibit only one LTP (ca. 200 °C) with tailing. The total acidity of MZ-xAT estimated from the peak area in the NH_3-TPD profiles is presented in Table 4.1. The variations in the amount of acid sites strongly support the formation of EFAl at higher NaOH concentrations, being consistent with the previous work [93].

Upon the subsequent strong acid washing of MZ-xAT, the HTP intensity of the resulting MZ-xAAT increases, particularly for MZ-0.7AAT and MZ-0.8AAT, implying that the contribution of strong acid sites has been largely restored (Figure 4.5 B). However, the total acidity of MZ-xAAT drops considerably with rising alkaline concentrations in the first step (Table 4.1). These findings mean that EFAl (aluminum debris) has created acidity, but majorly weak and medium acid sites. Thus, the complete removal of aluminum debris by

the strong acid treatment induces a decreased total acidity, but an increased contribution of strong acid sites.

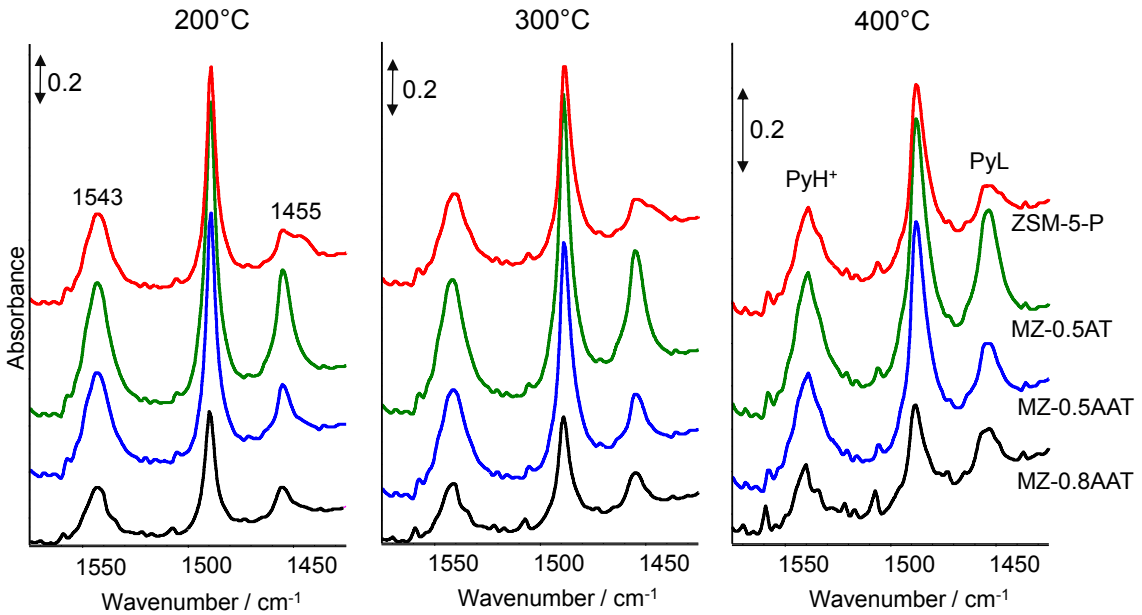

Figure 4.6 py-IR spectra of ZSM-5-P, MZ-0.5AT, MZ-0.5AAT and MZ-0.8AAT samples after evacuation at 200, 300 and 400 °C.

To obtain a better understanding of these changes in the acidic properties, IR spectra of adsorbed pyridine (py-IR) were measured on the representative samples: ZSM-5-P, MZ-0.5AT, MZ-0.5AAT and MZ-0.8AAT. After the adsorption procedure and evacuation at 200, 300 and 400 °C, the IR spectra of pyridine adsorbed on these samples (Figure 4.6) display two bands responsible for adsorbed pyridine. The band at ca. 1543 cm^{-1} is attributed to the pyridinium cation and indicates Brønsted acid sites (PyH^+, BS), while the band at ca.1455 cm^{-1} is characteristic of pyridine coordinated to Lewis acid sites (PyL, LS). The quantitative estimation of BS and LS was obtained by normalizing the integral intensity of the corresponding bands to the BET surface area (Table 4.2). In good agreement with the NH_3-TPD data, MZ-0.5AT exhibits a similar total number of BS and LS (after evacuation at 200 °C) compared to ZSM-5-P. However, an increased fraction of LS at the expense of BS density for MZ-0.5AT clearly indicates the formation of EFAl during alkaline treatment. The desorption temperature increases from 200 to 400 °C, and approximately 50% amount of pyridine chemisorbed on BS of ZSM-5-P and MZ-0.5AT is retained. This suggests that the strong intrinsic BS of ZSM-5 are mainly preserved upon the optimized alkaline treatment.

Table 4.2 Normalized integral intensities of pyridine adsorption bands over ZSM-5-P, MZ-0.5AT, MZ-0.5AAT and MZ-0.8AAT upon evacuation at 200, 300 and 400 °C

Sample	200°C			300°C			400°C		
	B	L	B/L	B	L	B/L	B	L	B/L
ZSM-5-P	1.48	0.59	2.5	1.20	0.43	2.7	0.84	0.30	2.7
MZ-0.5AT	1.38	0.63	2.2	1.13	0.54	2.0	0.65	0.40	1.6
MZ-0.5AAT	1.05	0.25	4.1	0.89	0.22	4.0	0.62	0.18	3.4
MZ-0.8AAT	0.52	0.16	3.1	0.40	0.16	2.4	0.24	0.15	1.6

B, L are the integral band intensities of pyridine adsorbed on Brønsted acid sites (1543 cm^{-1}) and Lewis acid sites (1455 cm^{-1}) normalized to the BET surface areas respectively ($\times 10^{-2}$, a.u.).

The strong acid washing primarily reduces the surface density of LS (by approximately 60%) because of the removal of Al-amorphous debris. Accordingly, a sharp rise in the BS-to-LS ratio has been attained for MZ-0.5AAT, independent of desorption temperature, further confirming an enhanced contribution of strong BS upon the strong acid treatment (Table 4.2). These results are nicely consistent with the work of Milina et al. [92] who found that the acid treatment of alkaline treated ZSM-5 increased the fraction of strong BS. Since zeolite catalysis mainly involves BS as active sites, the subsequent strong acid washing should be applied to improve the active site effectiveness upon base treatment of Al-rich ZSM-5. For MZ-0.8AAT, although strong BS are restored largely, the amount of both BS and LS suffers a significant decrease compared to that of parent ZSM-5, possibly because of the substantial destruction of the zeolite structure.

4.3 Catalytic cracking of cumene and TIPB

The catalytic performance of parent ZSM-5 (ZSM-5-P) and the final mesoporous ZSM-5 samples (MZ-xAAT) was evaluated in the gas phase cracking of cumene and 1,3,5-triisopropylbenzene (TIPB) as probe reactions to visualize the changes in the textural and acidic properties upon the base-acid treatment. The alkaline treated samples MZ-xAT were not submitted to these probe reactions because they are generally less active than the alkaline-acid treated samples as well-acknowledged in the literature [67,90,92].

Cumene cracking is an established test reaction for the estimation of strong Brønsted acidity. With its molecular cross-section of 0.5 nm, cumene can penetrate the micropores of ZSM-5 wherein most active BS are located. However, even when cumene molecules readily enter ZSM-5 crystals, the pore diffusion might be relatively slow, which leads to the low catalyst utilization and thereby consequent catalytic activity [94,95]. Thus, in this work the cumene cracking over ZSM-5-P and MZ-xAAT catalysts was run at 250 °C to evaluate the influence of both acidic properties and mesoporosity on their catalytic performance

because the overall cracking reaction rate of cracking is likely to be determined by the diffusion rate at such low temperature [94]. The effect of thermal cracking was checked with an inert material (glass beads). No cumene conversion was evidenced over glass beads under the studied reaction conditions. With the presence of the catalysts, cumene was mostly dealkylated on BS to form benzene as a main product, suggesting that BS are at play in this reaction [96].

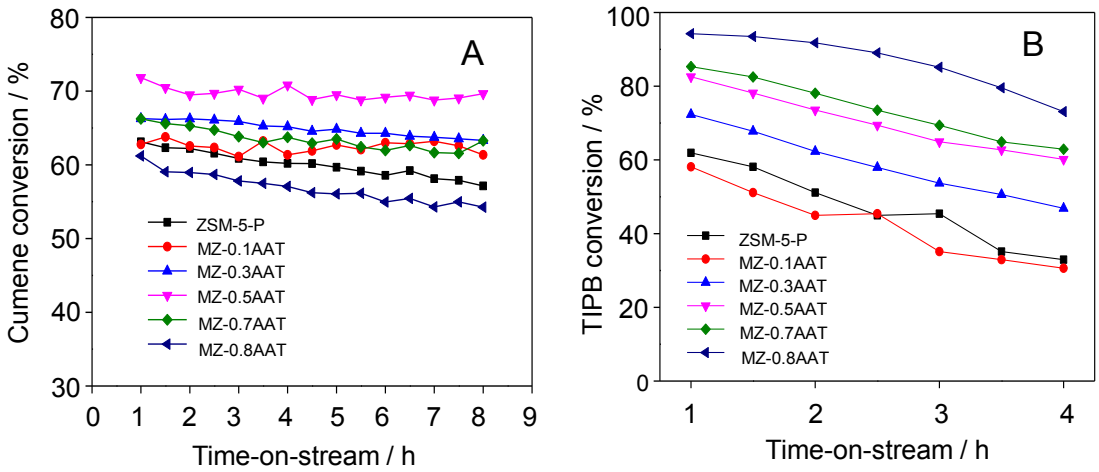

Figure 4.7 Conversion of the respective hydrocarbon in the cracking of (A) cumene and (B) TIPB over ZSM-5-P and MZ-xAAT with time-on-stream. Reaction conditions: ambient pressure, 250 °C (cumene) or 300 °C (TIPB), WHSV = 3.0 h^{-1} (cumene) or 1.0 h^{-1} (TIPB).

Table 4.3 Catalytic activities of ZSM-5-P and MZ-xAAT in the cracking of cumene and TIPB in relation to their acidic properties.

Sample	Total acidity[a]	Strong BS[b]	Cumene conversion[c], %	TIPB conversion[c], %
ZSM-5-P	1.24	0.84	63.1	61.9
MZ-0.1AAT	0.98	n.a.	62.9	58.1
MZ-0.3AAT	0.85	n.a.	66.1	72.3
MZ-0.5AAT	0.71	0.62	71.8	82.5
MZ-0.7AAT	0.50	n.a.	66.3	85.3
MZ-0.8AAT	0.42	0.24	61.2	94.2

[a]NH_3-TPD; [b]strong BS defined as the normalized integral band intensities of pyridine adsorbed on BS (1543 cm^{-1}) after evacuation 400 °C (×10^{-2} a.u.); [c]cumene and TIPB conversions after 1 h on-stream. Reaction conditions: ambient pressure, 250 °C (cumene) or 300 °C (TIPB), WHSV = 3.0 h^{-1} (cumene) or 1.0 h^{-1} (TIPB).

Figure 4.7 A presents the cumene conversion over the various catalysts with time-on-stream. As expected, mesoporous MZ-xAAT catalysts show higher cracking activities than parent ZSM-5-P, except MZ-0.8AAT. Remarkably, MZ-0.5AAT displays the highest cumene conversion which looks almost stable within the initial 8 hours on-stream. Table

4.3 summarizes the cumene conversion over ZSM-5-P and MZ-xAAT after 1 h on-stream with respect to their acidic properties. No strong relationship between the cumene conversion and the acid density, particularly strong BS can be found, suggesting that there are diffusional transport constraints affecting cumene reactivity under the tested conditions.

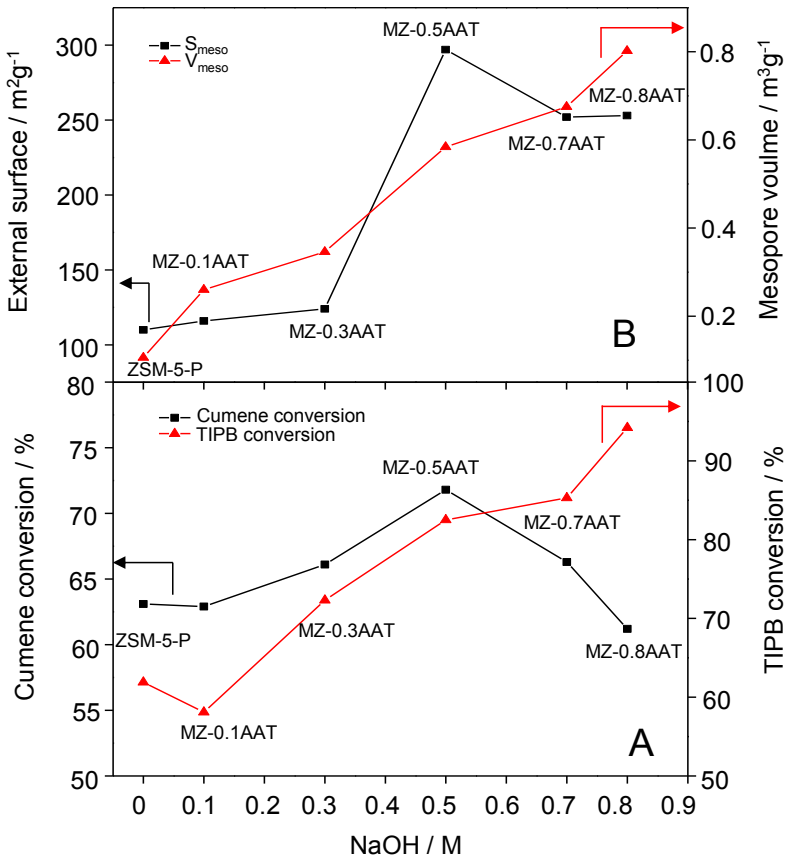

Figure 4.8 Cumene and TIPB conversions over ZSM-5-P and MZ-xAAT with respect to their mesoporosity as a function of NaOH concentrations. Reaction conditions: ambient pressure, 250 °C (cumene) or 300 °C (TIPB), WHSV = 3.0 h^{-1} (cumene) or 1.0 h^{-1} (TIPB).

To elucidate such effects, the cumene conversion over various catalysts and their mesoporosity are plotted as a function of NaOH concentrations used in the first step (Figure 4.8). Interestingly, a good correlation between the cumene conversion and external surface has been found. However, this relationship is not proportional, indicating that both mesoporosity and acidity are of importance in the cracking of cumene. Compared to parent ZSM-5, MZ-0.1AAT yields a similar cumene conversion of approximately 63% due to the minor changes in the acidic properties and limited mesoporosity development caused by the mild base treatment (0.1 NaOH) in the first

step. With increasing mesoporosity formation (larger external surfaces), MZ-0.3AAT and MZ-0.5AAT catalysts become more active, giving cumene conversions of 66.1% and 71.8%, respectively, even though they possess a lower density of acid sites, particularly strong BS than the first two samples as shown by the data of NH_3-TPD and py-IR. These results agree well with the work of Zhao et al. [83] who found that the diffusion rate of cumene in mesoporous ZSM-5 is by 2-3 orders of magnitude faster than that in conventional ZSM-5, which doubled the cumene conversion over mesoporous ZSM-5 despite the lower Brønsted acidity. Al-Khattaf et al. [97] reported that under the diffusion-controlled regime, the larger the external surface, the higher the catalyst effectiveness and consequently the catalytic activity. Taking these findings into account, the improved cumene conversion over the mesoporous ZSM-5 samples in this work can be attributed to the enhanced acid site utilization due to the increased accessibility and physical transport provided by substantial mesoporosity. For MZ-0.8AAT, the cumene conversion drops though considerable mesopores are already available. The lower activity of MZ-0.8AAT can be explained by a sharp decrease in its surface density of strong BS in this sample as confirmed by the py-IR data. Hence, the introduction of mesoporosity coupled to the preservation of microporous characteriestics, i.e. strong BS plays a key role for the superior catalytic activity in a strong acid catalyzed reaction like cumene cracking under the diffusion-controlled reaction conditions.

Since cumene cracking only assesses the catalytic activity of strong BS primarily located in the micropores of ZSM-5, TIBP cracking was carried out to obtain information on the catalytic activity of BS located solely on the external surface generated by base-acid treatment. With a molecular cross-section of 0.74 nm, TIPB cannot enter the micropores of ZSM-5 (less than 0.56 nm); therefore the catalytic activity in the TIPB cracking reflects the external surface activity. The TIPB cracking reaction was performed at 300 °C to eliminate the effect of thermal cracking. Di-isopropylbenzene was found to be a main product, indicating that the chosen conditions for the TIPB cracking reaction favor the first dealkylation step [98]. Figure 4.7 B depicts the TIPB conversion over the various catalysts with time-on-stream which indicates that mesoporous MZ-xAAT catalysts are more active than parent ZSM-5-P except MZ-0.1AAT. It is worth noting that MZ-0.8AAT shows the highest TIPB conversion with the slowest deactivation rate even though this sample has the smallest density of BS. The TIPB conversion over ZSM5-P and MZ-xAAT upon 1 h on-stream (Table 4.3) varies in a reverse trend with the density of acid sites, particularly of BS. On the other side, it is apparent from Figure 4.8 that the TIPB conversion increases with the external surface, being consistent with the work of Mochizuki et al. [93]. However, the TIPB conversion over MZ-0.7AAT and MZ-0.8AAT

deviates from this trend, suggesting that larger pores are more beneficial for conversion of bulky molecules, the conversion of which is heavily hindered by steric constraints. These results indicate that upon the alkaline-acid treatment, the BS are enriched on the external surface whose accessibility is facilitated by the larger mesopores. On the other hand, it should be noted that TIPB can be easily activated even by weak BS. Therefore, the information on the strength of the external BS cannot be derived from the cracking of TIPB, and the characterization of such external active sites remains a challenge.

4.4 Summary and conclusions

Thus, it is possible to prepare mesoporous ZSM-5 materials with high mesoporosity coupled to the preservation of intrinsic zeolite characteristics from Al-rich ZSM-5 by means of optimization of alkaline treatment and subsequent strong acid washing. Appropriately used NaOH concentrations in the first step determine the mesoporosity development while a second strong acid washing step is required to improve the physicochemical properties of the final mesoporous ZSM-5 material. A mild alkaline treatment of Al-rich ZSM-5 and subsequent strong acid washing has minor effects due to little extraction of silicon and aluminum from the zeolite framework (MZ-0.1AAT and MZ-0.3AAT). A severe base treatment, in contrast, causes an excessive dissolution of zeolite crystals, resulting in a drastic reduction in the BET surface area, micropore volume and acidic strength (MZ-0.7AT and MZ-0.8AT). Although a subsequent strong acid treatment enables the restoration of these intrinsic microporous properties to certain extent, the recovery yield from preparation and total acidity drop dramatically (MZ-0.8AAT). Most notably, the alkaline treatment of Al-rich ZSM-5 in 0.5 NaOH, followed by the strong acid washing in 0.5 M HCl, was found to be optimal for the preparation of mesoporous ZSM-5 materials (MZ-0.5AAT) containing substantial mesoporosity (S_{meso} = 297 m^2/g) with the preserved intrinsic zeolite features (e.g. V_{mico} = 0.13 cm^3/g, B/L ratio = 4.1) and a relatively high recovery yield (62%).

Cumene cracking over parent ZSM-5 and the final mesoporous ZSM-5 catalysts (MZ-xAAT) reveals that the presence of mesoporosity indeed increases cumene reactivity of the MZ-xAAT catalysts in the diffusion-controlled regime as their densities of zeolite BS are mainly retained. The catalytic activity of the external surface was probed by TIPB cracking which indicates that the formation of larger pores and the enrichment of BS on the external surface caused by the base-acid treatment are favorable for conversion of large molecules like TIPB.

Chapter 5

Direct Synthesis of Nano-ZSM-5/SBA-15 Analog Composites from ZSM-5 Precursors

Chapter 5 explores high-temperature synthesis of nano-sized ZSM-5/SBA-15 analog composites from ZSM-5 nanoseeds. This chapter starts with the description of the optimization of pH values for the preparation of a highly condensed, ordered mesoporous SBA-15 analog from ZSM-5 precursors under hydrothermal treatment at elevated temperature. Then the precrystallization time period of initially formed ZSM-5 precursors controlling the distribution of ZSM-5 phase and SBA-15 analogs phase is thoroughly discussed. The steaming stability and catalytic activity in the gas phase cracking of cumene and TIPB as probe reactions are ultimately presented.

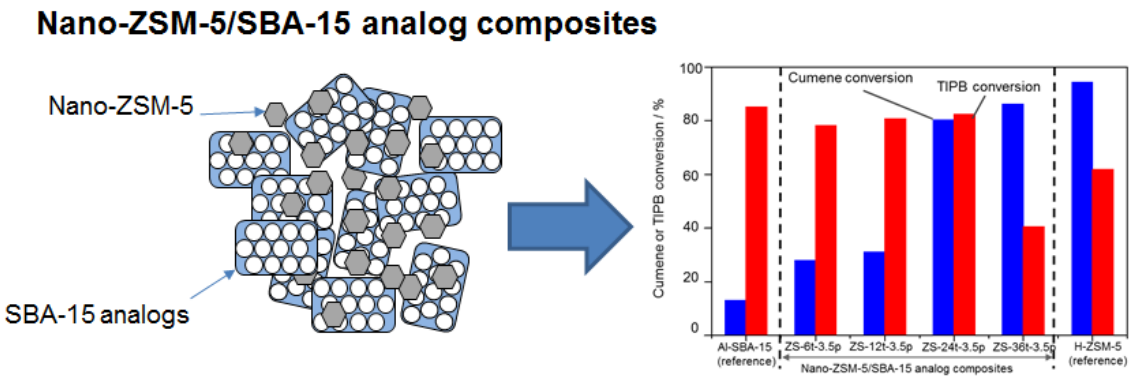

5.1 Evolution of precursors to zeolite crystals

Understanding of the evolution of nano-scale precursors ("nanoseeds") to zeolite crystals during the precrystallization process is of fundamental importance for the preparation of novel hierarchical materials. In the present work, the ZSM-5 seed solution was preheated at 90 °C in a reflux system for different time periods and the evolution of precursor nanoclusters to zeolite crystals was monitored by WAXS (Figure 5.1).

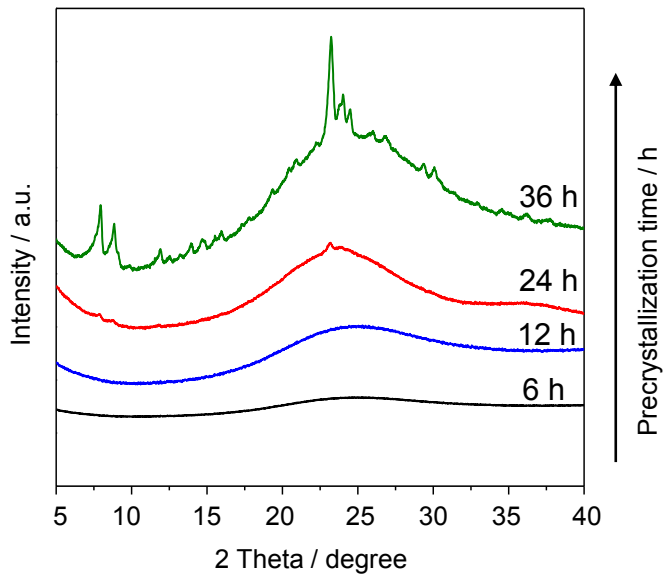

Figure 5.1 WAXS patterns of the ZSM-5 precursor solution after precrystallization for 6 h, 12 h, 24 h and 36 h.

As can be seen from Figure 5.1, within short precrystallization periods (6 h, 12 h) crystalline ZSM-5 nanoparticles do not form, as confirmed by absence of reflections in the WAXS patterns. Extending the reaction time to 24 h, the first indications of ZSM-5 crystals appear with the small typical reflections of MFI topology at 2θ = 8.0°, 8.8° and 23.1°. This indicates that the formation of ZSM-5 nanocrystals proceeds progressively with the precrystallization time, leading to an adequate crystalline phase that can be detected by WAXS [99]. These MFI reflections look well developed upon aging for 36 h, suggesting a dominant fraction of ZSM-5 nanocrystals. Thus, the formation and content of crystalline ZSM-5 phase in the seed solution, to certain extent, can be controlled by adjusting the precrystallization time. These findings offer possibilities for tuning the content of ZSM-5 nanocrystals to desired values with respect to the mesoporous matrix that can be directly developed from unreacted precursors in a subsequent step [76,100].

5.2 Effect of the pH value during hydrothermal treatment (htt-pH)

To avoid the further evolution of zeolite precursors to bulky zeolite crystals, several attempts focused on the self-assembly of these precursors with surfactant templates in strongly acidic media at mild temperatures (typically 100-150 °C) [53]. However, the resulting mesoporous materials like MSU-S [69] or MAS-9 [70] still exhibit poor hydrothermal stability and acidity because the amount of incorporated aluminum (ruling acidity) and the condensation degree of mesoporous walls (ruling stability) are low. In order to improve the named properties of mesoporous materials assembled from ZSM-5 nanoseeds, this work aims at increasing a) the silica condensation degree and b) the incorporated aluminum content in the mesoporous walls by pH adjustment prior to hydrothermal treatment at high temperature (200 °C). The seed suspension precrystallized for 6 h is employed as model precursor because after such a short aging time the seed solution obviously contains a large amount of unreacted precursors (as shown by the WAXS data) that can be used for the subsequent self-assembly of a mesostructure [101].

5.2.1 Effect of the htt-pH on the structural and textural properties

It has been reported that the acidity of the synthesis solution is a decisive factor for not only the mesoporous regularity but also the successful incorporation of aluminum into the SBA-15 framework [80,102]. Therefore the effect of the htt-pH on the preparation of SBA-15 analogs from ZSM-5 precursors at 200 °C was investigated systematically. The structural and textural properties of the resulting materials were characterized by SAXS, N_2 adsorption/desorption and TEM. The results are shown in Figures 5.2, 5.3 and Table 5.1.

Table 5.1 Effect of the htt-pH on the structural and textural properties of ZS composites.

Sample	d_{100} (nm)	a_0 (nm)	D_p (nm)	W (nm)	S_{BET} (m^2/g)	V_t (cm^3/g)
ZS-6t-1.5p	11.1	12.9	9.0	3.9	424	1.05
ZS-6t-2.5p	11.2	12.9	9.1	3.8	412	1.10
ZS-6t-3.5p	11.2	12.9	9.1	3.8	372	0.97
ZS-6t-4.5p	11.2	12.9	9.1	3.8	297	0.80
ZS-6t-5.5p	11.1	12.9	-	-	184	0.77

d_{100}: spacing value; a_0: unit cell parameter ($a_0 = 2 \times d_{100}/3^{1/2}$); D_p: pore diameter; W: pore wall thickness ($W = a_0 - D_p$); V_t: total pore volume. The missing parameters are due to the absence of an ordered mesostructure.

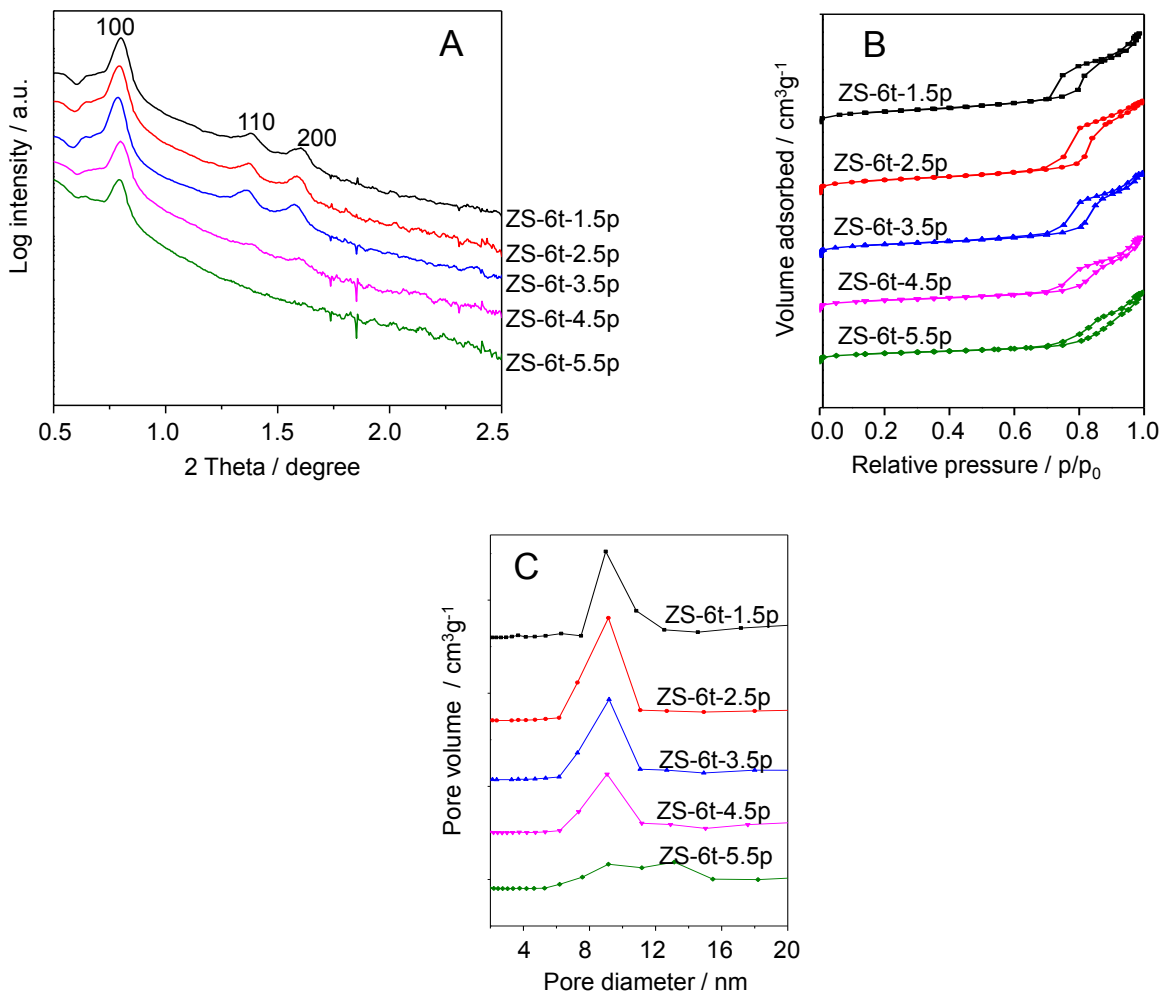

Figure 5.2 Effect of the htt-pH on the structural and textural properties of ZS composites: (A) SAXS patterns, (B) N_2 sorption isotherms and (C) the corresponding pore size distribution curves.

From the SAXS patterns (Figure 5.2 A) it can be seen that the samples prepared at lower htt-pH values in the second step (ZS-6t-1.5p, ZS-6t-2.5p, ZS-6t-3.5p) show three well-resolved reflections indexed as the 100, 110 and 200 reflections of 2D hexagonal (p6mm) symmetry, indicating an ordered mesostructure. As increasing the htt-pH value to 4.5 (ZS-6t-4.5p) or 5.5 (ZS-6t-5.5p), the 110 and 200 reflections become much less pronounced, suggesting the formation of a disordered mesostructure. These results demonstrated that the htt-pH significantly impacts on the ordering of mesostructures, which is in accordance with the report by Pan et al. [80] using conventional silica precursors. On the other hand, it is worthy to note that the reflection angles shift very slightly over the whole range of the studied htt-pH values, implying that the unit cell dimension of the formed mesostructure seems to be not affected by the htt-pH.

The data of N_2 adsorption/desorption are also in accordance with those of SAXS. As

depicted in Figure 5.2B, all ZS-6t-yp series exhibit type IV isotherms with H1-type hysteresis loop, confirming their mesoporous nature. However, the capillary condensation steps of ZS-6t-1.5p, ZS-6t-2.5p and ZS-6t-3.5p are very steep and occur in the relative pressure (p/p_0) range of 0.7-0.9, which is characteristic of an ordered mesostructure with a large and uniform pore size. The two latter samples (ZS-6t-4.5p, ZS-6t-5.5p) display a less steep hysteresis loop being indicative of a disordered mesopore arrangement [80,81]. There are no obvious increases in the N_2 uptake at low relative pressure (p/p_0 <0.01), suggesting the complete absence or presence of a very small fraction of micropores in ZS-6t-yp samples. The dimension and uniformity of mesopores can be directly reflected by the pore size distribution (Figure 5.2C). With increasing pH values used in the hydrothermal treatment step, the pore size distribution becomes broader. The pore size and pore wall thickness of the first four samples (pH = 1.5−4.5) was estimated to be about 9.0−9.1 nm and 3.76-3.85 nm (Table 5.1). Compared to those of MAS-9 (8.0 and 5.4 nm respectively) [70] prepared at a lower temperature (100 °C), these results imply that the silica based walls of the ZS composites have been further condensed under the hydrothermal treatment at 200 °C, being similar to the reported works [80,103]. For ZS-6t-5.5p, the mesoporous framework has been partially destroyed and therefore its pore size cannot be calculated. The disordered mesostructure of ZS-6t-4.5p and ZS-6t-5.5p is also evidenced by their relatively low surface areas and pore volumes compared to those of the three other samples. As summarized in Table 5.1, ZS-6t-1.5p, ZS-6t-2.5p and ZS-6t-3.5p show the BET specific surface areas ranging from 424 to 372 m^2/g and pore volumes from 1.10 to 0.97 cm^3/g, whereas these textural parameters drop to 279 m^2/g and 0.80 cm^3/g for ZS-6t-4.5p and 184 m^2/g and 0.77 cm^3/g for ZS-6t-5.5p. Hence, in order to obtain ordered mesoporous SBA-15 analogs, the htt-pH value should not be higher than 3.5. According to Pan et al. [80], the surfactant-silanol interaction becomes weak at higher pH values, reducing the surfactant content adsorbed within the pores and incorporated into the walls. As a result, the mesostructure partially collapsed as the framework shrinkage occurred at high temperature (200 °C).

The ordered mesostructure can be visualized by TEM analysis, as the stability of the samples at the TEM conditions was high enough to study their original state. The TEM images of the representative sample ZS-6t-3.5p exhibit well-ordered hexagonal arrays of mesopores with one-dimensional channels taken in [100] and [110] directions (Figure 5.3 A and B respectively). From the bright-dark contrast in the TEM image in Figure 5.3 A, the mesopore size and wall thickness can be estimated to be about 8.6 nm and 3.7 nm, respectively, which are comparable to the data of SAXS and N_2 adsorption/desorption (Table 5.1).

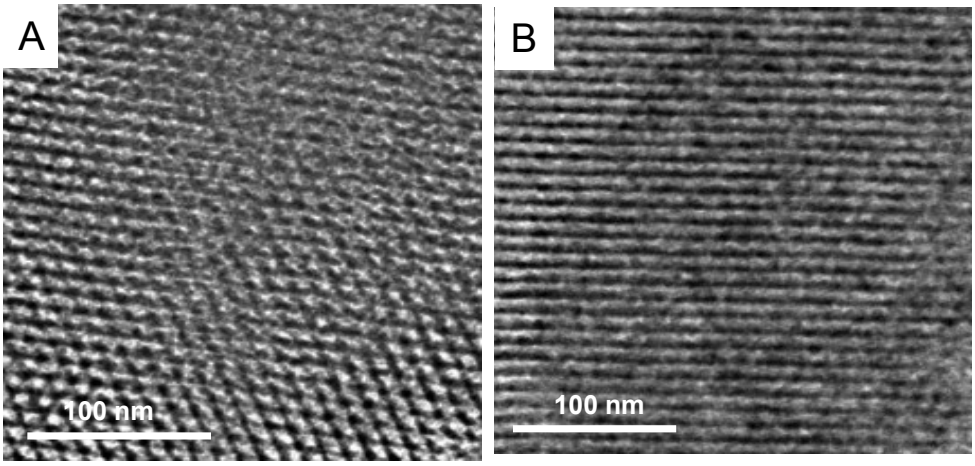

Figure 5.3 TEM images of ZS-6t-3.5p viewed along [100] (A) and [110] (B) directions.

5.2.2 Effect of the htt-pH on the acidic properties

The influence of the htt-pH on the total number and strength of acid sites was studied by NH_3-TPD. The data are presented in Figure 5.4 and Table 5.2 together with the elemental composition.

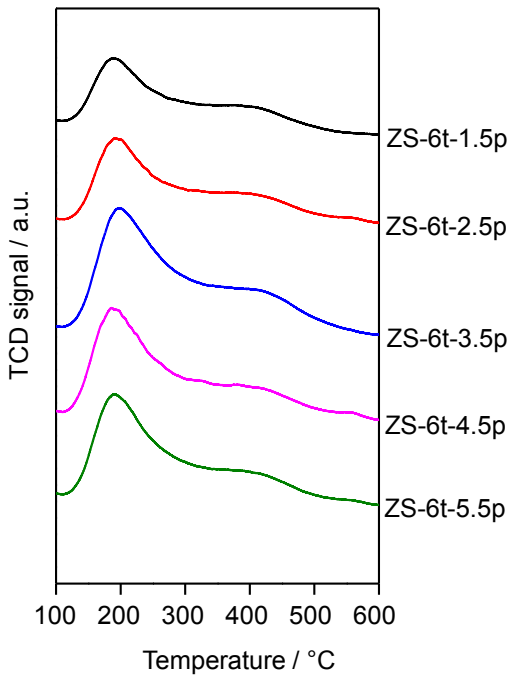

Figure 5.4 NH_3-TPD profiles of ZS composites prepared at different htt-pH values.

In general, the NH_3-TPD profiles of ZS-6t-yp series exhibit two desorption peaks (Figure 5.4). The first sharp peak around 200 °C can be attributed to weak acid sites, while the broader peak in the range of 300-500 °C shows the presence of medium and strong acid sites. The quantitative analysis shows that the total acidity (Table 5.2) rises considerably with the htt-pH value increase. The total acidity of ZS-6t-5.5p (0.35 mmol NH_3/g) is two times greater than that of ZS-6t-1.5p (0.16 mmol NH_3/g). This can be ascribed to larger amounts of incorporated aluminum at higher htt-pH values, as confirmed by elemental analysis, which give rise to more acid sites in the final products (Table 5.2). Remarkably, in the htt-pH range of 3.5-5.5 almost all aluminum added to the initial zeolite seed solution has been effectively introduced into the mesoporous walls of the ZS composites. For example, ZS-6t-3.5p has a Si/Al ratio = 34 in the product, which is very close to the Si/Al ratio = 30 in the initial gel. In contrast, MAS-9 prepared in strong acidic media showed a relatively low aluminum content; for example, the Si/Al ratio in the initial gel of 60 resulted in a product with Si/Al = 256 [104].

Table 5.2 Effect of the htt-pH on the elemental composition and total acidity of ZS composites.

Sample	Si/Al ratio in gel	Si/Al ratio in products[a]	Total acidity (mmol NH_3/g)[b]
ZS-6t-1.5p	30	67	0.16
ZS-6t-2.5p	30	40	0.22
ZS-6t-3.5p	30	34	0.26
ZS-6t-4.5p	30	32	0.27
ZS-6t-5.5p	30	29	0.35

[a]Si, Al content in the products analyzed by AAS and ICP, respectively; [b]NH_3-TPD.

It is generally accepted that the aluminum incorporation into the final product is favored in less acidic media. At lower htt-pH values, the Al-O-Si bonds in the ZSM-5 precursors might get hydrolyzed, causing the leaching of Al during the hydrothermal treatment. Consequently, the total acidity drops in the samples synthesized at lower pH values. On the other hand, the increase of pH values over 3.5 brought about less ordering of mesostructures. Thus, the htt-pH 3.5 is considered as optimal under the studied conditions in terms of increased total acidity and preservation of highly condensed ordered mesostructures.

5.3 Effect of the precrystallization time

After optimizing the htt-pH, the next step was to explore the preparation of nano-ZSM-

5/SBA-15 analog composites with controlled distribution of microporous and mesoporous domains derived from ZSM-5 precursors. This can be achieved by varying the precrystallization time (6-36 h) in the first step to yield the precursor solutions containing different fractions of nano-ZSM-5. Then high-temperature hydrothermal treatment at the optimized pH value is applied to convert the fraction of precursors that has not been consumed in the first step to an ordered mesoporous SBA-15 analog that surrounds and disperses the initial ZSM-5 nanocrystals.

5.3.1 Effect of the precrystallization time on the morphology, structural and textural properties

Figure 5.5 presents SAXS (A) and XRD (B) patterns of ZS-xt-3.5p series prepared from preformed ZSM-5 nanoclusters with different precrystallization times. As shown in Figure 5.5 A, the samples ZS-6t-3.5p, ZS-12t-3.5p and ZS-24t-3.5p, precrystallized for 6 h, 12 h, and 24 h, respectively, exhibit three well-resolved reflections indexed as the 100, 110, and 200 reflections of 2D hexagonal (p6mm) symmetry, indicative of a highly ordered mesostructure (SBA-15 analogs). After a more extended precrystallization of 36 h (ZS-36t-3.5p), no such reflections can be observed, suggesting the absence of an ordered mesostructure in this sample. These results indicate that the ordered mesostructure has developed from self-assembly of unreacted precursors rather than well-defined ZSM-5 nanocrystals that can be detected by WAXS (see Figure 5.1).

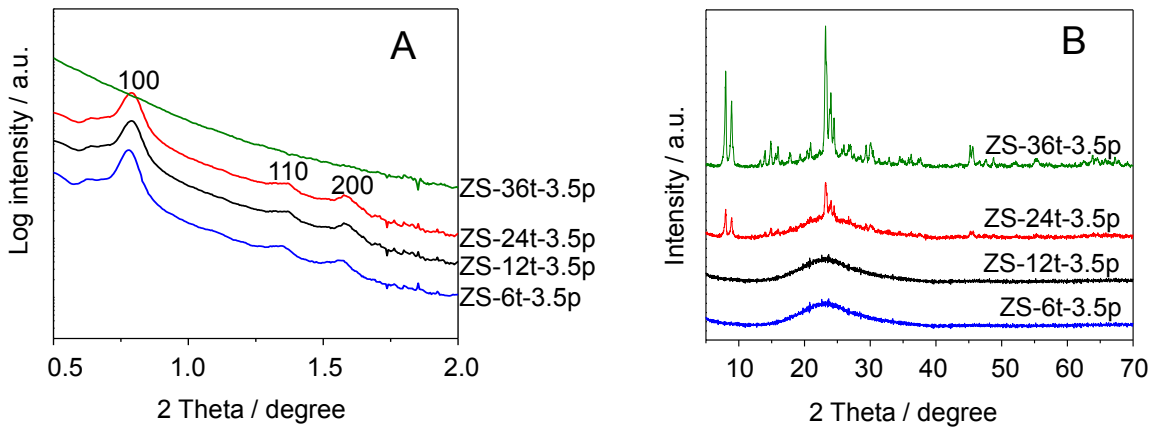

Figure 5.5 Effect of the precrystallization time on the structural properties of ZS composites: (A) SAXS and (B) XRD patterns.

Wide angle XRD patterns (Figure 5.5 B) yield complementary information on the presence of a crystalline ZSM-5 phase in the samples ZS-24t-3.5p and ZS-36t-3.5p. Both

samples show clear reflections in the 2θ regions of 8-10° and 23-25°, indicative of crystalline ZSM-5 zeolites. In contrast, no such reflections are detected in the samples ZS-6t-3.5p and ZS-12t-3.5p, implying a very low content or absence of a zeolite structure. The reflections become sharper and more prominent with increasing the precrystallization time, suggesting a better crystallinity in ZS-36t-3.5p compared to ZS-24t-3.5p.

The complementary SAXS and XRD data can be interpreted as a gradual transition from a mesoporous SBA-15 analog phase to a microporous ZSM-5 phase that is controlled by the precrystallization time applied in the ZSM-5 precursor synthesis. Controlled formation of micro-/mesoporous composites is then a question of kinetic control of the synthesis process. For the longest precrystallization time (36 h), the zeolite crystal growth consumes all precursor species; hence the mesoporous framework phase cannot be formed anymore. Contrarily, for short precrystallization times (ZS-6t-3.5p and ZS-12t-3.5p), the precursors have been hardly consumed in the zeolite formation; therefore the mesoporous frame can be formed around the zeolite domains in the second synthesis step. Thus, the final ZS-24t-3.5p sample contains sufficient amounts of ordered mesoporous SBA-15 analogs (Figure 5.5 A) and crystalline ZSM-5 (Figure 5.5 B), in order to form detectable amounts of ordered mesoporous and microporous phases. This interpretation is also in agreement with the literature, wherein precursor species that have not reacted to form zeolite crystals were described as building units for the self-assembly of a mesostructure [76,100].

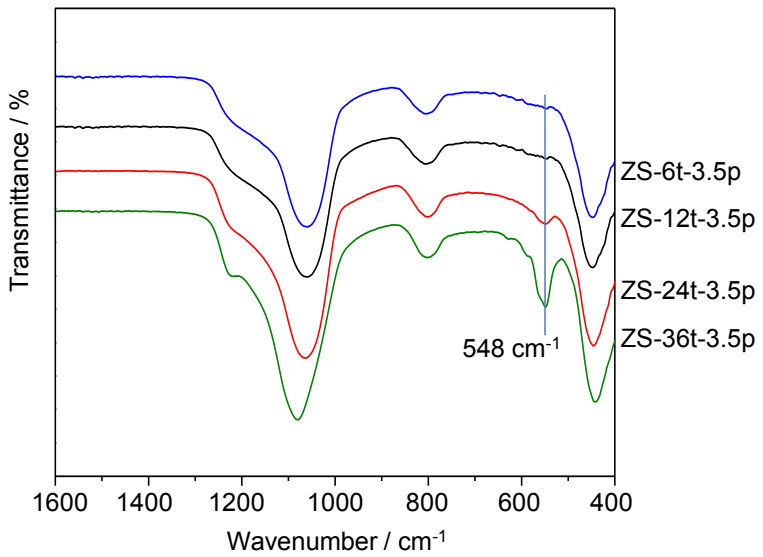

Figure 5.6 FTIR spectra of ZS composites with varying the precrystallization time.

FT-IR spectroscopy used to investigate the zeolite structure supports the outlined hypothesis. From Figure 5.6 it can be seen that ZS-36t-3.5p displays a sharp band at 548 cm^{-1}, which is assigned to asymmetric stretching mode of pentasil units in the MFI zeolite topology, indicating the relatively high ZSM-5 crystallinity [76]. The spectrum of ZS-24t-3.5p shows the same absorption band, but less pronounced, suggesting that this sample is less crystallized. In case of ZS-6t-3.5p and ZS-12t-3.5p, only a very small band at 548 cm^{-1} can be observed. It is likely that the atomic order of ZS-6t-3.5p and ZS-12t-3.5p is only in the range of few unit cells that is not adequate to be detected by XRD (Figure 5.5 B), being consistent with the results of Xiao et al. [70] and Pinnavaia et al. [71].

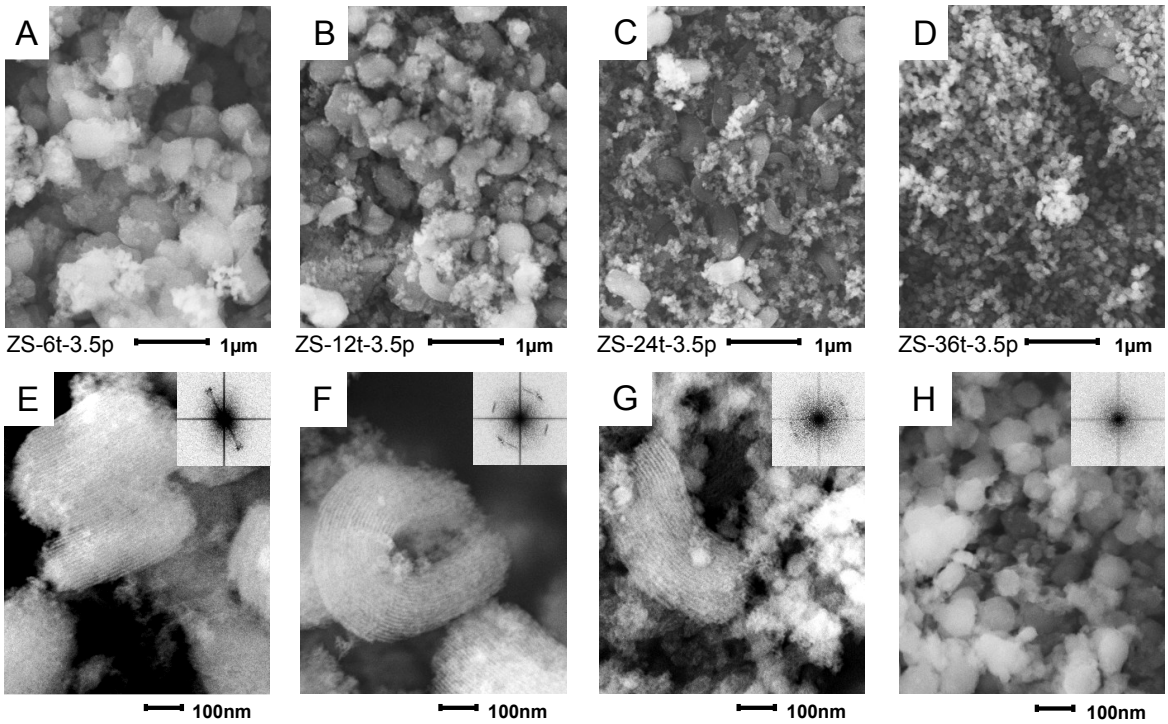

Figure 5.7 SEM images of ZS composites with precrystallization times of 6 h, 12 h, 24 h or 36 h (from left to right). SEM images with 20k magnification are shown in upper row (A-D), 100k images in lower row (E-H). Insets show FFT images of the respective SEM.

Also SEM and TEM analyses support the interpretation of a precrystallization-time controlled tuning of microporous and mesoporous phase contents. Figure 5.7 displays SEM micrographs of ZS-xt-3.5p samples synthesized with the precrystallization time periods of the ZSM-5 solution of 6 h (ZS-6t-3.5p, A/E), 12 h (ZS-12t-3.5p, B/F), 24 h (ZS-24t-3.5p, C/G) and 36 h (ZS-36t-3.5p, D/H). For each material, the SEM images at magnifications of 20k (A-D) as well as 100k (E-H) are shown along with FFT (Fast Fourier Transformations) of the 100k images to analyze the presence of ordered mesoporosity

(insets in E-H). The images for all samples indicate the presence of two different intermixed phases with clearly distinct particle sizes and particle morphology. The content of both phases clearly shifts with increasing the precrystallization time. ZS-6t-3.5p, the material with the shortest precrystallization time of the ZSM-5 seed solution shows the dominating presence of particles of about 300 to 600 nm diameter along with very small amounts of an additional phase of about 50 to 100 nm particle size (Figure 5.7 A). The entire fraction of larger particles features a distinct type of mesoporosity with parallel channels (Figure 5.7 E), a structure typical for SBA-15 type materials. The ordered pore arrangement is confirmed by FFT analysis of the corresponding SEM image (insert in Figure 5.7 E), which shows two symmetric spots corresponding well with the typical hexagonal pore arrangement. The two types of particle domains can therefore be assigned to a mesoporous phase (larger particles) and microporous zeolite phase (smaller particles).

Both types of phases are observed also in the samples synthesized with the longer precrystallization times of 12 h (Figure 5.7 B/F), 24 h (Figure 5.7 C/G) and 36 h (Figure 5.7 D/H). However, with increasing the precrystallization time, the content of mesoporous phase decreases gradually, whereas a higher content of the ZSM-5 phase is apparent (from Figure B to C and D). The ordered mesostructure is confirmed by higher resolution SEM images and corresponding FFT images for 12 h (Figure 5.7 F) and 24 h (Figure 5.7 G) precrystallization time, whereas the sample precrystallized for 36 h retains hardly any mesoporous phase (Figure 5.7 D and H, note the absence of spots in the FFT insert). Thus, the relative content of mesoporous phase and microporous zeolite phase can be easily adjusted synthetically by increasing the precrystallization time of the ZSM-5 precursor solution.

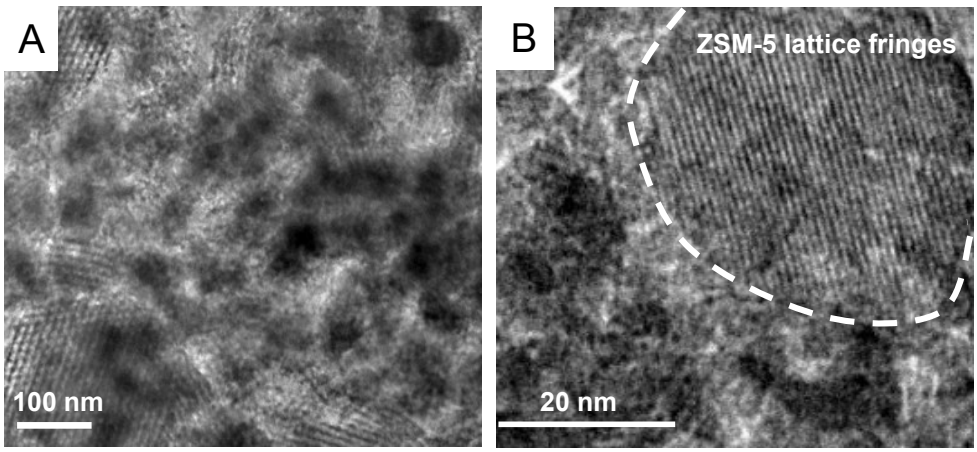

Figure 5.8 TEM images of ZS-24t-3.5p: (A) low magnification and (B) high magnification.

TEM analysis validates the phase assignments of a mesoporous phase and a microporous crystalline ZSM-5 phase. TEM images of ZS-24t-3.5p (Figure 5.8) indicate that this material consists of an ordered hexagonal mesoporous structure (pore channels clearly evident in Figure 5.8 A), coexisting with fairly uniform ZSM-5 nanoparticles (note the black domains), leading to a composite with well-dispersed nano-ZSM-5 crystals. The lattice fringe of a nano-ZSM-5 domain embedded in the mesoporous matrix is visualized through the TEM image with high magnification (Figure 5.8 B). Such close contact between ZSM-5 phase and mesoporous SBA-15 analogs phase proved to form a highly interconnected pore structure, which greatly benefits catalytic performance of the composite compared to a mechanical mixture of the corresponding individual zeolites and mesoporous materials [74,88].

The local environment of the Al and Si atoms in the representative sample ZS-24t-3.5p was investigated by ^{27}Al- and ^{29}Si-MAS-NMR spectroscopy, respectively (Figure 5.9). The ^{27}Al-MAS-NMR spectrum (Figure 5.9A) shows a dominant signal centered at approximately 53 ppm and a much weaker signal at approximately 0 ppm, which are attributed to tetrahedrally and octahedrally coordinated aluminum, respectively. This indicates that most of the aluminum is incorporated into the material framework [105].

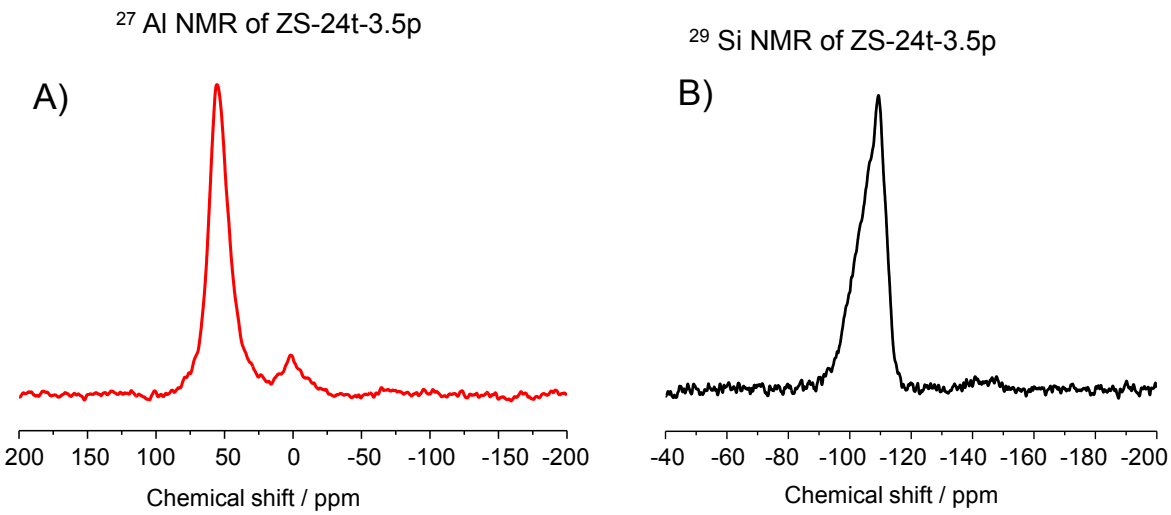

Figure 5.9 ^{27}Al- (A) and ^{29}Si- (B) MAS-NMR spectra of ZS-24t-3.5p.

From Figure 5.9 B, it can be seen that the ^{29}Si-MAS-NMR spectrum displays a dominating signal at -112 ppm due to Q4 silicon species (Si(4Si)) and a broad, low-field shoulder at -95 to -105 ppm. This shift range is typical for Q2 and Q3 silicon species Si(2Si,2OH) and Si(3Si,1OH), respectively, but also for silicon atoms with an oxygen bridge to tetrahedrally coordinated framework aluminum species (Si(3Si,1Al)). The latter

silicon species are responsible for the formation of Brønsted acid sites, e.g. in zeolite ZSM-5 [105]. Generally, the ^{29}Si-MAS-NMR spectrum indicates a high degree of silica condensation in this sample. These data clearly demonstrate the advantages of high temperature synthesis for the preparation of composite materials compared to the mild temperature synthesis whose products such as MSU-S_{BETA}/zeolite beta [100] or MCM-14/zeolite Beta [106] suffered from large fractions of octahedral aluminum and much less condensed mesoporous walls.

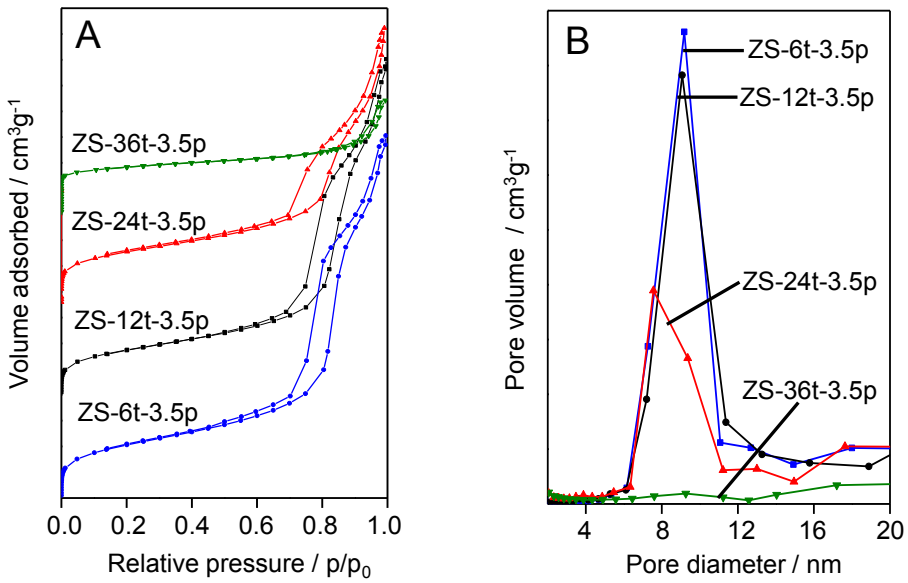

Figure 5.10 Effect of the precrystallization time on the textural properties of ZS composites: (A) N_2 sorption isotherms and (B) the corresponding pore size distribution curves.

The N_2 adsorption/desorption isotherms and corresponding pore size distribution curves of ZS-xt-3.5p materials are illustrated in Figure 5.10. As expected, ZS-6t-3.5p, ZS-12t-3.5p and ZS-24t-3.5p exhibit type IV isotherms with a very steep capillary condensation step in the relative pressure (p/p_0) range of 0.7-0.9, characteristic for an ordered mesostructure with a large and uniform pore size. It should be noted that the isotherm of ZS-24t-3.5p shows a relatively steep increase of the adsorbed N_2 amount at low relative pressures ($p/p_0 < 0.01$), indicating the presence of micropores in this sample. The same phenomenon is observed from the isotherm of ZS-36t-3.5p, but more obvious, which further confirms its microporous nature. On the other hand, ZS-6t-3.5p and ZS-12t-3.5p show no indications of micropores from their isotherms. In relation with the XRD results, a good agreement can be found. Additionally, an increased gas uptake at relative high pressures ($p/p_0 > 0.9$) can be seen for all samples, indicative of inter-crystalline

pores. These observations are directly reflected by the pore size distribution as shown in Figure 5.10B. The first three samples have narrow pore size distribution curves centered at approximately 9.0 nm (ZS-6t-3.5p, ZS-12t-3.5p) and 7.5 nm (ZS-24t-3.5p), whereas the pore size distribution of ZS-36t-3.5p looks broader, suggesting that this sample contains only interparticle voids.

Table 5.3 Effect of the precrystallization time on the structural and textural properties of ZS composites. The data of Al-SBA-15 and H-ZSM-5 are included for reference.

Sample	d_{100} (nm)	a_0 (nm)	D_p (nm)	W (nm)	S_{meso}[c] (m^2/g)	S_{BET} (m^2/g)	V_{micro}[c] (cm^3/g)	V_t (cm^3/g)
ZS-6t-3.5p	11.2	12.9	9.1	3.8	372	372	0	0.97
ZS-12t-3.5p	11.3	13.0	9.0	4.0	346	346	0	0.98
ZS-24t-3.5p	11.2	12.9	7.5	5.4	233	361	0.058	0.84
ZS-36t-3.5p	-	-	-	-	103	324	0.113	0.27
Al-SBA-15[a]	10.2	11.7	7.2	4.5	466	466	0	0.93
H-ZSM-5[b]	-	-	-		110	373	0.113	0.21

[a]synthesized by the same procedure as ZS-xt-3.5p series, but using the conventional silica based source TEOS instead of zeolite seeds; [b]commercial Al-rich H-ZSM-5 (Zeocat PZ-2/25); [c]t-plot method; d_{100}: spacing value; a_0: unit cell parameter ($a_0 = 2 \times d_{100}/3^{1/2}$); D_p: pore diameter; W: pore wall thickness ($W = a_0 - D_p$); V_t: total pore volume; the missing parameters are due to the absence of an ordered mesostructure.

The detailed information about the textural properties of all ZS-xt-3.5p materials as well as the reference samples is summarized in Table 5.3. The specific BET surface area of ZS-xt-3.5p series lies in the range of 324-412 m^2/g, which represents a feature of both highly condensed mesoporous materials and microporous zeolites [80,107]. No micropore volumes (V_{micro}) of ZS-6t-3.5p and ZS-12t-3.5p can be derived by t-plot method, further confirming the absence or very small content of ZSM-5 domains in these samples. Extending the precrystallization time to 24 h and 36 h, the V_{micro} of the resulting composites rises drastically at the expense of the mesoporous phase (S_{meso}). As a consequence, the total pore volume decreases sharply, from 0.97-0.84 cm^3/g for the predominant mesoporous samples (ZS-6t-3.5p, ZS-12t-3.5p, ZS-24t-3.5p, Al-SBA-15) to 0.27-0.21 cm^3/g for the samples dominated by the ZSM-5 phase (ZS-36t-3.5p and H-ZSM-5).

5.3.2 Effect of the precrystallization time on the acidic properties

The total number and strength of acid sites of ZS-xt-3.5p composites and the reference materials H-ZSM-5 and Al-SBA-15 were determined by NH_3-TPD. The results are

presented in Figure 5.11 and Table 5.4 together with the elemental compositions. Similar to ZS-6t-yp series, all ZS-xt-3.5p samples exhibit a TPD profile with two desorption peaks. The dominant peak around 200 °C probably arises from desorbed NH_3 on weak acid sites, whereas the second broader peak, shaped like a tail, in the range of 300-500 °C shows the presence of medium and strong acid sites.

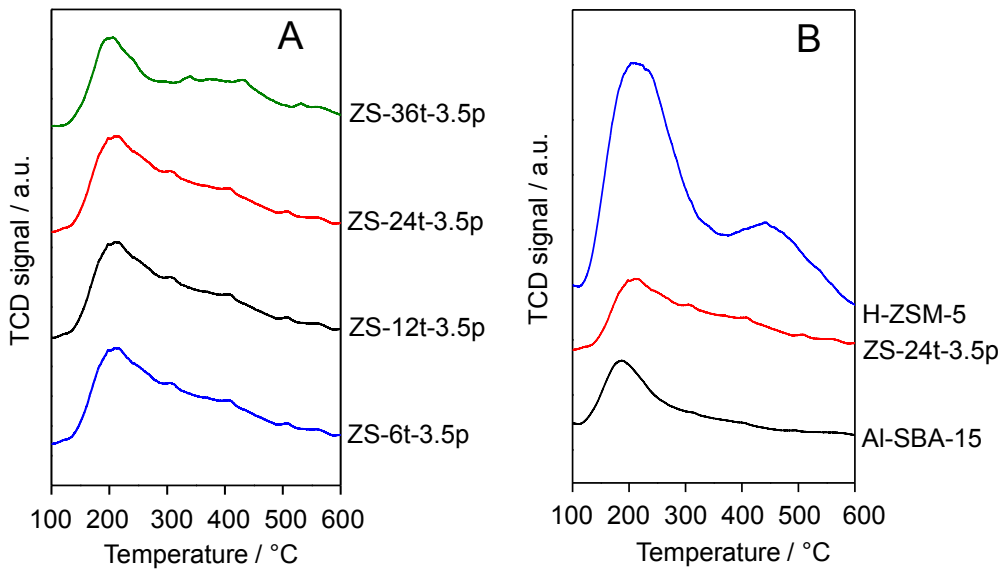

Figure 5.11 NH_3-TPD profiles of (A) ZS composites with various precrystallization times and (B) ZS-24t-3.5p with respect to the reference samples H-ZSM-5 and Al-SBA-15.

Table 5.4 Effect of the precrystallization time on the elemental composition and total acidity of ZS composites. The data of Al-SBA-15 and H-ZSM-5 are included for reference.

Sample	Si/Al in gel	Si/Al in products[c]	Total acidity (mmol NH_3/g)[d]
ZS-6t-3.5p	30	34	0.26
ZS-12t-3.5p	30	32	0.27
ZS-24t-3.5p	30	30	0.34
ZS-36t-3.5p	30	27	0.31
Al-SBA-15[a]	30	45	0.18
H-ZSM-5[b]	n.a.	11	1.24

[a]synthesized by the same procedure as ZS-xt-3.5p series, but using the conventional silica based source TEOS instead of zeolite seeds; [b]commercial Al-rich H-ZSM-5 (Zeocat PZ-2/25); [c]Si, Al content in the products analyzed by AAS and ICP, respectively; [d]NH_3-TPD.

From Table 5.4, it can be seen that extending the precrystallization time slightly increases both the total acidity and the incorporated Al content in the final products. This

can be explained by larger fractions of nano-ZSM-5 phase generated during the longer precrystallization time periods. The total acidity of ZS-24t-3.5p and ZS-36t-3.5p is noticeably higher than that of ZS-6t-3.5p and ZS-12t-3.5p, which reflects a sufficient amount of nano-ZSM-5 phase to be detected by XRD (see Figure 5.5 B). It is also noteworthy that the number of acid sites is lower for ZS-36t-3.5p than for ZS-24t-3.5p though the former contains predominantly nano-ZSM-5 domains. The possible explanation has been pointed out by Waller et al. [74] who observed that the interaction at the interface of microporous and mesoporous domains increased the number of hydroxyl groups, and consequently also the composite's total acidity.

With respect to commercial Al-rich H-ZSM-5, ZS composites have significantly lower acidity in terms of both number and strength of acid sites, but their acidic properties are higher than those of Al-SBA-15 prepared from conventional silica precursors (Figure 5.11 B and Table 5.4). The improved acidic properties of these ZS samples may result from the presence of nano-ZSM-5 and the retention of zeolite building units in SBA-15 analog phase [60-71]. Additionally, py-IR measurements were carried out over ZS composites and the reference samples in order to determine and discriminate the contribution of BS and LS.

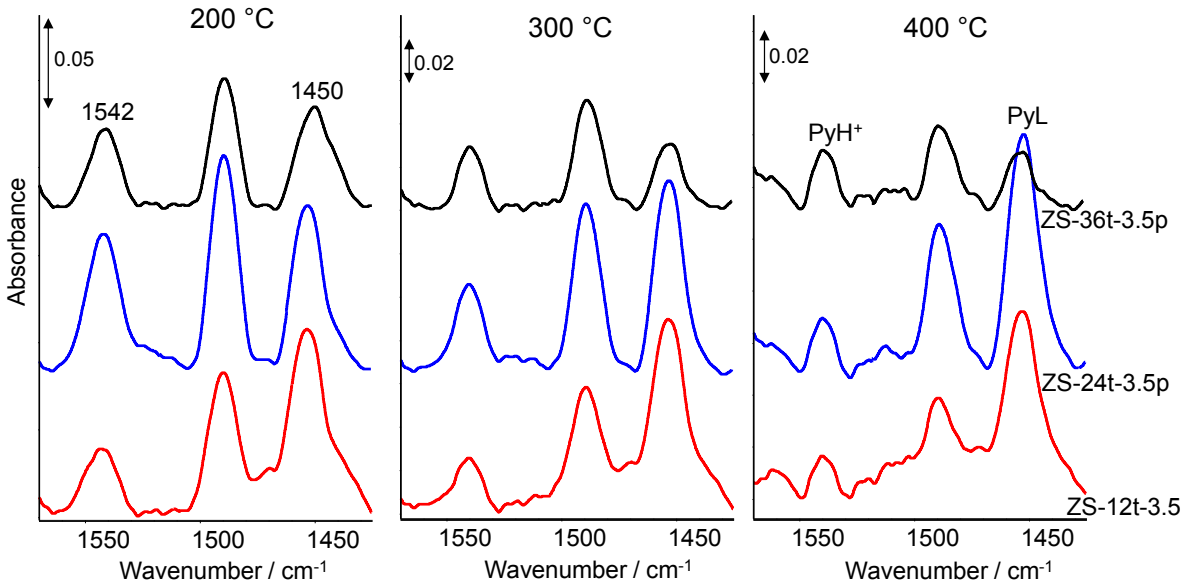

Figure 5.12 py-IR spectra of ZS-12t-3.5p, ZS-24t-3.5p and ZS-36t-3.5p after evacuation at 200, 300 and 400 °C.

Figure 5.12 presents the IR spectra of pyridine adsorbed on the surface of the representative ZS samples: ZS-12t-3.5p, ZS-24t-3.5p and ZS-36t-3.5p after adsorption

procedure and evacuation at 200, 300 and 400 °C. Quantitative estimation of BS and LS in the studied samples is given in Table 5.5. As expected, the density of BS in Al-SBA-15 is relatively low and largely reduced with desorption temperature, suggesting predominant weak BS. In contrast, ZS-36t-3.5p, dominated by nano-ZSM-5 domains, undergoes the least decrease upon evacuation at 400 °C, resulting in the highest concentration of pyridine adsorbed on BS compared to the other ZS composites. Therefore, this desorption temperature is taken as borderline with the assumption that weak and medium BS release pyridine while strong BS still retain it after evacuation at 400 °C. Clearly, the greater the content of nano-ZSM-5 phase, the greater the concentration of strong BS and the higher BS-to-LS ratio: H-ZSM-5 > ZS-36t-3.5p > ZS-24t-3.5p > ZSC-12t-3.5p (ZS-6t-3.5p) > Al-SBA-15. Both Al-SBA-15 and ZS samples possess high densities of strong LS. However, it is worth noting that the LS density is always relatively lower for ZS-36t-3.5p among the other samples, possibly because of almost complete absence of the mesoporous phase. Thus, the concentration of BS, in particular strong BS increases with increasing the zeolite phase whereas that of strong LS depends heavily on the mesoporous phase.

Table 5.5 Normalized integral intensities of pyridine adsorption bands over ZS composites upon evacuation at 200, 300 and 400 °C. The data of H-ZSM-5 and Al-SBA-15 are included for reference.

Samples	200 °C			300 °C			400 °C		
	B	L	B/L	B	L	B/L	B	L	B/L
ZS-12t-3.5p	1.79	3.79	0.47	0.95	3.09	0.30	0.49	2.66	0.18
ZS-24t-3.5p	3.02	3.68	0.82	1.39	3.55	0.39	0.66	3.52	0.19
ZS-36t-3.5p	2.10	3.02	0.69	1.14	1.42	0.80	0.80	1.02	0.78
Al-SBA-15[a]	1.58	2.21	0.71	0.92	1.97	0.46	0.30	1.88	0.16
H-ZSM-5[b]	14.77	5.92	2.5	12.03	4.36	2.7	8.47	3.08	2.7

[a]synthesized by the same procedure as ZS-xt-3.5p series, but using the conventional silica based source TEOS instead of zeolite seeds; [b]commercial Al-rich H-ZSM-5 (Zeocat PZ-2/25); B, L are the integral band intensities of pyridine adsorbed on BS (1542 cm^{-1}) and LS (1450 cm^{-1}) normalized to the BET surface areas respectively ($x10^{-3}$, a.u.).

It is known that strong BS are typical for zeolites with bridging hydroxyl groups (Si-OH-Al) originated from tetrahedral Al in the zeolite framework. The nature of strong LS is not clear, but generally LS are generated by partial extraction of Al framework, identified as octahedral Al. As a result, zeolites like H-ZSM-5 are often dominated by strong BS [107,108]. In contrast, most incorporated Al in amorphous mesoporous materials like Al-SBA-15 appears to contribute to LS acidity regardless of tetrahedral or octahedral Al due

to lack of a long-range atomic order [109]. Several strong BS can be also generated by the interaction of silanol groups with tetrahedral Al nearby [110]. Generally speaking, the acidic properties of amorphous mesoporous aluminosilicates are characterized by strong LS and weak BS [89,109]. Using zeolite nanoseeds as building blocks to construct a mesostructure proved to be an effective way to improve strong BS thanks to the retention of zeolite building units in the mesoporous walls [53]. Hence, the increased density of strong BS of ZS composites with respect to Al-SBA-15 might originate from the presence of nano-ZSM-5 phase as well as the preservation of zeolite building units in the mesoporous SBA-15 analogs phase. However, the larger densities of strong BS for ZS-24t-3.5p and ZS-36t-3.5p further emphasize the importance of additional nano-ZSM-5 phase when the aim is to enhance BS with improved accessibility. On the other hand, it is interesting to see that the contribution of BS and LS in the ZS composites can be tuned for different reactions by controlling the distribution of microporous and mesoporous phases via the precrystallization time.

5.4 Hydrothermal stability

Hydrothermal stability is of crucial importance as potential catalysts derived from the presented materials are targeted for the FCC process. This is because in the FCC process the catalyst has to withstand severe conditions, i.e. 700-800 °C in the presence of steam during regeneration step [43]. Therefore, the hydrothermal stability was evaluated by treatment of the representative sample ZS-24t-3.5p (800 °C, 30% of steam in He flow (30 ml/min)) and subsequent SAXS, XRD, and N_2 sorption analyses. The results for the fresh and steamed samples are shown in Figures 5.13 A (SAXS), B (XRD) and C (N_2 sorption).

Upon steaming for 24 h, ZS-24t-3.5p still exhibits three well-resolved reflections in the SAXS pattern assigned to the 100, 110, and 200 planes of highly ordered hexagonal symmetry, confirming the well-preserved ordered mesostructure (Figure 5.13 A). Similarly, in the wide-angle range, the XRD patterns of the untreated and treated samples (Figure 5.13 B) show almost identical reflections, typical of MFI topology and indicative of the excellent preservation of ZSM-5 nanocrystals. The high stability of ZS-24t-3.5p against steaming is finally assured by N_2 adsorption and desorption measurements (Figure 5.13C). Only little change can be observed in the shape of N_2 adsorption and desorption isotherms of ZS-24t-3.5p before and after the water vapor treatment, implying that its ordered mesostructure is well retained. Furthermore, the pore size and pore volume are almost unchanged at 7.5 nm and 0.84 cm^3/g, while by steaming under the same condition, the mesostructure of SBA-15 synthesized at 100 °C was partially collapsed already after 4

h, reducing the pore size from 6.4 to 4.6 nm and the pore volume from 1.06 to 0.43 cm^3/g, representing a loss of ca. 60% [111]. These data indicate that ZS-24t-3.5p possesses remarkable hydrothermal stability, which makes such ZS composites superior to other composites, synthesized at low temperature, whose pore size and volume experienced a pronounced decrease even after treatment at less severe conditions [52,71,77].

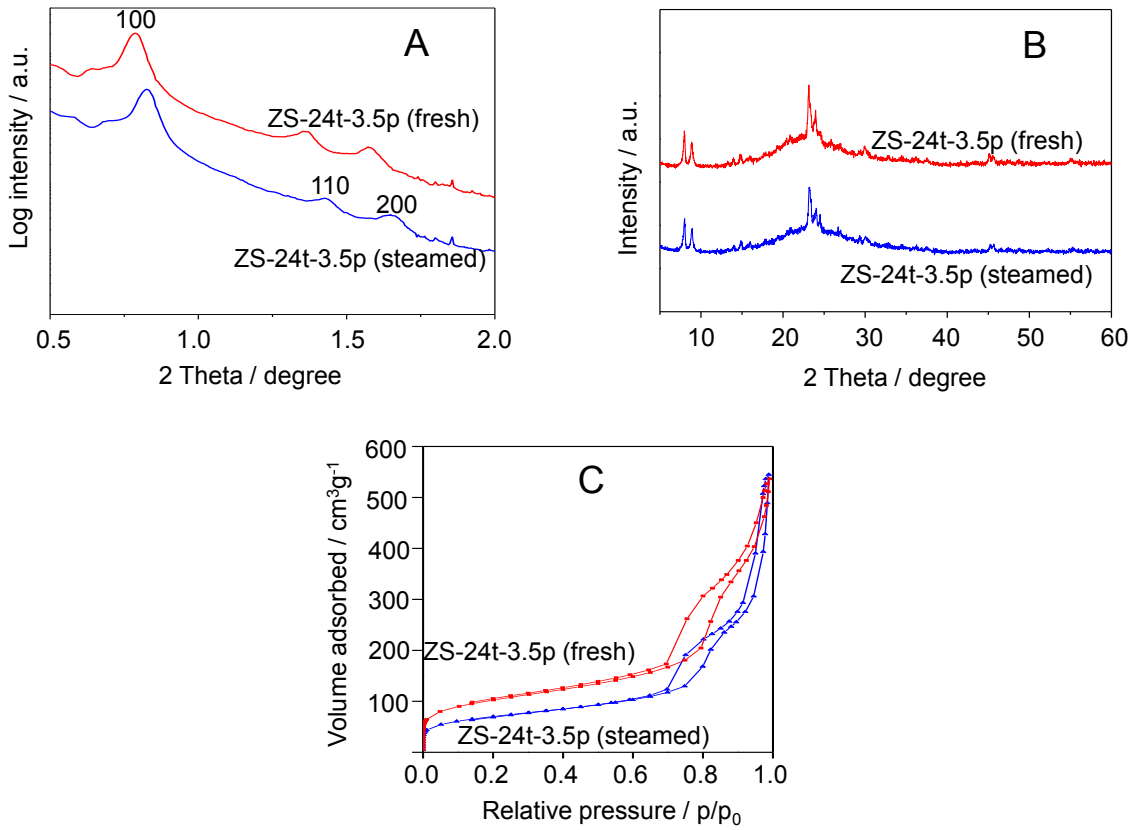

Figure 5.13 Effect of steaming of ZS-24t-3.5p at 800 °C for 24 h on the structural and textural properties: (A) SAXS, (B) XRD and (C) N_2 sorption isotherms.

The preservation of mesoporosity is of important significance since the modern FCC process tends to work with very short contact time (less than 2 s) [112], where the preservation of large pores eases mass transfer, finally improving catalytic performance. The high hydrothermal stability of nanocrystalline ZSM-5 phase is well-documented and results from the crystalline framework made up of SiO_4 and AlO_4 units. For the mesoporous phase in the composites, its remarkable hydrothermal stability might be related to the retention of zeolite building units and the high degree of silica condensation in the mesoporous walls as shown by IR and ^{29}Si-MAS-NMR analyses, respectively.

5.5 Catalytic cracking of cumene and TIPB

The catalytic activity of ZS composites compared to the reference samples Al-SBA-15 and H-ZSM-5 was investigated in the gas phase cracking of cumene and TIPB as probe reactions at 300 °C and ambient pressure. Similar to the previous tests in section 4.3, no thermal cracking was evidenced under the applied conditions, and with the presence of the ZS catalyst, cumene and TIPB were mainly dealkylated on BS to produce benzene and di-isopropylbenzene as the major products, respectively.

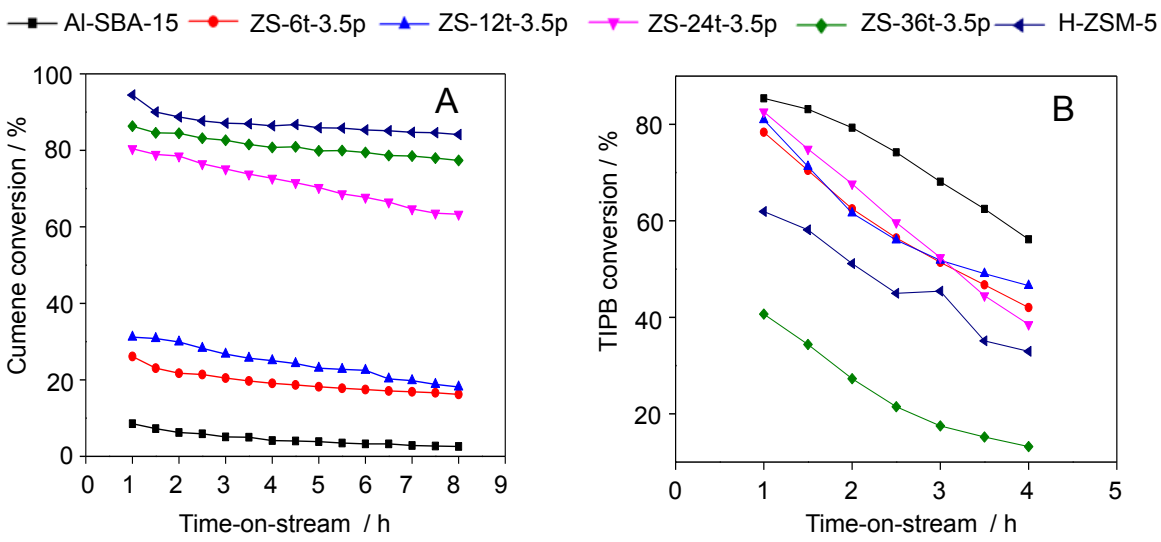

Figure 5.14 Conversion in the cracking of (A) cumene and (B) TIPB over ZS composites compared to Al-SBA-15 and H-ZSM-5 with time-on-stream. Reaction conditions: ambient pressure, 300 °C, WHSV = 1.5 h^{-1} (cumene) or 1.0 h^{-1} (TIPB).

The cracking activities over ZS composites in the gas phase cracking of cumene and TIPB with time-on-stream compared to Al-SBA-15 and H-ZSM-5 are depicted in Figure 5.14. The cumene and TIPB conversions after 1 h on-stream are summarized in Table 5.6. It is apparent that the cumene conversion heavily depends on strong BS. The conversion of cumene over ZS-36t-3.5p is higher than ZS-24t-3.5p though the latter sample contains a higher density of acid sites, in particular BS. This means that strong BS are active for cumene cracking rather than weak BS. For a better illustration, the relationship between the cumene conversion and density of strong BS is plotted in Figure 5.15. Obviously, the cumene conversion increases monotonously with the concentration of strong BS. Furthermore, by comparing with the cumene cracking behavior over the highly microporous materials (ZSM-5-P and MZ-xAAT) at 250 °C in section 4.3, the linear

relationship between the cumene conversion and strong BS of the ZS composites might indicate that there are no diffusional constraints affecting the cracking activity of ZS catalysts under the investigated conditions.

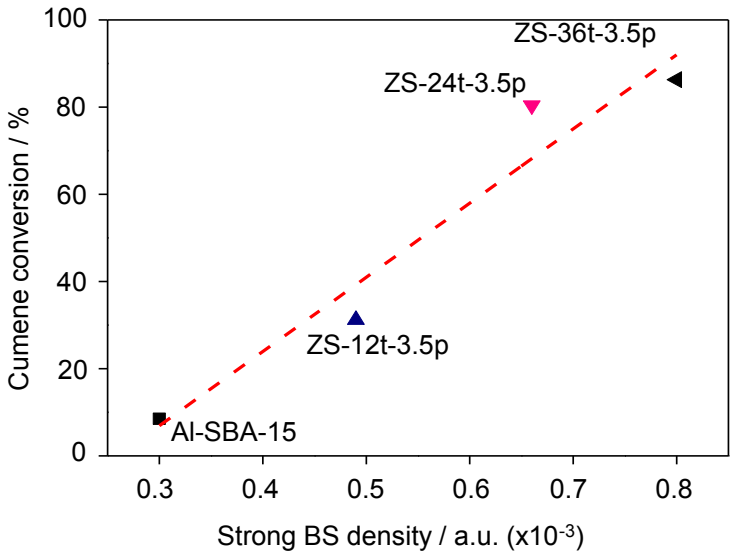

Figure 5.15 Relationship between the strong BS density and cumene conversion upon 1 h on-stream. Reaction conditions: ambient pressure, 300 °C, WHSV = 1.5 h^{-1}.

Table 5.6 Catalytic activities of ZS composites, Al-SBA-15 and H-ZSM-5 in the cracking of cumene and TIPB at 300 °C, WHSV = 1.5 h^{-1} (cumene) or 1 h^{-1} (TIPB) and ambient pressure.

Sample	Total acidity[c]	Strong BS[d]	Cumene conversion[e], %	TIPB conversion[e], %
ZS-6t-3.5p	0.26	n.a.	28.1	78.3
ZS-12t-3.5p	0.27	0.49	31.2	80.9
ZS-24t-3.5p	0.34	0.66	80.4	82.5
ZS-36t-3.5p	0.31	0.80	86.3	40.6
Al-SBA-15[a]	0.18	0.30	13.5	85.2
H-ZSM-5[b]	1.24	8.47	94.4	61.9

[a]synthesized by the same procedure as ZS-xt-3.5p series, but using the conventional silica based source TEOS instead of zeolite seeds; [b]commercial Al-rich H-ZSM-5 (Zeocat PZ-2/25); [c]NH_3-TPD (mmol NH_3/g); [d]strong BS are defined as the normalized integral band intensities of pyridine adsorbed on BS (1542 cm^{-1}) after evacuation at 400 °C (×10^{-3} a.u) respectively; [e]cumene and TIPB conversions after 1 h time-on-stream.

From Table 5.6, one can see that H-ZSM-5 exhibits the highest cumene conversion (94%) because of the very high concentration of strong BS. The samples ZS-24t-3.5p and ZS-36t-3.5p display approximately 80 and 86% cumene conversion, respectively, being comparable to that of H-ZSM-5. Considering the significant difference in the strong BS

density of these samples, these results again suggest that the presence of the mesoporous phase enhances the molecular transport to/from the active strong BS mostly located inside nano-ZSM-5 domains, thereby allowing high cumene conversion over these ZS samples despite their much lower densities of strong BS. Similar observations have been reported by Waller et al. [74] and others [73,100]. The authors found that the dispersion of nano-zeolites in a mesoporous matrix offered the high accessibility to almost all zeolite domains whereas nano-zeolites forming aggregates like in case of H-ZSM-5 reduced the accessibility to zeolite domains buried inside the aggregates. The samples ZS-6t-3.5p and ZS-12t-3.5p with the predominant mesoporous features show a moderate cumene conversion of around 30%, which further supports the work of Frunz et al. [73]. They found that the high intrinsic cumene cracking activity of zeolites cannot be attained with X-ray amorphous zeolite precursors incorporated in the mesoporous walls. However, it should be noted that ZS-6t-3.5p and ZS-12t-3.5p are still far more active than Al-SBA-15 (13% cumene conversion). The poor activity of Al-SBA-15 might be due to the least strong BS caused by its amorphous nature. The absence of any reasonable relationships between the cumene cracking activity and LS acidity further confirms the crucial role of strong BS in the cracking of cumene under the investigated conditions.

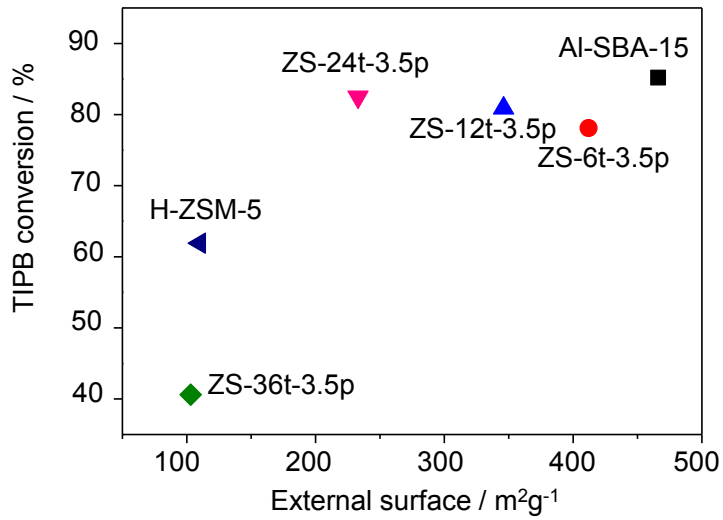

Figure 5.16 Relationship between the TIPB conversion and external surface upon 1 h on-stream. Reaction conditions: ambient pressure, 300 °C, WHSV = 1 h^{-1}.

In contrast to the cracking of cumene that serves to evaluate strong BS mainly located inside the micropores, the cracking of TIPB allow testing the catalytic activity of the external (mesoporous) surface since TIPB cannot enter the micropores of ZSM-5 domains. It is clear that there are no reasonable relationships between the TIPB

conversion and acidity (Table 5.6), but a good correlation between the TIPB conversion and external surface can be observed (Figure 5.16). Indeed, Al-SBA-15 possessing the largest external surface is the most active catalyst in the cracking of TIPB despite its lowest cumene conversion. The reason is that TIPB can be easily converted by even weak BS and it has the free accessibility of active sites inside the mesopores. Compared to Al-SBA-15, the ZS composites with the relatively large external surface provided by detectable mesoporous SBA-15 analog phase (ZS-6t-3.5p, ZS-12t-3.5p and ZS-24t-3.5p) exhibit slightly lower TIPB conversions of approximately 80%. This is because the TIPB cracking over the ZSM-5 phase proved to occur solely on the external surface with less active sites [107]. However, it appears that the TIPB conversion over ZS-24t-3.5p is higher than ZS-6t-3.5p and ZS-12t-3.5p though the differences are not pronounced. This might be due to the interaction at the surface interface of microporous and mesoporous phases, giving rise to an increase of accessible acid sites [74], as discussed above. Nevertheless, ZS-36t-3.5p containing hardly any mesoporous SBA-15 analog phase and the smallest external surface, still affords approximately 40% TIPB conversion, suggesting that the nano-ZSM-5 domains of this sample are quite effective for conversion of bulky molecules like TIPB. Similarly, H-ZSM-5, having the very high density of BS and consisting of small crystals (ca. 250 nm as verified by SEM and TEM images in chapter 4), displays a fairly high TIPB conversion of 61.9% after 1 h on-stream. Interestingly, the sample ZS-24t-3.5p shows high activities in the cracking of both cumene and TIPB, reaching 80 and 82% conversion, respectively. Thus, by controlling the distribution of microporous and mesoporous phases, the advantages of ZSM-5 nanocrystals and SBA-15 analogs can be combined to create superior materials for cracking reactions.

5.6 Summary and conclusions

Hierarchically structured composites that consist of mesoporous and microporous domains with easily tuneable phase content have successfully developed from preformed ZSM-5 precursors by high temperature synthesis. It was found that the pH adjustment prior to hydrothermal treatment at elevated temperature determines the formation of ordered mesostructures with increased silica condensation and aluminum incorporation, whereas the precrystallization time of initially formed ZSM-5 precursors controls the distribution of nano-ZSM-5 phase and SBA-15 analog phase. Starting from zeolite seeds with shorter aging time periods (6 and 12 h), ordered mesoporous SBA-15 type materials are mainly obtained (ZS-6t-3.5p and ZS-12t-3.5p). On the other hand, the longer precrystallization time (36 h) leads to predominant ZSM-5 nanocrystals (ZS-36t-3.5p). Most notably, the hierarchically structured composite (ZS-24t-3.5p), in which spherical

ZSM-5 nanocrystals (40-50 nm in diameters) are blended homogeneously with well-ordered, highly condensed mesoporous SBA-15 analogs can be prepared from the ZSM-5 precursor solution that has been precrystallized for 24 h. The acidic properties, in particular the surface density of strong Brønsted acid sites of the ZS composites are significantly augmented, being comparable to those of nano-ZSM-5. The bimodal micro-/mesoporous structures are well-preserved even upon steaming at 800 °C for 24 h, confirming the remarkable hydrothermal stability of the ZS composite. The gas phase cracking of cumene and TIPB as probe reactions reveals that an increased density of BS with high accessibility has been achieved over the ZS composite, giving high conversions of both cumene and TIPB.

Chapter 6

Catalytic Performance of Hierarchical Catalysts in the Cracking of Triglyceride-rich Biomass

Chapter 6 evaluates the performance of the prepared hierarchical ZSM-5 catalysts compared to commercial ZSM-5 (ZSM-5-P) and industrial FCC catalyst (Midas-BSR) in the catalytic cracking of triglyceride-rich biomass, i.e. triolein and WCO, under FCC conditions. The influence of operation variables, catalyst characteristics and feedstock compositions is systematically studied to establish the structure, property and catalytic performance relasionships. The advantages of the hierarchical catalysts over the commercial ZSM-5 and FCC catalyst are evidenced in the form of enhanced activity and selectivity toward the desired products, i.e. gasoline and light olefins. A reaction pathway has been proposed based on the obtained catalytic data.

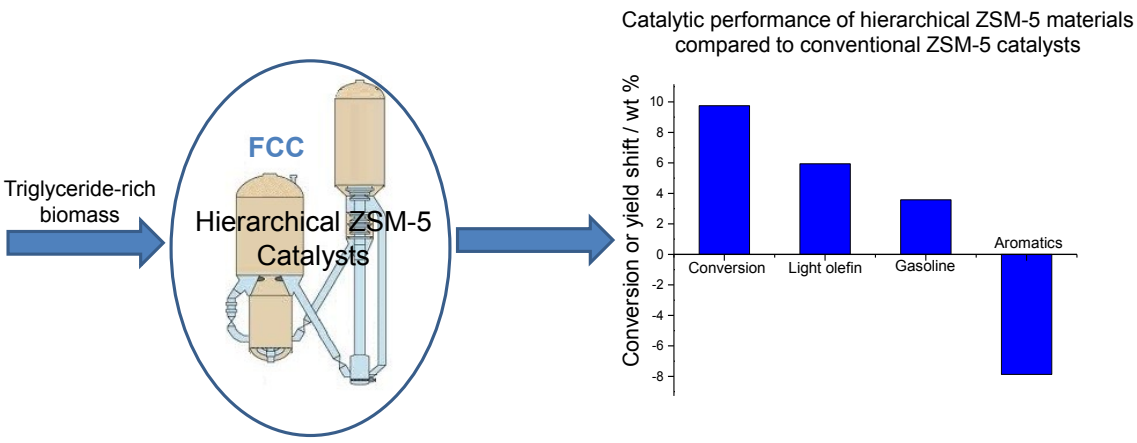

6.1 Feedstock and catalysts

6.1.1 Feedstock

Technical grade triolein and WCO with different unsaturation degrees were selected as the representative feedstock of triglyceride-rich biomass. This allows evaluating the effect of feedstock compositions on the catalytic performance. In addition, WCO has been emerging as one of the most economic raw materials for the production of biofuels and chemicals. The fatty acid and elemental compositions (Table 6.1) are similar to those of typical vegetable oils (see Table 1.1).

Table 6.1 Fatty acid and elemental compositions of technical grade triolein and WCO.

Feedstock	Triolein	WCO
Fatty acid composition as wt% methyl esters		
Dodecanoic acid [C12:0]	-	1.2
Palmitic acid [C16:0]	1.1	37.2
Stearic acid [C18:0]	1.9	4.9
Oleic acid [C18:1]	75.6	48.8
Linoleic acid [C18:2]	21.4	7.9
Elemental composition, wt%		
Carbon	79.4	79.4
Hydrogen	12.0	12.6
Oxygen	8.6	7.8
Nitrogen	0	0.2

[Cx:y] where x is the number of carbon atoms and y is the number of double bonds.

6.1.2 Catalysts

The main target of this chapter is to assess the catalytic performance of the prepared hierarchical ZSM-5 catalysts in the cracking of triglyceride-rich biomass under FCC conditions. Therefore, the optimal samples MZ-0.5AAT and ZS-24t-3.5p (with regard to improved mass transfer and preserved intrinsic zeolite characteristics) were selected as the representatives of mesoporous ZSM-5 materials and nano-ZSM-5/SBA-15 composites, respectively. For comparison, commercial Al-rich ZSM-5 (ZSM-5-P) and an industrial FCC catalyst (Midas-BSR) were used. The physicochemical properties of the industrial FCC catalyst (Grace Davison Refining Technologies) are listed in Table 6.2.

Table 6.2 Physico-chemical properties of the fresh industrial FCC catalyst (Midas-BSR).

Chemical composition (wt%)		Physical properties	
Al_2O_3	44.17	BET area, m^2/g	217
SiO_2	52.91	Pore volume, cm^3/g	0.18
Re_2O_3	1.84	Unit cell, nm	2.459

6.2 Thermal cracking

Thermal cracking may provide the basis on which the contribution of catalytic properties can be assessed. In general, the effect of thermal cracking becomes significant at elevated temperatures (> 460 °C) when using a fixed bed reactor with long residence time [113]. Therefore, the thermal cracking of triolein and WCO was carried out at 550 °C over glass beads (inert material). The results are summarized in Table 6.3.

Table 6.3 Thermal cracking of triolein and WCO at 550 °C.

Feedstock	Triolein	WCO	Gas composition (wt%)[b]	Triolein	WCO
Conversion (wt%)[a]	24.7	26.4	Hydrogen	0.44	0.44
			Methane	3.09	3.08
Product yields (wt%)[a]			Ethane	5.03	5.02
Total gas	6.5	7.9	Ethene	11.38	11.37
Dry gas	1.3	1.6	Propane	4.58	4.57
LPG	1.7	2.1	Propene	9.33	9.32
Light olefins (C_2-C_4)	1.9	2.3	i-Butane	0.02	0.02
CO,CO_2	3.5	4.2	n-Butane	4.21	4.20
C_{5+}gasoline	17.0	17.3	t-2-Butene	0.45	0.45
LCO	29.6	29.0	1-Butene	7.24	7.23
HCO	45.7	44.6	i-Butene	0.19	0.19
Coke	0.1	0.1	c-2-Butene	0.30	0.30
Water	1.1	1.2	CO_2	34.84	34.81
Mass balance (wt%)[a]	98.2	96.7	CO	18.97	18.95

[a]wt% on a feed basis; [b]wt% on a gas product basis.

It is evident that the thermal degradation of triglycerides took place considerably at 550 °C, giving 24.7 wt% and 26.4 wt% conversion of triolein and WCO, respectively. However, the yield of HCO is high, suggesting that most of heavy oxygenated compounds formed by the decomposition of triglycerides have not converted thermally, which is in line with the earlier reports [19,34]. Dupain et al. [19] studied the thermal cracking of rapeseed oil in a micro-riser reactor with adjustable reaction time. The results showed that 72 wt% of

triglycerides were already converted to fatty acids at 525 °C within 50 ms. After approximately 5.8 s, nearly complete conversion of triglycerides was achieved whereas the consecutive conversion of fatty acids remained relatively low, which gave a high yield (approximately 60 wt%) of heavy oxygenated compounds (mainly fatty acids).

From Table 6.3, a similar product distribution has been obtained with triolein and WCO. The gas compositions appear to be almost identical, in which CO, CO_2 and light olefins, in particular ethene, are predominant. This indicates that decarbonylation and decarboxylation reactions as well as secondary cracking reactions, involving the elimination of ethylene from hydrocarbons, occur preferentially, being consistent with the previous works [22,114]. However, the low yield of gaseous products accompanied by the large fraction of unconverted fatty acids evidences the poor selectivity of thermal cracking of triglycerides toward valuable fuel compounds. On the other hand, the effect of thermal cracking should be taken into account when evaluating the catalytic performance at high temperature since it might open a parallel degradation route.

6.3 Catalytic cracking of triolein

It has been reported that the performance of a cracking catalyst primarily depends on operation conditions and feedstock compositions, i.e. unsaturation degree of triglycerides [15,19]. Therefore, the cracking of triolein comprising predominantly unsaturated triglycerides was first performed with the hierarchical catalysts to optimize the reaction conditions and to study the catalytic behavior. Then the catalytic performance of the hierarchical catalysts compared to the reference catalysts was evaluated in the cracking of real feedstock WCO containing less unsaturated triglycerides. By comparing the catalytic performance obtained with WCO and triolein at the optimized conditions, the effect of unsaturation level of feedstock can be inferred.

6.3.1 Catalytic performance of mesoporous ZSM-5 materials

The catalytic performance of mesoporous ZSM-5 (MZ-0.5AAT) in the catalytic cracking of triolein was studied at different catalyst-to-oil (CTO) mass ratios and reaction temperatures in order to find out the optimal reaction conditions for maximizing the production of gasoline range hydrocarbons and light olefins. The catalytic performance of commercial parent ZSM-5 (ZSM-5-P) was included for reference. This offers an opportunity to evaluate the effect of the changes in the acidic and textural properties on the catalytic performance since both catalysts have the same MFI topology (ZSM-5) and the post-synthesis modification mainly affects these mentioned properties (Chapter 4).

Table 6.4 shows the overall data in the cracking of triolein over mesoporous MZ-0.5AAT and its parent ZSM-5 at the different temperatures ranging from 400 to 550 °C. As expected, MZ-0.5AAT displays superior catalytic activity and yield toward the desired products compared to ZSM-5-P, especially in the low reaction temperature region where the diffusion rate seems to be the rate determining step [97,98].

Table 6.4 Effect of reaction temperatures on the conversion and product distribution in the catalytic cracking of triolein over ZSM-5-P and MZ-0.5AAT at a CTO ratio of 0.4 (g/g).

Sample	**ZSM-5-P**				**MZ-0.5AAT**			
Reaction temp. (°C)	**400**	**450**	**500**	**550**	**400**	**450**	**500**	**550**
Conversion (wt%)	61.3	77.5	89.0	88.7	69.0	84.6	88.2	89.7
Product yields (wt%)								
Total gas	16.2	28.4	38.0	43.3	19.7	30.7	37.6	43.7
Dry gas	1.3	2.6	5.0	7.7	1.4	2.7	4.9	7.6
LPG	12.7	22.7	28.6	30.5	16.0	24.9	28.5	30.8
Light olefins (C_2-C_4)	11.7	21.6	24.5	26.2	15.4	24.2	26.0	28.1
CO,CO_2	2.2	3.1	4.3	5.0	2.3	3.1	4.1	5.3
C_{5+}gasoline	35.6	40.7	40.9	37.1	37.9	42.7	41.7	38.1
LCO	17.6	13.3	7.3	6.7	16.0	9.6	7.9	7.4
HCO	21.1	9.2	3.7	4.6	15.0	5.8	3.9	2.9
Coke	2.5	1.5	1.2	1.2	3.4	2.2	1.7	1.4
Water	6.7	6.8	8.7	6.9	7.8	8.7	7.1	6.3
Mass balance (wt%)	95.2	98.4	97.5	97.6	96.7	98.4	97.5	97.6

wt% on a feed basis

By increasing the reaction temperature from 400 to 450 °C, the conversion over ZSM-5-P rises from 61.3 to 77.5 wt%, a relative increase of 26.4%, whereas MZ-0.5AAT gives a higher conversion of 69.0 to 84.6 wt%, corresponding to an increase of 22.6%. At the higher reaction temperature region (500-550 °C), however, no significant differences in the conversion can be seen. Both catalysts yield a comparable high conversion of approximately 88-90 wt% (Table 6.4 and Figure 6.1 A). A similar behavior was observed by Al-Khattaf et al. [97,98], who performed the cracking of TIPB over zeolite Y in a riser simulator. They postulated that the reaction temperature increase shifts the catalytic cracking of TIPB from the diffusion-controlled regime to the reaction kinetics-controlled regime. At the lower reaction temperature (400-450 °C), the diffusional constraints limit the overall reaction rate, decreasing the catalyst effectiveness [98]. In this case, the external surface enlargement induced by mesoporosity enhances the utilization of the zeolite's acid sites; therefore, the higher conversion over MZ-0.5AAT compared to ZSM-5-

P has been achieved. On the other hand, at 500-550 °C, the overall reaction rate seems to be determined by the intrinsic kinetics; hence, the comparable high conversions over both catalysts imply that the intrinsic zeolite characteristics of parent ZSM-5 have been preserved in mesoporous MZ-0.5AAT.

The reaction temperature has great influence on the production of light olefins and gasoline hydrocarbons. While the light olefin yield grows monotonously with the reaction temperature, the yield of gasoline goes through a maximum (Table 6.4). The increased formation of light olefins with the reaction temperature is well-acknowledged because it involves a highly endothermic thermal cracking process [25,115]. Interestingly, mesoporous MZ-0.5AAT always produces approximately 3 wt% higher yield of light olefins than its parent ZSM-5-P, irrespective of the reaction temperature. The superior yield of light olefins over MZ-0.5AAT may originate from the increased conversion and/or light olefin selectivity. Considering the large FCC capacity in refineries, such increases are definitely of economical relevance. To elucidate this, the selectivity toward light olefins with respect to other gaseous hydrocarbons, more common known as light olefinicity, defined as the fraction of C_2-C_4 olefins per the total C_2-C_4 hydrocarbons is plotted as a function of the conversion (Figure 6.1B).

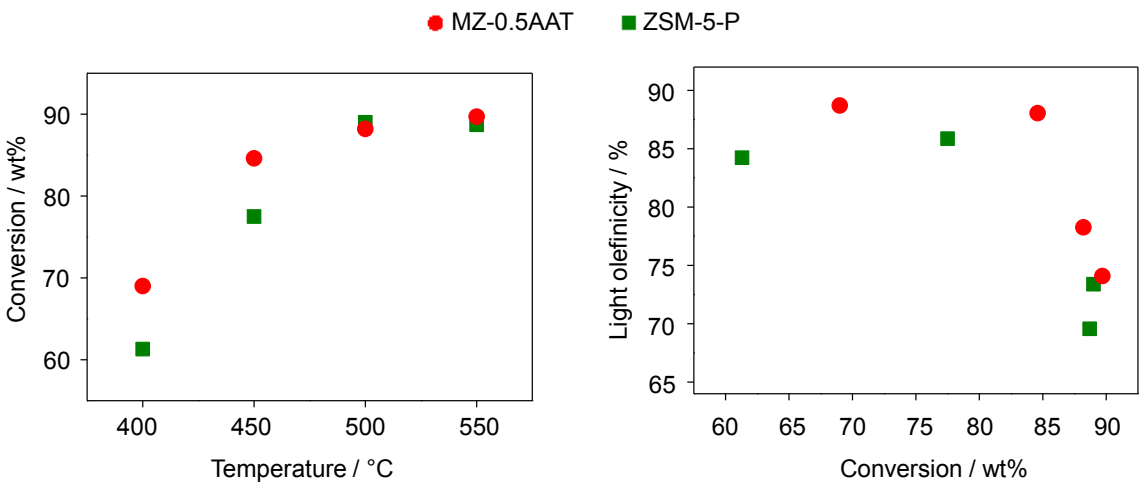

Figure 6.1 Effect of reaction temperature on the conversion (A) and light olefinicity (B) at a CTO ratio of 0.4 g/g.

Clearly, a higher selectivity toward light olefins over MZ-0.5AAT than with parent ZSM-5-P is evidenced. These results suggest that the undesired secondary reactions of the primary light olefins have been partially suppressed over MZ-0.5AAT, being consistent with the work of Botas et al. [37] who performed the cracking of rapeseed oil over

hierarchical ZSM-5 catalysts using a fixed bed reactor with much longer contact time (WHSV = 7.6 h^{-1}). They postulated that the presence of mesoporosity caused shorter residence times inside the zeolite micropores (by shortening the diffusion path length), therefore, avoiding further transformation of the primary light olefins.

Concerning the observed gasoline yield variation, the plausible explanation is that gasoline is an unstable cracking product. It can be produced by cracking of heavier fractions such as HCO and LCO, but at the same time gasoline can be cracked to gaseous products like LPG if the severity of cracking process is adequate [18,36,115]. In this case, the reduced gasoline yield at 500-550 °C confirms the occurrence of the over-cracking reactions (Table 6.4). Thus, the reaction temperature should not go above 450 °C when the gasoline range hydrocarbons are desirable. On the other hand, it is also worth noting that MZ-0.5AAT produces more gasoline than ZSM-5-P, particularly in the low temperature range of 400-450 °C, suggesting that mesoporous MZ-0.5AAT has a higher selectivity toward gasoline hydrocarbons in general.

Table 6.5 Effect of CTO ratios on the conversion and product distribution in the catalytic cracking of triolein over ZSM-5-P and MZ-0.5ATT at 450 °C.

Sample	**ZSM-5-P**				**MZ-0.5AAT**			
CTO ratio (g/g)	**0.2**	**0.4**	**0.8**	**1.2**	**0.2**	**0.4**	**0.8**	**1.2**
Conversion (wt%)	48.5	77.5	85.8	85.7	54.5	84.6	85.3	84.9
Product yields (wt%)								
Total gas	13.0	28.4	32.6	31.3	14.8	30.7	31.0	32.0
Dry gas	1.0	2.6	3.1	2.9	1.0	2.7	3.1	3.0
LPG	9.3	22.7	26.6	25.6	10.6	24.9	25.3	26.5
Light olefins (C_2-C_4)	9.4	21.6	18.6	13.2	10.9	24.2	18.5	12.9
CO,CO_2	2.7	3.1	2.8	2.7	3.1	3.1	2.6	2.5
C_{5+}gasoline	30.9	40.7	42.1	42.6	33.6	42.7	42.3	39.8
LCO	19.7	13.3	9.5	9.6	17.3	9.6	9.4	9.5
HCO	31.8	9.2	4.8	4.7	28.0	5.8	5.3	5.6
Coke	0.9	1.5	2.1	2.6	1.2	2.2	3.5	4.2
Water	3.6	6.8	8.8	8.9	4.8	8.7	8.2	8.6
Mass balance (wt%)	97.1	98.4	95.4	95.5	97.0	99.8	99.0	98.0

wt% on a feed basis

The effect of a varying CTO ratio on the conversion and product distribution at 450 °C are shown in Table 6.5 and Figure 6.2. With the CTO ratio increase from 0.2 to 0.4 (g/g), the conversion over ZSM-5-P enhances from 48.5 to 77.5 wt%, while the yields of gasoline and light olefins rise from 30.9 and 9.4 wt% to 40.7 and 21.6 wt%, respectively.

For MZ-0.5AAT, a similar trend has been observed in the CTO ratio ranging from 0.2 to 0.4 (g/g), but approximately 7 wt% higher conversion and 2-3 wt% higher yields of gasoline and light olefins than those of ZSM-5-P have been attained. These findings further confirm the advantages of MZ-0.5AAT over ZSM-5-P under the diffusion-controlled reaction regime.

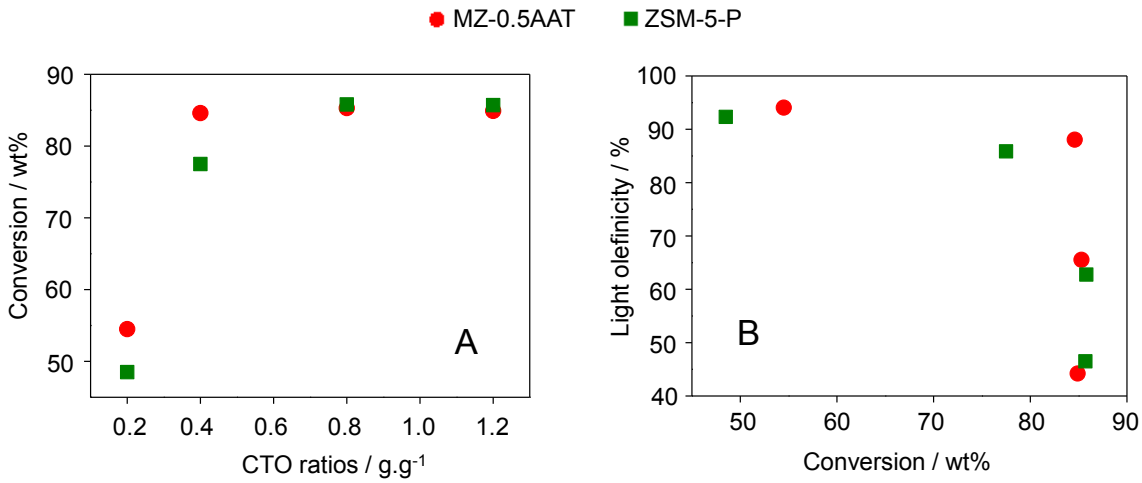

Figure 6.2 Effect of CTO ratios on the conversion (A) and light olefinicity (B) at 450 °C.

As the CTO ratio goes above 0.4, however, both catalysts yield almost constant conversions, but lower light olefin fractions. It should be noted that the reduction in the fraction of light olefins has been compensated by the increase in the light paraffin fraction (Table B.3), which gives rise to a little change in the conversion, gasoline yield, and total gas yields (Table 6.5). These results indicate that hydrogen transfer reactions take place drastically when more active acid sites are involved in the reaction system at higher CTO ratios [43,116]. Thus, in order to maximize the production of gasoline and light olefins, the CTO ratio of 0.4 (g/g) is considered as optimal.

6.3.2 Catalytic performance of nano-ZSM-5/SBA-15 analogs

Table 6.6 gives the overall catalytic performance of ZS-24t-3.5p in the catalytic cracking of triolein as a function of the reaction temperature and CTO ratio. There are dramatic changes in the triolein conversion and product distribution due to the changes in the operation variables. However, the selectivity toward light olefins (light olefinicity) is exceptionally high, independent of operation conditions, suggesting that ZS-24t-3.5p is a highly selective catalyst for converting triglycerides into light olefins.

Table 6.6 Effect of reaction temperatures and CTO ratios on the conversion and product distribution in the catalytic cracking of triolein over ZS-24t-3.5p.

CTO ratio (g/g) or	CTO ratio = 0.4 g/g			T = 550 °C		
reaction temperature (°C)	450	500	550	0.2	0.8	1.2
Conversion (wt%)	24.8	49.7	70.9	62.5	77.5	79.6
Product yields (wt%)						
Total gas	6.4	20.1	28.0	21.0	38.9	41.0
Dry gas	0.4	1.4	2.3	2.1	3.0	4.0
LPG	2.5	14.3	18.0	13.1	28.9	33.0
Light olefins (C_2-C_4)	2.3	14.0	18.2	13.5	29.4	33.5
CO,CO_2	3.5	4.4	7.6	5.8	7.1	4.1
C_{5+}gasoline	14.0	24.3	35.2	34.9	29.7	28.8
LCO	24.9	19.3	18.7	22.4	14.4	12.1
HCO	50.2	30.9	10.4	15.1	8.1	8.3
Coke	2.1	1.7	1.6	1.0	2.4	2.3
Water	2.3	3.6	6.1	5.6	6.5	7.5
Mass balance (wt%)	97.5	96.4	98.1	97.9	97.4	99.3
Light olefinicity (C_2-C_4), %	86.0	90.7	91.7	90.9	93.6	92.0

wt% on a feed basis

As can be seen from Table 6.6, the reaction temperature increase from 450 to 550 °C steadily enhances the conversion and light olefin yield from 24.8 and 2.3 wt% to 70.9 and 18.2 wt% respectively. This corresponds to increases by approximately 200 and 700% for the conversion and light olefins yields, respectively. However, these absolute values remain noticeably lower compared to those of mesoporous ZSM-5 materials (MZ-0.5AAT) at the same cracking conditions (Table 6.4), suggesting that ZS-24t-3.5p composite is less active. It is expected because ZS-24t-3.5p has a much lower density of acid sites than MZ-0.5AAT. Similarly, a progressive growth in the gasoline yield with the reaction temperature has been observed, from 14.0 wt% at 450 °C to 35.2 wt% at 550 °C, indicating that the cracking of heavy fractions to lighter products has dominated over ZS-24t-3.5p throughout the investigated temperature range. However, the reaction temperature should not go above 550 °C because thermal cracking may accelerate dramatically, which has negative effect on the desired product selectivity.

The effect of CTO ratio variations at 550 °C on the conversion and product distribution is also given in Table 6.6. As varying the CTO ratio from 0.2 to 1.2 g/g, the conversion and light olefin yield increase monotonously from 65.2 and 13.5 wt% to 79.6 and 33.5 wt%, respectively. These observations are different from those obtained with mesoporous MZ-

0.5AAT in the high range of CTO ratios (0.8-1.2 g/g) (Table 6.5). One possible explanation could be the difference in the acid site density and reaction temperature. It is known that hydrogen transfer reactions involving bimolecular reactions via carbenium ions should be accelerated with the density of strong BS [43,119]. Additionally, the relative rate of cracking reactions is more enhanced by the reaction temperature than that of hydrogen transfer reactions due to the higher activation energy of the former [19]. Thus, at the mild reaction temperature (450 °C) and high CTO ratios (0.8-1.2 g/g), MZ-0.5AAT with a higher density of BS facilitates hydrogen transfer reactions of light olefins while the conversion reaches almost constant values. On the other hand, at the same range of CTO ratios, but higher reaction temperature (550 °C), ZS-24t-3.5p with a much lower density of BS promotes cracking reactions to a larger extent with respect to hydrogen transfer reactions; therefore, the conversion and yield of light olefins are enhanced.

Unlike the conversion and light olefin production, the gasoline yield apparently goes through a maximum when varying the CTO ratios at 550 °C (Table 6.6). In fact, the gasoline yield shows a little gain from 34.9 to 35.2 wt% with the CTO ratio rise from 0.2 to 0.4 g/g and then drops sharply to 29.7 and 28.8 wt% at the CTO ratios of 0.8 and 1.2 g/g, respectively. This implies that the over-cracking of gasoline hydrocarbons has been promoted as the CTO ratio goes above 0.4 (g/g), giving rise to the substantial reduction in gasoline yield, but the boost in light olefins. Hence, the CTO ratio should not be higher than 0.4 g/g when the production of both gasoline and light olefins are targeted.

6.4 Catalytic cracking of WCO

The catalytic performance of the hierarchical ZSM-5 catalysts (MZ-0.5AAT, ZS-24t-3.5p) compared to commercial parent ZSM-5 (ZSM-5-P) and industrial FCC catalyst (Midas-BSR) was evaluated in the catalytic cracking of real feedstock WCO under the mild and severe cracking conditions. In the mild cracking operation, the cracking variables (450 °C and CTO ratio = 0.4 g/g) optimized for mesoporous MZ-0.5AAT material were used. The optimal conditions for ZS-24t-3.5p composite (550 °C, CTO ratio = 0.4 g/g) were applied in the severe cracking operation.

6.4.1 Catalytic performance of various catalysts under mild cracking conditions

Table 6.7 shows the overall data on the catalytic performance over the different catalysts which evidence that MZ-0.5AAT is the best catalyst for conversion of triglycerides into gasoline range hydrocarbons and light olefins under the mild cracking conditions.

Table 6.7 Catalytic performance of various catalysts in the catalytic cracking of WCO under the mild reaction conditions (450 °C, CTO ratio = 0.4 (g/g)).

Catalysts	Midas-BSR	ZS-24t-3.5p	ZSM-5-P	MZ-0.5AAT
Conversion (wt%)	23.8	26.8	74.3	84.1
Product yields (wt%)				
Total gas	4.0	6.9	28.6	33.5
Dry gas	0.3	0.4	2.4	2.4
LPG	2.1	3.1	21.6	26.5
Light olefins (C_2-C_4)	1.1	3.0	20.0	25.9
CO,CO_2	1.7	3.4	4.6	4.6
C_{5+}gasoline	15.2	16.4	36.4	40.0
LCO	17.9	22.9	15.1	9.40
HCO	58.3	50.2	10.5	6.50
Coke	2.2	1.5	2.5	2.55
Water	2.4	2.1	6.8	8.04
Mass balance (wt%)	98.1	96.7	98.2	96.9
Light olefinicity, %	49.4	87.7	83.8	89.9

wt% on a feed basis

As shown in Table 6.7, the industrial FCC catalyst Midas-BSR and composite ZS-24t-3.5p exhibit poor conversions of approximately 24-26 wt%. It can be explained by the fact that Midas-BSR and ZS-24t-3.5p are mixtures of active zeolite phase (< 50 wt% for the industrial sample) with other less active components such as silica-alumina or mesoporous aluminosilicates serving as supports, which reduce the densities of strong BS and consequently the catalytic activities [25,117]. On the contrary, ZSM-5-P and MZ-0.5AAT, which contain mainly ZSM-5 phase with much higher densities of strong BS, are far more active, giving double conversions compared to those of the first two samples. Remarkably, the conversion over MZ-0.5AAT (84.1 wt%) is considerably higher than over ZSM-5-P (74.3 wt%) though the former has a lower BS density. This again confirms that the presence of mesoporosity facilitates the transformation of heavy fractions into lighter products by improving the access and molecular transport to/from the zeolite's active sites under the mild operation conditions.

Regarding the product distribution, one can see from Table 6.7 that Midas-BSR and ZS-24t-3.5p display significantly lower yields of the desired products than ZSM-5-P and MZ-0.5AAT. It is reasonable since the first two samples are much less active under the mild reaction conditions, inducing very large fractions of HCO (> 50 wt%). Nevertheless, there are obvious differences in the product distribution between Midas-BSR and ZS-24t-3.5p because of their different compositions. The industrial FCC catalyst containing zeolite

Y produces about 1.1 and 2.2 wt% yields of light olefins and coke respectively. At comparable conversion, ZS-24t-3.5p consisting of nano-ZSM-5 shows three orders of magnitude higher yield of light olefins (3 wt%) and less coke (1.5 wt%). The reason is that in the large pore zeolite Y (pore mouths diameter of 0.74 nm and pore intersection size (supercage) of 1.3 nm), polyaromatics can be formed through hydrogen transfer reactions involving cyclization, aromatization and condensation, leading to the increased coke formation and reduced light olefins [19,34]. In contrast, the medium pore zeolite ZSM-5 (pore mouths diameter of 0.52-0.56 nm and pore intersection size of 0.8 nm) severely suppresses the formation of polyaromatics because the limited space inside the medium pore channel cannot accommodate these intermediates [34,44]. This means that hydrogen transfer reactions are less prominent over the medium pore zeolite ZSM-5; therefore, the higher light olefins and lower coke are obtained. On the other hand, it should be noted that both catalysts are more selective toward LCO fractions rather than gasoline hydrocarbons. This is possibly due to the presence of mesoporous matrix coupled to the medium BS acidity, being consistent with the work of Corma et al. who carried out the cracking of gas oil over hierarchical USY [118].

ZSM-5-P yields considerably larger fractions of gasoline and light olefins reaching 36.4 and 20.0 wt%, respectively, compared to the first two catalyst samples (Midas-BSR and ZS-24t-3.5p), but noticeably less than those of MZ-0.5AAT. Under the same reaction conditions, MZ-0.5AAT produces about 40 wt% gasoline yield, an increase by 9.8% and 25.9 wt% light olefin yield, a relativeincrease by 30% with respect to its parent ZSM-5-P. The enhancement of the desired products primarily comes from the deeper cracking of heavy compounds in the LCO and HCO boiling ranges into lighter products thanks to the intracrystalline mesopores of MZ-0.5AAT. Additionally, MZ-0.5AAT shows a higher selectivity toward light olefins (light olefinicity, Table 6.7) than parent ZSM-5-P despite its higher conversion. This validates the assumption that the shortened diffusion path length provided by the hierarchical pore structure avoids the undesired secondary reactions of the primary light olefins.

To give more insights, the compositions of gasoline obtained over ZSM-5-P and MZ-0.5AAT, and the corresponding gas compositions were analyzed (Figure 6.3). It is clear that mesoporous MZ-0.5AAT boosts the concentration of light olefins while it lowers that of aromatic hydrocarbons. In other words, the primary light olefins are likely to be preserved over MZ-0.5AAT rather than undergo the oligomerization and subsequent aromatization reactions.

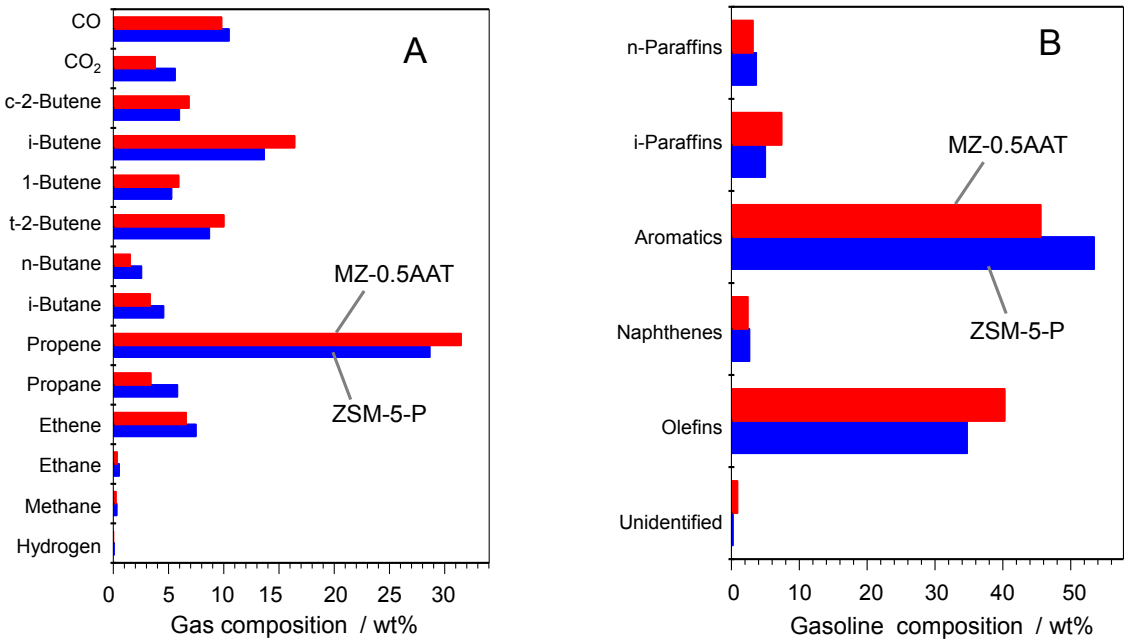

Figure 6.3 Gas (A) and gasoline (B) compositions in the catalytic cracking of WCO over ZSM-5-P and MZ-0.5AAT at 450 °C and a CTO ratio of 0.4 (g/g).

6.4.2 Catalytic performance of various catalysts under severe cracking conditions

Under severe cracking conditions (550 °C, CTO ratio = 0.4 g/g), MZ-0.5AAT still produces the highest yields of gasoline and light olefins. However, with the exceptional high light olefinicity, ZS-24t-3.5p appears to be the most selective catalyst for the production of light olefins from triglyceride based feedstock.

Table 6.8 gives the overall data on the catalytic performance of the different catalyst. One can see that the difference in the conversion over the tested catalysts is narrowed with the reaction temperature rise from 450 to 550 °C. Indeed, both ZSM-5-P and MZ-0.5AAT yield a comparable high conversion of ca. 91 wt% whereas Midas-BSR and ZS-24t-3.5p yield lower conversions of 59.8 and 70.6 wt%, respectively. The higher conversion over ZSM-5-P and MZ-0.5AAT can be attributed to their higher densities of BS compared to those of the latter samples (ZS-24t-3.5p and Midas-BSR). No remarkable influences of additional mesoporosity on the conversion can be derived, possibly because the overall reaction rate is controlled by the intrinsic kinetics rather than diffusion constraints at elevated temperatures.

Concerning the product distribution, it is obvious from table 6.8 that Midas-BSR again produces more coke (2.3 wt%) and less light olefins (10.6 wt%) compared to ZS-24t-3.5p (1.4 and 22.7 wt% respectively) under severe cracking conditions. The double light olefin yield over ZS-24t-3.5p in relation to Midas-BSR clearly indicates the higher selectivity

toward light olefins of the ZS catalyst. This is supported by their light olefinicity, which is plotted as a function of the conversion (Figure 6.4 A). In the comparable conversion range, a distinct higher light olefinicity over ZS-24t-3.5p than Midas-BSR has been achieved. These data further confirm the advantages of the medium pore zeolite ZSM-5 based catalyst (ZS-24t-3.5p) over the large pore zeolite Y based catalyst (Midas-BSR) in enhancing the production of light olefins while avoiding the coke formation in the cracking of triglycerides under FCC conditions.

Table 6.8 Catalytic performance of various catalysts in the catalytic cracking of WCO under the severe reaction conditions (550 °C, CTO ratio = 0.4 g/g).

Catalysts	Midas-BSR	ZS-24t-3.5p	ZSM-5-P	MZ-0.5AAT
Conversion (wt%)	59.8	70.6	91.5	90.5
Product yields (wt%)				
Total gas	19.1	30.7	48.8	46.4
Dry gas	2.4	2.6	8.2	7.2
LPG	11.6	22.1	33.7	33.9
Light olefins (C_2-C_4)	10.6	22.7	30.4	30.8
CO,CO_2	5.1	5.9	6.9	5.3
C_{5+}gasoline	34.4	32.2	35.0	37.1
LCO	18.2	17.7	4.0	6.9
HCO	22.0	11.7	4.5	2.6
Coke	2.3	1.4	1.2	1.0
Water	4.1	6.3	6.5	6.1
Mass balance (wt%)	99.8	99.4	98.1	97.6
Light olefinicity (%)	79.0	93.2	73.5	76.3

wt% on a feed basis.

From table 6.8, it can be seen that MZ-0.5AAT and ZSM-5-P yield a similar product distribution under severe cracking conditions. At almost complete conversions, the slightly higher fractions of gasoline and light olefins over MZ-0.5AAT compared to ZSM-5-P again validate the benefits of mesoporosity introduction. With respect to Midas-BSR and ZS-24t-3.5p, the samples MZ-0.5AAT and ZSM-5-P show higher yields of gasoline and light olefins. The higher yields of gasoline over ZSM-5-P and MZ-0.5AAT are attributed to the increased conversion and selectivity. The superior selectivy toward gasoline originates from the medium micropore size of ZSM-5 which directs the process toward the formation of gasoline range hydrocarbons (C_5-C_{10}) [33,34]. However, the higher yields of light olefins may mainly result from the almost complete conversion rather than the selectivity since

the light olefinicity over MZ-0.5AAT and ZSM-5-P drops sharply at the severe cracking conditions.

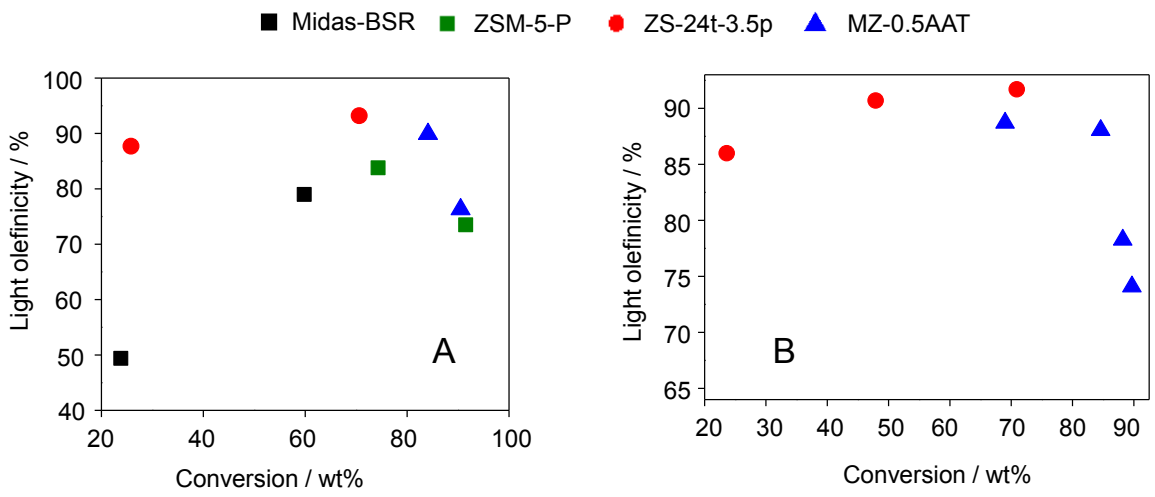

Figure 6.4 The light olefinicity over various catalysts as a function of the conversion in the cracking of WCO (A) and triolein (B). Reaction conditions: 450-550 °C, CTO ratio of 0.4 g/g.

It is likely from Figures 6.4 A, B that ZS-24t-3.5p possesses the highest selectivity toward light olefins (light olefinicity) among the studied catalysts. This conclusion is further supported by the exceptionally high light olefinicity obtained from the cracking of triolein over ZS-24t-3.5p, independent of cracking variables (Table 6.6). Tago et al. [119,120] studied the effect of crystal sizes and Si/Al ratios on the catalytic performance of ZSM-5 in the cracking of n-hexane at high temperature (550-650 °C). They found that with a similar density of acid sites (Si/Al ratio), nano-ZSM-5 displayed a higher light olefin yield than micro-sized ZSM-5 due to the improved mass transfer. Higher acid site densities (lower Si/Al ratios) increased the conversion of n-hexane but decreased the selectivity toward light olefins. It was found that increasing the acid site density promoted hydrogen transfer reactions which consumed light olefins to produce gasoline aromatics and light paraffins. A similar behavior can be seen from Figure 6.5 wherein MZ-0.5AAT shows higher concentrations of light paraffins and aromatic hydrocarbons with respect to ZS-24t-3.5p, further confirming the acceleration of hydrogen transfer reactions over MZ-0.5AAT due to its higher density of acid sites.

Thus, the highest selectivity toward light olefins over ZS-24t-3.5p among others can be attributed to the bimodal porous system coupled to the medium acidity which enables ZS-24t-3.5p not only to promote the formation of light olefins, but also effectively to protect them from further transformation.

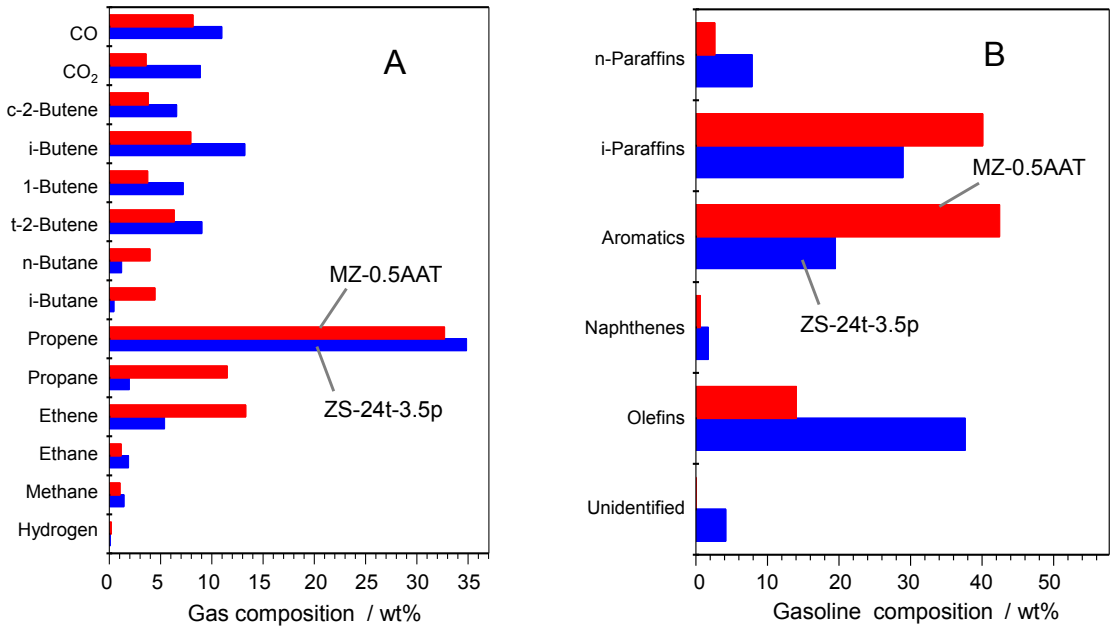

Figure 6.5 Gas (A) and gasoline (B) compositions in the catalytic cracking of WCO over ZS-24t-3.5p and MZ-0.5AAT at 550 °C and a CTO ratio of 0.4 (g/g).

6.5 Effect of feedstock composition

It has been reported that the yields of gasoline and light olefins dropped sharply when processing unsaturated triglycerides over FCC catalysts under FCC conditions [19,36].

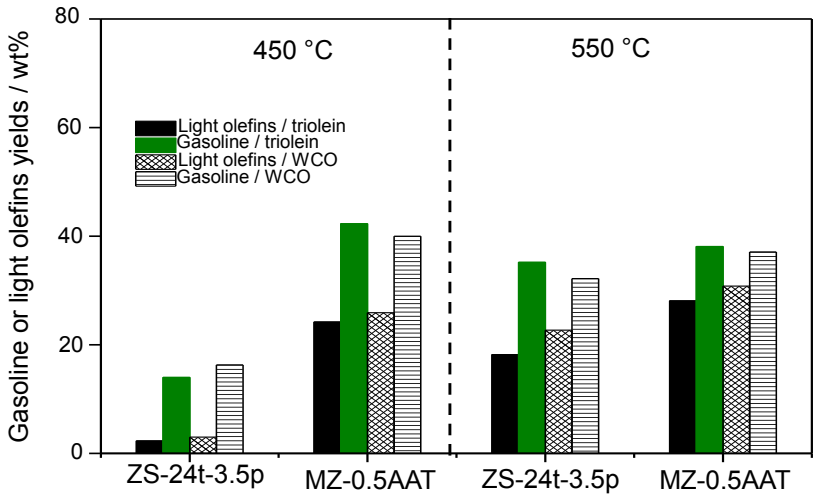

Figure 6.6 Effect of unsaturation degree of triglyceride based feedstock on the desired product yields over the prepared hierarchical ZSM-5 catalysts. Reaction conditions: 450-550 °C, a CTO ratio of 0.4 g/g.

The yields of gasoline and light olefins in the cracking of triolein (comprising predominantly unsaturated triglycerides) and WCO (containing less unsaturated triglycerides) over the prepared hierarchical ZSM-5 catalysts (MZ-0.5AAT and ZS-24t-3.5p) under the mild and severe cracking conditions are plotted in the Figure 6.6. It can be seen that the cracking of WCO over ZS-24t-3.5p and MZ-0.5AAT apparently produces more light olefins, but less gasoline than the cracking of triolien. The deeper cracking of WCO confirms its higher reactivity than triolein. However, the observed difference in the yields of gasoline and light olefins is not remarkable compared to that reported by Dupain et al. [19] who converted triglyceride based feedstock with FCC catalysts under realistic FCC conditions (525 °C and 4 s). They found that the cracking of saturated stearic acid produced significantly higher yields of gasoline and light olefins (approximately 57 and 14 wt% respectively) than the cracking of unsaturated triglyceride feedstock (rapeseed oil) (approximately 34 and 3 wt% for gasoline and light olefins respectively). It was postulated that the fast aromatization of unsaturated fatty acid over the large pore zeolite Y based catalyst led to the formation of polyaromatics that are less active. Taking it into account, the minor shift in the yields of gasoline and light olefins over the hierarchical catalysts further confirms that the formation of polyaromatics have been largely suppressed on the medium pore zeolite ZSM-5 of the hierarchical catalysts.

6.6 Proposed reaction pathway

A reaction pathway for the cracking of triglycerides over hierarchical ZSM-5 catalysts under FCC conditions is proposed by adopting the earlier reaction mechanism for the cracking of triglycerides in the literature [19,25,37] and taking into account the catalytic data obtained in this work (Figure 6.7).

The first step involves thermal decomposition of triglycerides to primarily form fatty acid by means of radical reactions, which is fast and independent of reaction temperature and catalyst characteristics. Then the further transformation of these fatty acids over ZSM-5 based catalysts follows two competitive routes: (i) deoxygenation and subsequent secondary cracking reactions and (ii) aromatization followed by dealkylation reactions. The occurrence of these different routes mainly depends on the unsaturation degree of fatty acids and reaction temperature. The former route is favored with saturated fatty acid like stearic acid at high reaction temperature (550 °C) while the aromatization of unsaturated fatty acid like oleic acid is facilitated at mild reaction temperature (450 °C). Since the limited space inside the medium pore channels of ZSM-5 cannot accommodate polyaromatics, it is expected that mainly alkyl mono-aromatic hydrocarbons can be formed in the latter route. The further transformation of these alkyl mono-aromatics may mimic the

cracking of cumene for which the presence of mesoporosity increases the accessibility of active sites and mass transfer, and consequently the catalyst effectiveness. This is responsible for the superior catalytic performance of mesoporous MZ-0.5AAT compared to its parent ZSM-5 under the mild operation conditions.

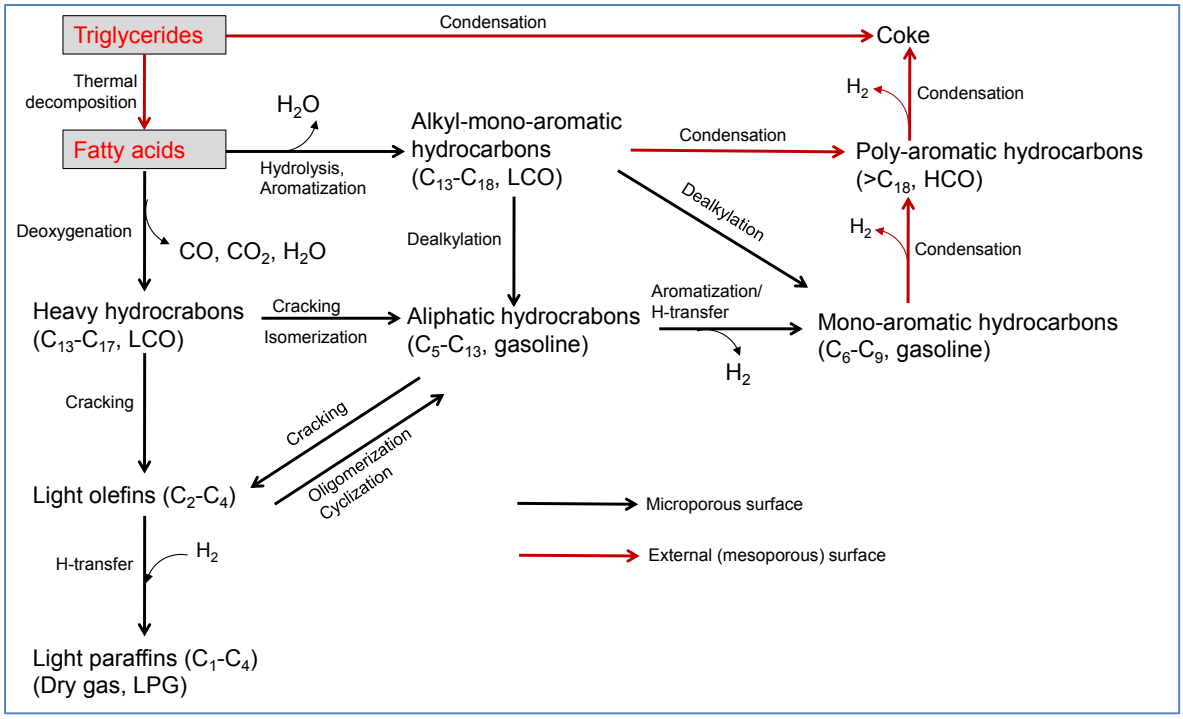

Figure 6.7 Proposed reaction pathway for catalytic cracking of triglycerides over hierarchical ZSM-5 based catalysts under FCC conditions.

On the other hand, the former route is dominated under severe operation conditions, increasing the extent of triglyceride cracking, and therefore more light products are produced. The medium acidity and shortened diffusion path length on the one hand enhance the formation of light olefins by cracking of heavier fractions, but on the other hand limit the secondary reactions of these primary light olefins. This explains why ZS-24t-3.5p is very selective for the production of light olefins. In addition, coke can be formed through the condensation process on the external surface.

6.7 Summary and conclusions

Thus, it is evident that the hierarchical ZSM-5 based catalysts (MZ-0.5AAT and ZS-24t-3.5p) exhibit a superior performance compared to the commercial Al-rich ZSM-5 (ZSM-5-

P) and industrial FCC catalysts (Midas-BSR) in terms of activity and selectivity toward the desired products. The industrial FCC catalyst displays the poorest performance, giving the least conversion and light olefins yield. Compared to commercial (parent) ZSM-5 (ZSM-5-P), which has been known as the best zeolite type catalyst for the cracking of triglycerides, mesoporous ZSM-5 material (MZ-0.5AAT) enhances the conversion, gasoline and light olefin yields by ca. 14%, 10% and 30%, respectively, under mild operation conditions. The improved catalytic performance originates from the presence of substantial mesoporosity that enables the mesoporous ZSM-5 material to effectively crack alkyl mono-aromatic species, which mainly result from the fast aromatization of unsaturated fatty acids. Simultaneously this catalyst also hinders the undesired secondary reactions of the primary light olefins. However, the selectivity toward light olefins over MZ-0.5AAT and ZSM-5-P experiences a dramatic reduction at higher temperatures or CTO ratios, suggesting that the undesired secondary reactions come to the foreground at the severe operation conditions. The advantage of ZS-24t-3.5p with respect to the other catalysts (Midas-BSR, ZSM-5-P and MZ-0.5AAT) is the exceptionally high selectivity for the production of light olefins, regardless of the operation variables, due to the fast diffusion rate provided by the bimodal pore system and the medium acidity. In addition, no significant effect of unsaturation degree of triglyceride feedstock on the performance of the hierarchical ZSM-5 based catalysts can be evidenced, further confirming their advantages over conventional zeolite Y based FCC catalysts.

Chapter 7

Summary and Outlook

This chapter summarizes the main findings and contributions of the thesis, and evaluates them with regard to application perspectives along with some recommendations for further work.

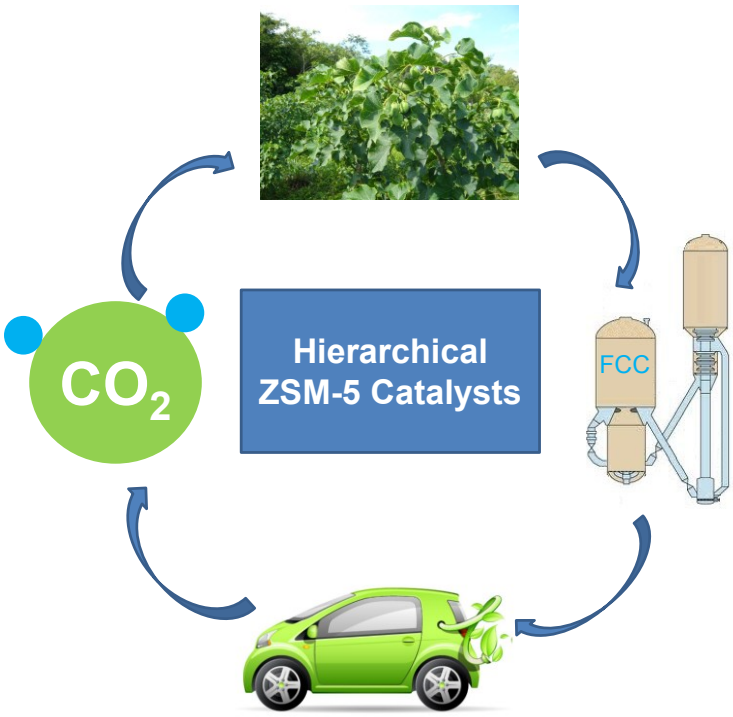

7.1 Mesoporous ZSM-5 materials by post-synthesis modifications

Post-synthesis modifications of commercial ZSM-5 represent the most practical way to prepare mesoporous ZSM-5 (MZ) materials. However, the success of this approach requires optimizing post-treatment variables for individual starting zeolites. In this respect, the post-synthesis treatment of commercial ZSM-5 zeolites with a very low Si/Al ratio of ca. 10 has not been explored to date although they are of practical importance.

In the present work, therefore, the two-step post-synthesis protocol involving the optimization of alkaline treatment and subsequent strong acid washing has been established for the preparation of MZ materials from commercial Al-rich ZSM-5 (Si/Al = 11). It is shown that a mild alkaline treatment generates little mesoporosity, but increases the total acidity mainly due to the removal of amorphous domains inherent in commercial ZSM-5. The zeolite framework is hardly affected by such mild base treatments. As exposed to 0.5 M NaOH, the formation of mesopores becomes substantial at the expense of micropore volume. However, the dealumination of framework Al forming extra-framework Al occurs along with the desilication process, which reduces the density of strong Brønsted acid sites. More severe alkaline treatment causes an excessive dissolution of zeolite crystals, resulting in the drastic loss in the BET surface area, micropore volume, recovery yield, strength and density of acid sites. Hence, the optimal NaOH concentration for substantial mesoporosity development without losing significant intrinsic microporosity should be 0.5 M under the investigated conditions.

The subsequent strong acid washing completely removes Al-rich debris deposited on the external surface, uncovering the micro-/mesoporous network; thereby the Si/Al ratio, contribution of strong Brønsted acid sites and necessary textural properties are greatly enhanced. However, the strong acid treatment decreases the recovery yield and total acidity. Upon the strong acid washing, the optimal sample exhibits the largest external surface (S_{meso} = 297 m^2/g) with the preserved intrinsic zeolite characteristics (strong Brønsted site density) and relatively high recovery yield (62%).

Gas phase cracking of cumene and 1,3,5-tri-isopropyl-benzene (TIBP) was performed over parent ZSM-5 and the final MZ catalysts to assess the catalytic benefits of generated mesoporosity in acid-catalyzed reactions. Cumene cracking reveals that under the diffusion-controlled regime, the presence of mesoporosity indeed increases cumene reactivity of the MZ catalyst as the zeolite strong Brønsted density is mainly retained. The catalytic activity of the external surface probed by TIPB cracking indicates that the formation of larger pores and the enrichment of Brønsted sites on the external surface caused by base-acid treatment are favorable for conversion of large molecules like TIPB.

In both cases, the increased catalytic activity can be attributed to the enhanced accessibility and physical transport rates provided by substantial mesoporosity.

7.2 Nano-ZSM-5/SBA-15 analog composites by high temperature synthesis

Compared to the post-synthesis design of mesoporous ZSM-5 materials, the direct synthesis of nano-ZSM-5/SBA-15 analog (ZS) composite from ZSM-5 precursors by high temperature synthesis is more complicated, but it provides more precise control over the distribution of microporous and mesoporous phases. In such hierarchically structured materials, nano-ZSM-5 domains hold major active sites, and their accessibility is enhanced by mesoporous phase serving as a matrix. Thus, nano-ZSM-5 domains should be well dispersed in such a porous matrix whose mesostructures are maintained under severe operation conditions (i.e. in the regeneration conditions of the FCC process). To achieve this, the present work considers two aspects: improving hydrothermal stability and acidic properties of SBA-15 analogs (assembled from ZSM-5 nanoseeds by pH adjustment prior to high temperature hydrothermal treatment) and employing them as an advanced matrix for in-situ dispersion of nano-ZSM-5 crystals (which are initially formed in the ZSM-5 precursor solution).

It is found that the htt-pH (hydrothermal treatment pH) is a decisive factor for the formation of an ordered mesostructure with increased aluminum incorporation, as demonstrated in the preparation of SBA-15 analogs from ZSM-5 nanoseeds at high temperature. A highly condensed, ordered mesoporous SBA-15 analog with significantly improved hydrothermal stability and acidic properties can be optimally prepared at an htt-pH of 3.5 and 200 °C. Higher htt-pH values partially destroy the ordered mesostructure while at lower htt-pH values, the incorporated Al content and consequent total acidity are declined.

The precrystallization time of preformed ZSM-5 precursors controls the distribution of nano-ZSM-5 phase and SBA-15 analogs phase, and this behavior was investigated systematically under the optimized conditions (htt-pH = 3.5 and 200 °C). Starting from shortly precrystallized ZSM-5 precursors (6 or 12 h), mainly mesoporous SBA-15 analogs containing zeolite building units are obtained, whereas upon extending the precrystallization time to 36 h, nano-ZSM-5 crystals are dominated. In between, a ZS composite of which spherical ZSM-5 nanocrystals (40-50 nm in diameters) well-dispersed in highly condensed, ordered mesoporous SBA-15 analogs can be prepared from the ZSM-5 precursors precrystallized for 24 h. The micro-/mesoporous structures of the ZS

composite are well retained even upon steaming at 800 °C for 24 h with almost unchanged pore size and volume, suggesting its remarkable hydrothermal stability. The steaming stability of nano-ZSM-5 phase is well-documented and originates from the crystalline framework made up of SiO_4 and AlO_4 units. For the mesoporous phase, it might be related to the retention of zeolite building units and the high degree of silica condensation in the mesoporous walls as shown by IR and ^{29}Si-MAS-NMR analyses, respectively.

The total acidity of the ZS composite varies slightly with the precrystallization time. Moreover, the total number of acid sites is apparently enhanced by the interaction between nano-ZSM-5 phase and mesoporous SBA-15 analogs phase. IR spectroscopy of adsorbed pyridine (py-IR) evidenced that the concentration of strong Brønsted acid sites increases with the nano-ZSM-5 content. In contrast, the number of strong Lewis sites severely depends on the fraction of mesoporous phase. A good correlation between the cumene conversion and strong Brønsted site density has been established, further confirming the data of py-IR. It is noteworthy that the ZS composite yields a high cumene conversion, being comparable to that of commercial ZSM-5 despite its much lower density of strong Brønsted acid sites. This implies that the presence of mesoporous SBA-15 analogs phase in the ZS composite enhances the access and molecular transport to/from the active acid sites of nano-ZSM-5 domains, thereby improving the cumene reactivity over the ZS composite. Contrary to the cracking of cumene, which is controlled by the strength of Brønsted sites, the TIPB conversion is primarily determined by the accessibility of acid sites. Accordingly, the cracking of bulky TIPB is favored on the external surface (mesoporous phase) rather than on sites provided by nano-ZSM-5 phase.

7.3 Performance of hierarchical ZSM-5 based catalysts in the cracking of triglyceride-rich biomass under FCC conditions

The hierarchical MZ and ZS materials represent promising catalysts for conversion of triglyceride-rich biomass into gasoline-range hydrocarbons and light olefins under FCC conditions. Compared to commercial Al-rich ZSM-5 (ZSM-5-P) and industrial FCC catalyst (Midas-BSR), the hierarchical catalysts show a superior performance in terms of activity and yield toward the desired products.

Of the four studied catalysts, the industrial FCC catalyst displays the poorest performance, giving the least conversion and yield of light olefins, but the highest coke formation. This indicates that the industrial FCC catalyst based on large pore zeolite Y, developed for petroleum processing, is not the ideal catalyst for converting bio-feedstock

like triglyceride-rich biomass.

Compared to commercial ZSM-5 (ZSM-5-P), which has been known as the best zeolite type catalyst for the cracking of triglycerides, the MZ catalyst enhances the conversion, gasoline and light olefin yields by approximately 14%, 10% and 30%, respectively, under the mild operation conditions (450 °C, CTO ratio = 0.4 g/g). The improved activity is particularly noticeable when considering the fact that the MZ has a lower acidity than ZSM-5-P. The increased utilization of acid sites is attributed to the increased accessibility and accelerated molecular transport provided by the substantial fraction of mesoporosity. On the other hand, the enhanced yields of the desired products can be assigned to the inhibited undesirable secondary reactions induced by the shortened micropore diffusion path length. However, the selectivity toward light olefins and gasoline over the MZ experiences a dramatic reduction at higher temperatures or CTO ratios, suggesting that the undesired secondary reactions take place drastically under the severe operation conditions.

The main advantage of ZS-24t-3.5p with respect to the other catalysts (Midas-BSR, ZSM-5-P and MZ-0.5AAT) is the very high selectivity toward light olefins, regardless of the operation variables. The fast mass transfer and medium acidity are probably responsible for the superior catalytic performance of the ZS composite.

The negative effect of unsaturated triglycerides on the yield of desired products has been effectively suppressed with the hierarchical ZSM-5 based catalysts. This is because the space inside the the medium pore channel of ZSM-5 cannot accommdate such large polyaromatic species; therefore, the yields of gasoline and light olefins are enhanced.

7.4 Outlook

Since petroleum prices are increasing as a result of oil depletion, it is expected that biofuels will play an ever-increasing role in the future transportation fuel supply. Processing triglyceride-rich biomass in conventional FCC units represents a promising option for the future to produce biofuels and chemicals. The work described in this thesis might open new opportunities for the synthesis and application of hierarchical zeolitic catalysts for such a process by the petroleum refinery infrastructure. Future work should focus on the characterization of the external surface's acid sites generated by the intracrystalline or intercrystalline mesoporosity, and their role in the catalytic cracking of triglycerides. The knowledge about the catalytic properties of external surfaces, particularly in terms of nature and strength of acid sites would enable to further improve the catalytic performance of hierarchical catalysts. Also, the post-synthesis design of mesoporous ZSM-5 materials starting from low Al containing ZSM-5 and their application

in the cracking of triglycerides should be tried. A better understanding of the mechanism of zeolite evolution will benefit the preparation of nano-ZSM-5 based composites from zeolite precursors. More credits should be paid to the precise control over the distribution of nano-ZSM-5 and SBA-15 analogs; thereby the catalytic properties of the resulting composite can be tuned during preparation. Several attempts are required to minimize the undesired secondary reactions over mesoporous ZSM-5 materials at high temperature. In this respect, much deeper studies in reaction engineering with regard to contact time and mass transfer are required. Although the general reaction pathway of catalytic cracking of triglycerides has been proposed, the detailed reaction mechanism remains unclear. Both experimental and theoretical studies would shed more light on this. Finally, from practical point of view, shaping hierarchical zeolitic catalysts in the form of FCC catalysts and checking their catalytic performance in the cracking of triglycerides under FCC conditions deserve more dedicated future studies.

In conclusion, the introduction of a secondary network of mesopores, either intracrystalline (mesoporous ZSM-5 materials) or intercrystalline (nano-ZSM-5 based composites) mesoporosity indeed improves the catalytic performance of ZSM-5 in the cracking of triglycerides under FCC conditions. The superior catalytic performance of hierarchical ZSM-5 catalysts originates from the enhanced accessibility and mass transfer provided by substantial mesoporosity while retaining the intrinsic catalytic properties of ZSM-5 (strong Brønsted acid sites and shape selectivity). This enables hierarchical ZSM-5 catalysts to effectively convert triglycerides, independent of unsaturation degree, to gasoline-range hydrocarbons and light olefins as well, under FCC conditions.

8 References

[1] L. Caspeta, N. A. A. Buijs, J. Nielsen, Energy Environ. Sci. 6 (2013) 1077–1082.

[2] G. W. Huber, S. Iborra, A. Corma, Chem. Rev. 106 (2006) 4044–4098.

[3] L. Petrus, M. A. Noordermeer, Green Chem. 8 (2006) 861–867.

[4] J. A. Melero, J. Iglesias, A. Garcia, Energy Environ. Sci. 5 (2012) 7393–7420.

[5] World Energy Outlook 2013, International Energy Agency (IEA), http://www.worldenergyoutlook.org/publications/weo-2013/

[6] N. Taufiqurrahmi, S. Bhatia, Energy Environ. Sci. 4 (2011) 1087–1112.

[7] G. W. Huber, A. Corma, Angew. Chem. Int. Ed. 46 (2007) 7184–7201.

[8] M. Al-Sabawi, J. Chen, S. Ng, Energy Fuels 26 (2012) 5355–5372.

[9] M. C. Math, S. P. Kumar, S. V. Chetty, Energy for Sustainable Development 14 (2010) 339–345.

[10] A. B. Chhetri, K. C. Watts, M. R. Islam, Energies 1 (2008) 3–18.

[11] A. Sivasamy, K. Y. Cheah, P. Fornasiero, F. Kemausuor, S. Zinoviev, S. Miertus, ChemSusChem 2 (2009) 278–300.

[12] Opportunities for Biorenewables in Oil Refineries, UOP LLC, http://www.osti.gov/scitech/biblio/861458

[13] NExBTL renewable diesel, Nesteoil, http://www.nesteoil.com/default.asp?path=1,41,11991,22708,22709,22710

[14] J. K. Satyarthi, T. Chiranjeevi, D. T. Gokak, P. S. Viswanathan, Catal. Sci. Technol. 3 (2013) 70–80.

[15] T. V. M. Rao, X. Dupain, M. Makkee, Micropor. Mesopor. Mater. 164 (2012) 148–163.

[16] S. Yan, C. DiMaggio, H. Wang, S. Mohan, M. Kim, L. Yang, S. O. Salley, K. Y. Simon Ng, Current Catal. 1 (2012) 41–51.

[17] K. D. Maher, D.C. Bressler, Bioresoure Technol. 98 (2007) 2351–2368.

[18] J. A. Melero, M. M. Clavero, G. Calleja, A. Garcıa, R. Miravalles, T. Galindo, Energy Fuels 24 (2010) 707–717.

[19] X. Dupain, D. J. Costa, C. J. Schaverien, M. Makkee, J. A. Moulijn, Appl. Catal. B: Environ. 72 (2007) 44–61.

[20] P. Bielansky, A. Weinert, C. Schönberger, A. Reichhold, Fuel Processing Technol. 92 (2011) 2305–2311.

[21] A.W. Schwab, G.J. Dykstra, E. Selke, S.C. Sorenson, E.H. Pryde, JAOCS 65 (1988) 1781–1786.

[22] R. O. Idem, S. P.R. Katikaneni, N. N. Bakhshi, Fuel Processing Technol. 51 (1997) 101–125.

[23] D. G. Lima, V. C. D. Soares, E. B. Ribeiro, D. A. Carvalho, E. C. V. Cardoso, F. C. Rassi, K. C. Mundim, J. C. Rubim, P. A. Z. Suarez, J. Anal. Appl. Pyrolysis 71 (2004) 987–996.

[24] R. O. Idem, S. P. R. Katikaneni, N. N. Bakhshi, Energy Fuels 10 (1996)1150–1162.

[25] S. P. R. Katikaneni, J. D. Adjaye, R. O. Idem, N. N. Bakhshi, Ind. Eng. Chem. Res. 35 (1996) 3332–3346.

[26] Y. S. Ooi, S. Bhatia, Micropor. Mesopor. Mater. 102 (2007) 310–317.

[27] S. P. R. Katikaneni, J. D. Adjaye, N. N. Bakhshi, Energy Fuels 9 (1995) 599–609.

[28] Y. S. Ooi, R. Zakaria, A. R. Mohamed, S. Bhatia, Catal. Commun. 5 (2004) 441–445.

[29] F. A. Twaiq, N. A. M. Zabidi, A. R. Mohamed, S. Bhatia, Fuel Processing Technol. 84 (2003) 105–120

[30] T. A. Ngo, J. Kim, S. K. Kim, S. S. Kim, Energy 35 (2010) 2723–2728.

[31] Y. S. Ooi, R. Zakaria, A. R. Mohamed, S. Bhatia, Biomass and Bioenergy 27 (2004) 477–484.

[32] F. A. A. Twaiq, A. R. Mohamad, S. Bhatia, Fuel Processing Technol. 85 (2004) 1283–1300.

[33] F. A. A. Twaiq, N. A. M. Zabidi, S. Bhatia, Ind. Eng. Chem. Res. 38 (1999) 3230–3237.

[34] D. Chen, N. I. Tracy, D. W. Crunkleton, G. L. Price, Appl. Catal. A: Gen. 384 (2010) 206–212.

[35] N. Taufiqurrahmi, A. R. Mohamed, S. Bhatia, Bioresource Technol. 102 (2011) 10686–10694.

[36] V. P. Doronin, O. V. Potapenko, P. V. Lipin, T. P. Sorokina, L. A. Buluchevskaya, Petroleum Chemistry 52 (2012) 392–400.

[37] J. A. Botas, D. P. Serrano, A. García, R. Ramos, Appl. Catal. B: Environ. 145 (2014) 205–215.

[38] Y. S. Ooi, R. Zakaria, A. R. Mohamed, S. Bhatia, Appl. Catal. A: Gen. 274 (2004) 15–23.

[39] P. Bielansky, A. Reichhold, C. Schoenberger, Chemical Engineering and Processing 49 (2010) 873–880.

[40] V. P. Doronin, O. V. Potapenko, P. V. Lipin, T. P. Sorokina, Fuel 106 (2013) 757–765.

[41] T. V. M. Rao, M. M. Clavero, M. Makkee, ChemSusChem 3 (2010) 807–810.

[42] P. B. Weisz, W. O. Haag, P. G. Rodewald, Science 206 (1979) 57–58.

[43] M. Stoecker, Micropor. Mesopor. Mater. 82 (2005) 257–292.

[44] A. Corma, J. Catal. 216 (2003) 298–312.

[45] M. Rigutto, Cracking and hydrocracking, in Zeolites and Catalysis, Synthesis, Reactions and Applications, Wiley-VCH, Weinheim, 2010, pp 547–578.

[46] L. Zhang, A. N. C. van Laak, P. E. de Jongh, K. P. de Jong, Textural characterization of mesoporous zeolites, in Zeolites and Catalysis, Synthesis, Reactions and Applications, Wiley-VCH, Weinheim, 2010, pp 237–274.

[47] J. Pérez-Ramírez , C. H. Christensen, K. Egeblad, C. H. Christensen, J. C. Groen, Chem. Soc Rev 37 (2008) 2530–2542.

[48] K. Möller, T. Bein, Chem. Soc. Rev. 42 (2013) 3689-3707.

[49] R. Chal, C. Gérardin, M. Bulut, S. van Donk, ChemCatChem 3 (2011) 67–81.

[50] S. van Donk, A. H. Janssen, J. H. Bitter, K. P. de Jong, Catal. Rev. Sci. Eng. 45 (2003) 297–319.

[51] J. C. Groen, J. A. Moulijn, J. Pérez-Ramírez, J. Mater. Chem. 16 (2006) 2121–2131.

[52] J. Čejka, S. Mintova, Catal. Rev. Sci. Eng. 49 (2007) 457–509.

[53] Y. Liu, T. J. Pinnavaia, J. Mater. Chem. 12 (2002) 3179–3190.

[54] X. Meng, F. Nawaz, F. S. Xiao, Nano Today 4 (2009) 292–301.

[55] L. H. Chen, X. Y. Li, J. C. Rooke, Y. H. Zhang, X.-Y. Yang, Y. Tang, F. S. Xiao, B. L. Su, J. Mater. Chem. 22 (2012) 17381–17403

[56] D. Verboekend, J. Pérez-Ramírez, Catal. Sci. Technol.1 (2011) 879–890.

[57] R. M. Dessau, E. W. Valyocsik, N. H. Goeke, Zeolites 12 (1992) 776–779.

[58] A. Čižmek, B. Subotic, I. Smit, A. Tonejc, R. Aiello, F. Crea, A. Nastro, Micropor. Mater. 8 (1997) 159–169.

[59] R. L. V. Mao, S. T. Le, D. Ohayon, F. Caillibot, L. Gelebart, G. Denes, Zeolites 19 (1997) 270–278.

[60] M. Ogura, S. Y. Shinomiya, J. Tateno, Y. Nara, E. Kikuchi, H. Matsukata, Chem. Lett. 29 (2000) 82–83.

[61] J. C. Groen, L. A. A. Peffer, J. A. Moulijn, J. Pérez-Ramírez, Chem. Eur. J. 11 (2005) 4983–4994.

[62] J. C. Groen, J. A. Moulijn, J. Pérez-Ramírez, Micropor. Mespor. Mater. 87 (2005) 153–161.

[63] J. C. Groen, J. C. Jansen, J. A. Moulijn, J. Pérez-Ramírez, J. Phys. Chem. B 108 (2004) 13062–13065.

[64] J. C. Groen, Ph.D Thesis: Mesoporous zeolites obtained by desilication, the department DelftChemTech, Faculty of Applied Sciences, Delft University of Technology (2007).

[65] D. Verboekend, J. Pérez-Ramírez, ChemSusChem 2014, doi:10.1002/cssc.201301313

[66] D. Verboekend, J. Pérez-Ramírez, Chem. Eur. J. 17 (2011) 1137–1147.

[67] D. Verboekend, S. Mitchell, M. Milina, J. C. Groen, J. Pérez-Ramírez, J. Phys. Chem. C 115 (2011) 14193–14203.

[68] Y. Wan, D. Zhao, Chem. Rev. 107 (2007) 2821–2856.

[69] Y. Liu, W. Zhang, T. J. Pinnavaia, J. Am. Chem. Soc. 122 (2000) 8791–8792.

[70] Y. Han, S. Wu, Y. Sun, D. Li, F. S. Xiao, J. Liu, X. Zhang, Chem. Mater. 14 (2002) 1144–1148.

[71] Y. Liu, T. J. Pinnavaia, Chem. Mater. 14 (2002) 3–5.

[72] Y. Liu, W. Zhang, T. J. Pinnavaia, Angew. Chem.113 (2001) 1295–1298

[73] L. Frunz, R. Prins, G. D. Pirngruber, Micropor. Mesopor. Mater. 88 (2006) 152–162.

[74] P. Waller, Z. Shan, L. Marchese, G. Tartaglione, W. Zhou, J. C. Jansen, T. Maschmeyer, Chem. Eur. J. 10 (2004) 4970–4976.

[75] F. N. Gu, F. Wei, J. Y. Yang, N. Lin, W. G. Lin, Y. Wang, J. H. Zhu, Chem. Mater. 22 (2010) 2442–2450.

[76] Y. Xia, R. Mokaya, J. Mater. Chem. 14 (2004) 863–870.

[77] Y. Xia, R. Mokaya, J. Mater. Chem. 14 (2004) 3427–3435.

[78] L. Liu, G. Xiong, X. Wang, J. Cai, Z. Zhao, Micropor. Mesopor. Mater. 123 (2009) 221–227.

[79] D. S. Lee, T.-K. Liu, React. Kinet. Catal. Lett. 72 (2001) 209–218.

[80] D. Pan, P. Yuan, L. Zhao, N. Liu, L. Zhou, G. Wei, J. Zhang, Y. Ling, Y. Fan, B. Wei, H. Liu, C. Yu, X. Bao, Chem. Mater. 21 (2009) 5413–5425.

[81] X. Yang, S. Zhang, Z. Qiu, G. Tian,Y. Feng, F.S. Xiao, J. Phys. Chem. B 108 (2004) 4696–4700.

[82] M. S. Holm, E. Taarning, K. Egeblad, C. H. Christensen, Catal. Today 168 (2011) 3–16.

[83] L. Zhao, B. Shen, J. Gao, C. Xu, J. Catal. 258 (2008) 228–234.

[84] J. Pérez-Ramírez, D. Verboekend, A. Bonilla, S. Abello, Adv. Funct. Mater. 19 (2009) 3972–3979.

[85] D. H. Choi, J. W. Park, J.-H. Kim, Y. Sugi, Polym. Degrad. Stab. 91 (2006) 2860–2866.

[86] M. Bjorgen, F. Joensen, M. S. Holm, U. Olsbye, K.-P. Lillerud, S. Svelle, Appl. Catal. A: Gen. 345 (2008) 43–50.

[87] J. Li, X. Li, G. Zhou, W. Wang, C. Wang, S. Komarneni, Y. Wang, Appl. Catal. A: Gen. 470 (2014) 115–122.

[88] L. Huang, W. Guo, P. Deng, Z. Xue, Q. Li, J. Phys. Chem. B 104 (2000), 2817–2823.

[89] D. P. Serrano, R.A. García, G. Vicente, M. Linares, D. Procházková, J. Cˇejka, J. Catal. 279 (2011) 366–380.

[90] M. Milina, S. Mitchell, Z. D. Trinidad, D. Verboekend, J. Pérez-Ramírez, Catal. Sci. Technol. 2 (2012) 759–766.

[91] B. Gil, Ł. Mokrzycki, B. Sulikowski, Z. Olejniczak, S. Walas, Catal. Today 152 (2010) 24–32.

[92] M. Milina, S. Mitchell, N. L. Michels, J. Kenvin, J. Pérez-Ramírez, J. Catal. 308 (2013) 398–407.

[93] H. Mochizuki, T. Yokoi, H. Imai, S. Namba, J. N. Kondo, T. Tatsumi, Appl. Catal. A: Gen. 449 (2012) 188–197.

[94] M. Ogura, S. Shinomiya, J. Tateno, Y. Nara, M. Nomura, E. Kikuchi, M. Matsukata, Appl. Catal. A: Gen.219 (2001) 33–43

[95] K. Egeblad, C. H. Christensen, M. Kustova, C. H. Christensen, Chem. Mater. 20 (2008) 946–960.

[96] A. Corma, B. W. Wojciechowski, Catal. Rev. Sci. Eng. 24 (1982) 1–65.

[97] S. Al-Khattaf, H. de Lasa, Appl. Catal. A: Gen. 226 (2002) 139–153.

[98] S. Al-Khattaf, J. A. Atias, K. Jarosch, H. de Lasa, Chem. Eng. Sci. 57 (2002) 4909 – 4920.

[99] B.Tokay, M. Somer, A. Erdem-Şenatalara, F. Schüth, R. W. Thompson, Micropor. Mesopor. Mater. 118 (2009) 143–151.

[100] S. A. Bagshaw, N. I. Baxter, D. R. M. Brew, C. F. Hosie, N. Yuntong, S. Jaenicke, C. G. Khuan, J. Mater. Chem. 16 (2006) 2235–2244.

[101] J. Wang, J. C. Groen, W. Yue, W. Zhou, M.-O. Coppens, J. Mater. Chem. 18 (2008) 468–474.

[102] S. Wu, Y. Han, Y. Zou, J. Song, L. Zhao, Y. Di, S. Liu, F.-S. Xiao, Chem. Mater. 16 (2004) 486–492.

[103] N. Xiao, L. Wang, S. Liu, Y. Zou, C. Wang, Y. Ji, J. Song, F. Li, X. Meng, F.-S. Xiao, J. Mater. Chem. 19 (2009) 661–665.

[104] Y. Han, N. Li, L. Zhao, D. Li, X. Xu, S. Wu, Y. Di, C. Li, Y. Zou, Y. Yu, F.-S. Xiao, J. Phys. Chem. B 107 (2003) 7551–7556.

[105] C. J. H. Jacobsen, C. Madsen, T. V. W. Janssens, H. J. Jakobsen, J. Skibsted, Micropor. Mesopor. Mater. 39 (2000) 393–401.

[106] W. Guo, C. Xiong, L. Huang, Q. Li, J. Mater. Chem. 11 (2001) 1886–1890.

[107] P. Morales-Pacheco, J. M. Domínguez, L. Bucio, F. Alvarez, U. Sedran, M. Falco, Catal. Today 166 (2011) 25–38.

[108] Z. Xue, T. Zhang, J. Ma, H. Miao, W. Fan, Y. Zhang, R. Li, Micropor. Mesopor. Mater. 151 (2012) 271–276.

[109] Z. Luan, J. A. Fournier, Micropor. Mesopor. Mater. 79 (2005) 235–240.

[110] G. Crepeau, V. Montouillout, A. Vimont, L. Mariey, T. Cseri, F. Mauge, J. Phys. Chem. B 110 (2006) 15172–15185.

[111] X. H. Vu, N. Steinfeldt, U. Armbruster, A. Martin, Micropor. Mesopor. Mater. 164 (2012) 120–126.

[112] R. H. Harding, A. W. Peters, J. R. D. Nee, Appl. Catal. A: Gen. 221 (2001) 389–396.

[113] H. Li, P. Yu, B. Shen, Fuel Processing Technol. 90 (2009) 1087–1092.

[114] J. W. Alencar, P. B. Alves, A. A. Craveiro, J. Agric. Food Chem. 31 (1983) 1268–1270.

[115] A. Aitani, T. Yoshikawa, T. Ino, Catal. Today 60 (2000) 111–117.

[116] X. Zhao, T. G. Roberie, Ind. Eng. Chem. Res. 38 (1999) 3847–3853.

[117] S. P. R. Katikaneni, J. D. Adjaye, R. O. Idem, N. N. Bakhshi, J. Am. Oil Chem. Soc. 75 (1998) 381–391.

[118] C. Martínez, D. Verboekend, J. Pérez-Ramírez, A. Corma, Catal. Sci. Technol. 3 (2013) 972–981.

[119] H. Konno, T. Tago, Y. Nakasaka, R. Ohnaka, J. Nishimura, T. Masuda, Micropor. Mesopor. Mater. 175 (2013) 25–33.

[120] T. Tago, H. Konno, Y. Nakasaka, T. Masuda, Catal. Surv. Asia 16 (2012) 148–163.

Appendix A

List of Abbreviations, Acronyms and Symbols

AAS	Atomic Absorption Spectroscopy
ASTM	American Society for Testing and Materials
AT	Alkaline Treatment
AAT	Alkaline - Acid Treatment
BET	Brunauer-Emmet-Teller model
BJH	Barret-Joyner-Halenda model
BS	Brønsted acid Sites
°C	Degree Celsius
etc.	et cetera
e.g.	exempli gratia
et al.	et alii
FCC	Fluid Catalytic Cracking
FID	Flame Ionization Detector
FTIR	Fourier Transformation Infrared Spectroscopy
GC	Gas Chromatography
GHSV	Gas Hourly Space Velocity
HTP	High Temperature Peak
ICP - OES	Inductive Coupled Plasma Optical Electron Spectroscopy
i.e.	id est
Py-IR	Infrared Spectroscopy of Adsorbed Pyridine
K	Kelvin
MAS-NMR	Magic Angle Spinning Nuclear Magnetic Resonance
LTP	Low Temperature Peak
LS	Lewis Sites
MZ	Mesoporous ZSM-5
NH_3-TPD	Temperature Programmed Desorption of Ammonia
nm	Nanometer
OMM	Ordered Mesoporous Materials
PIONA	Paraffin, I-paraffin, Olefin, Naphthene, Aromatic
SCT-MAT	Short Contact Time Microactivity Test

SEM	Scanning Electron Microscopy
SAXS	Small Angle X-ray Scattering
SIMDIST	Simulated Distillation
ZS	ZSM-5/SBA-15 composites
TCD	Thermal Conductivity Detector
TEM	Transmission Electron Microscopy
XRD	X-ray Diffraction
WAXS	Wide Angle X-ray Scattering
WCO	Waste Cooking Oil
WHSV	Weight Hourly Space Velocity

Appendix B

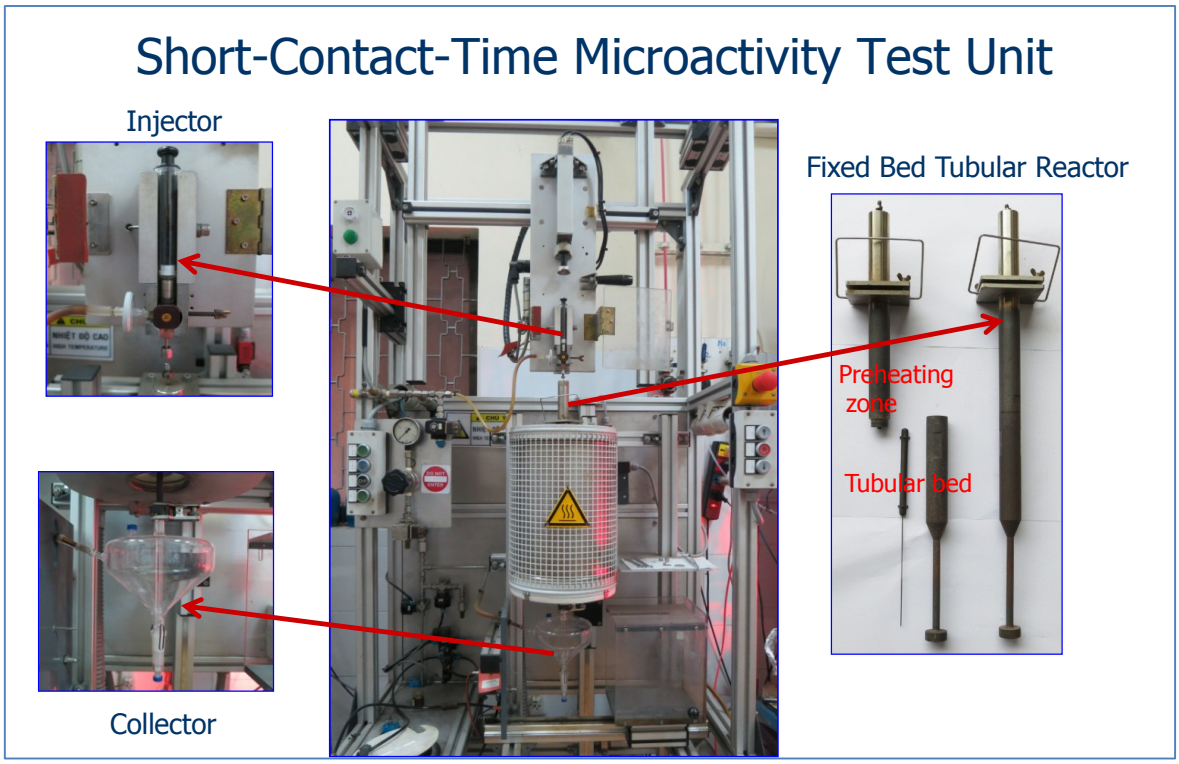

Figure B1 Experimental set-up of SCT-MAT.

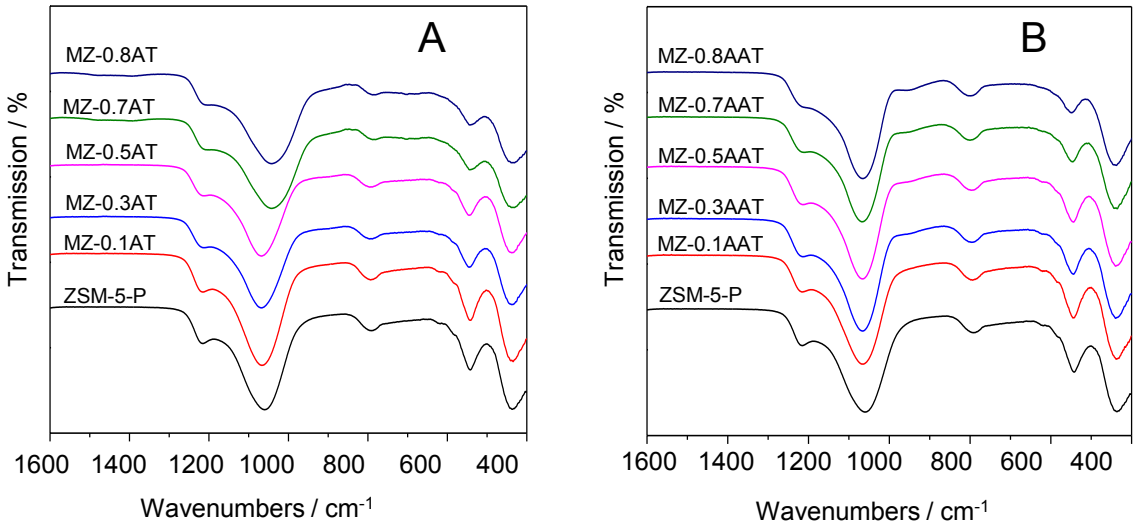

Figure B2 IR spectra of parent ZSM-5 (ZSM-5-P) and treated samples: (A) MZ-xAT and (B) MZ-xAAT.

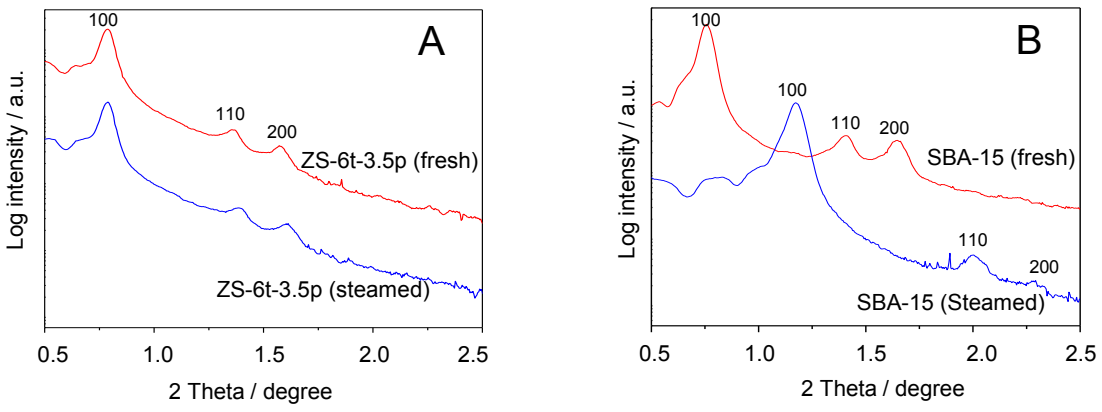

Figure B3 SAXS patterns of the fresh and steamed samples at 800 °C for 4 h: (A) ZS-6t-3.5p and (B) SBA-15.

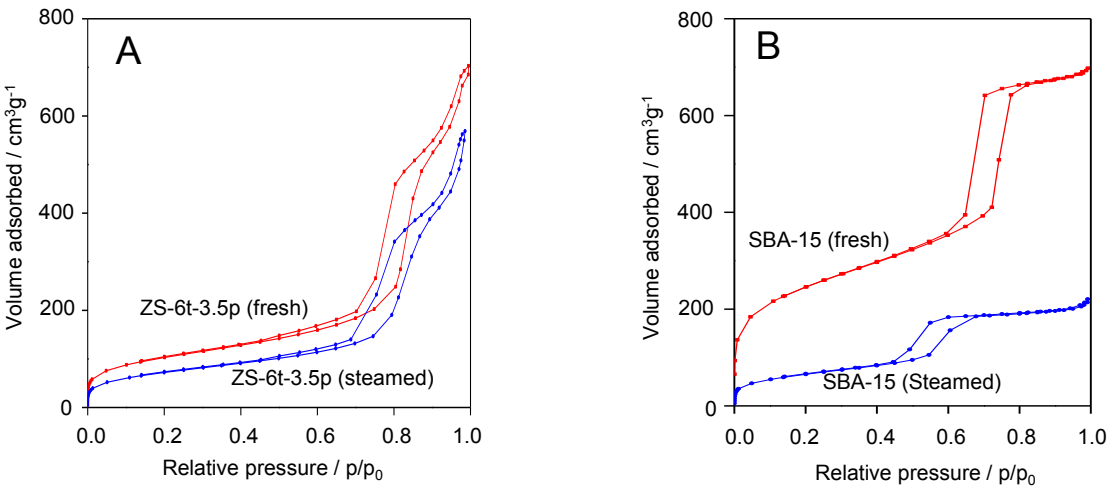

Figure B4 N_2 sorption isotherms of the fresh and steamed samples at 800 °C for 4 h: (A) ZS-6t-3.5p and (B) SBA-15.

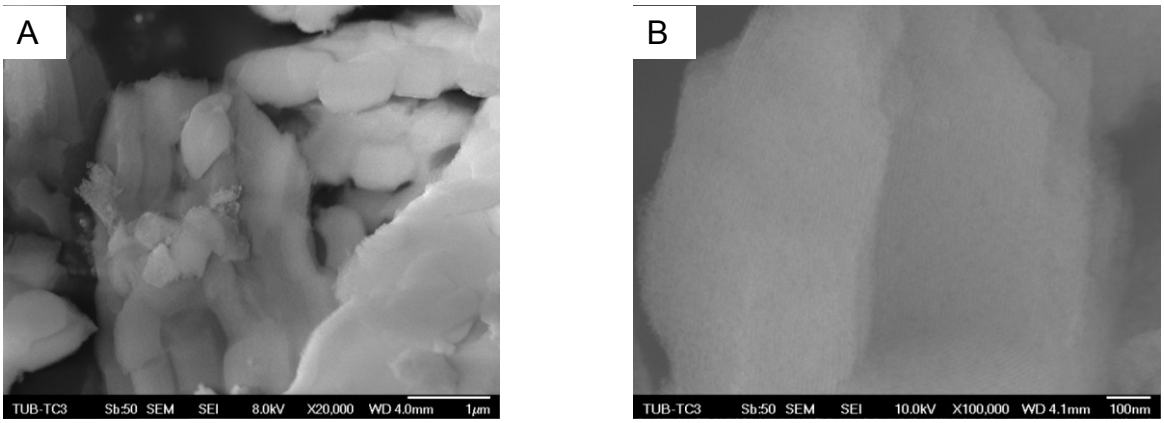

Figure B5 SEM images of Al-SBA-15 at low (A) and high (B) magnifications.

Table B1 GC conditions for gas product analysis.

Valve temperature	120 ºC
Oven temperature program	60 ºC hold 1 min, to 80 ºC at 20 K/min, to 190 ºC at 30 K/min
FID channel	
Front inlet	150 ºC, split ratio: 30:1 (higher or lower split ratio according to the concentrations of hydrocarbons)
Column	6: DB-1 (2 m x 0.32 mm x 5 µm)
	7: HP-PLOT Al_2O_3 S (25 m x 0.32 mm x 8 µm)
Column flow (He)	3.3 mL/min (12.7 psi at 60 °C), constant flow mode
FID	
Temperature	200 ºC
H_2 flow	40 mL/min
Air flow	400 mL/min
Make up (N_2)	40 mL/min
Second TCD channel	
Column	1: HayeSep Q 80/100 mesh
	2: HayeSep Q, 80/100 mesh
	3: Molecular sieve 5A, 60/80 mesh
Column flow (He)	25 mL/min (36 psi at 60 °C), constant flow mode
Procolumn flow (He)	22 mL/min at 60 °C (7 psi), constant pressure mode
TCD	
Temperature	200 ºC
Reference flow	45 mL/min
Make up	2 mL/min
Third TCD channel	
Column	4: HayeSep Q 80/100, mesh
	5: Molecular sieve 5A, 60/80, mesh
Column flow (N_2)	24 mL/min, (26 psi at 60 °C), constant flow mode
Procolumn flow (N_2)	7 psi, (24 mL/min at 60 °C), constant pressure mode
TCD	
Temperature	200 ºC
Reference flow	30 mL/min
Make up	2 mL/min

Table B2 Effect of the reaction temperature on the composition of gaseous products in the catalytic cracking of triolein over ZSM-5-P and MZ-0.5AAT at a CTO ratio of 0.4 (g/g).

Sample	**ZSM-5-P**				**MZ-0.5AAT**			
Reaction temperature (°C)	**400**	**450**	**500**	**550**	**400**	**450**	**500**	**550**
Hydrogen	0.10	0.09	0.15	0.23	0.05	0.06	0.10	0.16
Methane	0.24	0.27	0.43	0.93	0.25	0.30	0.47	0.89
Ethane	0.55	0.50	0.88	1.65	0.40	0.44	0.78	1.43
Ethylene	7.00	8.28	11.89	15.15	6.52	8.02	11.73	14.87
Propane	6.37	5.47	11.21	14.62	3.83	4.21	8.70	11.71
Propene	28.34	31.05	28.30	27.52	30.16	32.56	30.65	29.21
i-Butane	4.33	4.08	6.13	5.76	4.16	4.02	5.60	5.40
n-Butane	2.30	2.49	5.22	4.53	1.56	2.01	4.14	3.93
t-2-Butene	10.72	9.27	5.88	4.29	11.66	9.34	6.45	4.81
1-Butene	5.65	5.74	4.22	3.49	6.05	5.81	4.63	3.92
i-Butene	13.58	15.41	10.14	7.13	15.99	16.50	11.12	7.93
c-2-Butene	7.08	6.43	4.22	3.13	7.72	6.50	4.64	3.53
CO_2	6.27	3.92	3.37	3.28	4.60	3.15	3.10	3.64
CO	7.46	7.01	7.98	8.30	7.06	7.09	7.87	8.55

Table B3 Effect of the CTO ratio on the composition of gaseous products in the catalytic cracking of triolein over ZSM-5-P and MZ-0.5ATT at 450 °C.

Sample	**ZSM-5-P**				**MZ-0.5AAT**			
CTO ratio (g/g)	**0.2**	**0.4**	**0.8**	**1.2**	**0.2**	**0.4**	**0.8**	**1.2**
Hydrogen	0.13	0.09	0.13	0.20	0.08	0.06	0.10	0.17
Methane	0.62	0.27	0.33	0.53	0.61	0.30	0.42	0.66
Ethane	0.67	0.50	0.74	1.18	0.71	0.44	0.80	1.34
Ethene	6.71	8.28	8.55	7.45	5.94	8.02	8.72	7.17
Propane	2.65	5.47	14.66	22.20	1.74	4.21	12.60	21.92
Propene	29.49	31.05	23.45	17.74	30.39	32.56	25.00	16.95
i-Butane	1.16	4.08	12.37	16.87	0.97	4.02	12.60	19.36
n-Butane	1.55	2.49	6.13	8.22	1.23	2.01	5.41	8.30
t-2-Butene	10.02	9.27	6.10	4.12	10.32	9.34	6.29	3.98
1-Butene	6.38	5.74	3.83	2.60	6.41	5.81	3.98	2.47
i-Butene	13.01	15.41	10.97	7.35	13.44	16.50	11.28	7.00
c-2-Butene	6.96	6.43	4.25	2.89	7.15	6.50	4.42	2.80
CO_2	9.11	3.92	2.57	2.84	9.25	3.15	2.35	2.29
CO	11.54	7.01	5.91	5.82	11.77	7.09	6.03	5.60

Table B4 Effect of the reaction temperature and CTO ratios on the composition of gaseous products in the catalytic cracking of triolein over ZS-24t-3.5p.

CTO ratio (g/g) or	**CTO ratio = 0.4 g/g**			**550 °C**		
reaction temperature (°C)	**450**	**500**	**550**	**0.2**	**0.8**	**1.2**
Hydrogen	0.24	0.14	0.09	0.17	0.08	0.10
Methane	1.54	1.12	1.56	1.78	1.23	1.15
Ethane	2.13	1.45	2.02	2.46	1.42	1.31
Ethene	2.46	4.24	4.65	5.47	5.02	7.17
Propane	2.49	2.11	2.10	2.30	1.78	2.41
Propene	14.16	29.59	27.73	26.57	35.96	39.10
i-Butane	0.35	2.57	0.22	0.20	0.70	2.32
n-Butane	2.59	1.10	1.57	1.47	1.19	1.04
t-2-Butene	6.17	9.31	8.45	8.57	8.34	8.93
1-Butene	4.69	9.88	6.81	6.98	6.77	6.94
i-Butene	5.52	12.71	11.25	10.17	13.23	13.19
c-2-Butene	3.92	5.14	6.19	6.30	6.12	6.43
CO_2	20.89	8.19	11.88	12.41	7.67	4.17
CO	35.09	13.91	15.43	15.15	10.49	5.81

Table B5 Gas compositions in the catalytic cracking of WCO over various catalysts under the mild reaction conditions (450 °C, CTO ratio = 0.4 (g/g)).

Catalysts	**Midas-BSR**	**ZS-24t-3.5p**	**ZSM-5-P**	**MZ-0.5AAT**
Hydrogen	0.27	0.22	0.09	0.04
Methane	1.48	1.40	0.34	0.26
Ethane	2.25	1.21	0.56	0.37
Ethene	3.19	3.69	7.50	6.62
Propane	9.73	2.26	5.84	3.42
Propene	12.75	21.56	28.68	31.51
i-Butane	10.25	0.32	4.58	3.36
n-Butane	6.51	2.35	2.58	1.55
t-2-Butene	3.63	5.61	8.73	10.03
1-Butene	3.52	4.26	5.30	5.94
i-Butene	2.51	5.01	13.70	16.45
c-2-Butene	2.47	3.56	6.01	6.88
CO_2	30.69	31.88	5.61	3.81
CO	10.66	16.93	10.50	9.83

Table B6 Gas compositions in the catalytic cracking of WCO over various catalysts under severe reaction conditions (550 °C, CTO ratio = 0.4 g/g).

Catalysts	**Midas-BRS**	**ZS-24t-3.5p**	**ZSM-5-P**	**MZ-0.5AAT**
Hydrogen	0.17	0.11	0.19	0.21
Methane	2.35	1.44	0.80	1.06
Ethane	2.98	1.89	1.42	1.17
Ethene	6.99	5.40	14.44	13.33
Propane	4.64	1.96	12.15	11.52
Propene	24.93	34.86	28.19	32.72
i-Butane	3.82	0.47	4.15	4.47
n-Butane	3.40	1.21	4.76	3.99
t-2-Butene	6.63	9.04	4.81	6.35
1-Butene	6.12	7.22	3.80	3.76
i-Butene	6.25	13.23	7.63	7.96
c-2-Butene	4.82	6.58	3.49	3.82
CO_2	13.47	8.89	3.90	3.60
CO	13.41	10.98	10.21	8.18

Appendix C

List of Publications

The publications related to the work described in this thesis are listed below. Part of the work has not been published yet, but was included for relevant publications.

Journals

X. H. Vu, N. Steinfeldt, U. Armbruster, A. Martin, “Improved hydrothermal stability and acidic properties of ordered mesoporous SBA-15 analogs assembled from nanosized ZSM-5 precursors”, *Micropor. Mesopor. Mater.* 164 (2012) 120-126.

X. H. Vu, U. Bentrup, M. Hunger, R. Kraehnert, U. Armbruster, A. Martin, “Direct synthesis of nanosized-ZSM-5/SBA-15 analog composites from preformed ZSM-5 precursors for improved catalytic performance as cracking catalyst”, J. Mater. Sci. 49 (2014) 5676-5689.

X. H. Vu, M. Schneider, U. Bentrup, T. T. Dang, B. M. Q. Phan, D. A. Nguyen, U. Armbruster, A. Martin, “Hierarchical ZSM-5 materials for an enhanced formation of gasoline hydrocarbons and light olefins in catalytic cracking of triglyceride-rich biomass”, *Bioresource Technol.* (2014), to be submitted.

X. H. Vu, S. Nguyen, T. T. Dang, B. M. Q. Phan, D. A. Nguyen, U. Armbruster, A. Martin, “Catalytic performance of hierarchical ZSM-5 catalysts in the catalytic cracking of waste cooking oils under FCC conditions: A comparative study”, manuscript in preparation.

Conference contributions

15. International Congress on Catalysis, Munich, Germany, July 1-6,2012
X. H. Vu, U. Armbruster, A. Martin, “High-temperature synthesis of ordered mesoporous materials assembled from pre-formed ZSM-5 precursors by pH control“ (Poster Presentation).

15. Norddeutsches Doktorandenkolloquium, Kiel, Germany, September 24-25, 2012
X. H. Vu, U. Armbruster, A. Martin, "Nanosized micro-/mesoporous materials assembled from preformed ZSM-5 precursors for improved catalytic performance" (Oral Presentation).

25. Deutsche Zeolith-Tagung, Hamburg, Germany, March 6-8, 2013
X. H. Vu, U. Armbruster, A. Martin, "Hierarchical materials with improved catalytic properties" (Oral Presentation).

46. Jahrestreffen Deutscher Katalytiker, Weimar, Germany, March 13-15, 2013
X. H. Vu, U. Armbruster, A. Martin, "Nano-scale micro-/mesoporous materials for improved hydrocarbon cracking activity" (Poster Presentation).

VPI International Science and Technology Conference, Hanoi, Vietnam, May 22-23, 2013.
X. H. Vu, U. Armbruster, A. Martin, "Direct synthesis of nanocomposites for improved heavy oil catalytic cracking performance" (Poster Presentation).

LIKAT/ CaSuS Workshop, Rostock, Germany, September 16-18, 2013
X. H. Vu, T. T. Dang, B. M. Q. Phan, D. A. Nguyen, U. Armbruster, A. Martin, "Enhanced production of gasoline and light olefins in the catalytic cracking of waste cooking oils over meso-ZSM-5" (Poster Presentation).

47. Jahrestreffen Deutscher Katalytiker, Weimar, Germany, March 12-14, 2014
X. H. Vu, R. Eckelt, M.-M. Pohl, U. Armbruster, A. Martin, "An effective strategy for improved gasoline and light olefin production by catalytic cracking of plant oil under FCC conditions" (Poster Presentation).

Appendix D

Curriculum Vitae

Personal data

Name:	Xuan Hoan Vu
Date of birth:	12.11.1980
Nationality	Vietnamese
Marital status	Married

Academic Education

10.2010-present	**Leibniz-Institut for Catalysis e.V., University of Rostock, Germany** PhD student at the department of Heterogeneous Catalytic Processes" Title: "Hierarchical Zeolitic Catalysts for Cracking of Triglyceride-biomass to Hydrocarbons: Synthesis, Characterization and Catalytic Performance" Supervisors: PD Dr. Andreas Martin, Dr. Ing. Udo Armbruster
8.2003-10.2005	**School of Chemical Technology, TU Hanoi** Master thesis: "Effects of Supports on the Catalytic Performance of Pt-SO_4^{2-}/ZrO_2+Al_2O_3 in Isomerization of n-pentane" Supervisor: Prof. Dr. Nguyen Thi Minh Hien
9.1998-6.2003	**School of Chemical Technology, TU Hanoi** Bachelor thesis: "Preparation of Pt/ γ-Al_2O_3 for Isomerization of Light Naphtha" Supervisor: Asst.Prof. Dr. Le Van Hieu

Profession

2.2005-9.2010	**Vietnam Petroleum Institute, PetroVietnam Group** Research Engineer at Centre for Technology Application and Transfer.